
Empirical and physical modelling of the
accretion-powered X-Ray pulsars KS 1947+300 and
A 0535+26

Masterarbeit aus der Physik

vorgelegt von

Ralf Ballhausen

16. November 2015

Dr. Karl Remeis-Sternwarte Bamberg
Astronomisches Institut der Universität Erlangen-Nürnberg



Betreuer: Prof. Dr. Jörn Wilms

Abstract

Accretion powered X-ray pulsars provide a unique laboratory to study the behavior of matter in extreme magnetic and gravitational fields. The energy that is released by the accreted matter is mostly radiated away in X-rays. Because they have magnetic fields of 10^{12} G in strength, the infalling matter is directed to the polar caps and because of the rotation of the neutron star, the sources often show pulsations with each pulse phase being connected to different viewing angles onto the neutron star and the accretion column.

This thesis describes the spectral and timing analyses of the two accreting X-ray pulsars KS 1947+300 and A 0535+26 which both have massive Be-star companions. An overview of different empirical and physical spectral models is given their application to data taken with *Suzaku*, *NuSTAR* and *Swift* is presented.

The timing analysis of *Suzaku* and *NuSTAR* observations of KS 1947+300 shows an evolution of the pulse profile from one broad single peak to a broad and a narrow peak with increasing energy. This behavior is rarely seen in X-ray pulsars but has been observed in this particular source before.

The phase-averaged spectrum is well described by an absorbed powerlaw with high-energy cutoff and an additional blackbody. Emission lines of neutral, He-like and H-like iron are detected. A cyclotron resonance scattering feature could not be significantly detected because of insufficient energy coverage but its inclusion is in agreement with parallel *NuSTAR* observations.

The pulse phase resolved spectra show a variation of the all continuum parameters, in particular the black body temperature and a variation of N_{H} over pulse phase. These variations are affected by strong, artificial parameter correlations, but the spectral shape clearly changes over pulse phase.

Spectral analysis of two observations of A 0535+26 at very low luminosities shows that the spectral shape changes dramatically around 10^{36} erg s⁻¹. While the empirical spectral model of the brighter observation is in agreement to previous observations, the same model fails for the fainter observation. Measurements of the CRSF energy confirm previous findings that it stays constant over a wide range of luminosity. The *NuSTAR* observations allowed better constraints on the CRSF at low luminosities than previous observations.

Physical spectral models based on the theory of spectral formation by [Becker & Wolff \(2007\)](#) are tested on the phase averaged spectra, resulting in very promising best fits. A quantitative interpretation of the best fit parameters is not yet possible because some of the models are still under development and a more detailed investigation of the model characteristics is required but also currently in progress.

Deutsche Zusammenfassung

Akkretierende Neutronensterne bieten ein einzigartiges Laboratorium, um das Verhalten von Materie in extremen Magnet- und Gravitationsfeldern zu studieren. Die Energie, die von dem akkretierten Material freigesetzt wird, wird hauptsächlich im Röntgenbereich abgestrahlt. Durch das starke Magnetfeld von 10^{12} G wird die einfallende Materie zu den magnetischen Polen gelenkt und durch die Rotation des Neutronensterns zeigen diese Quellen häufig Pulsationen, wobei verschiedene Pulsphasen verschiedene Blickwinkel auf den Neutronenstern und die Akkretionssäule repräsentieren.

Die vorliegende Arbeit beschreibt spektroskopische und zeitliche Analysen der akkretierenden Röntgenpulsare KS 1947+300 und A 0535+26, deren Begleiter beide massereiche Be-Sterne sind. Sie gibt einen Überblick über verschiedene empirische und physikalische Spektralmodelle und zeigt deren Anwendung auf Beobachtungsdaten von *Suzaku*, *NuSTAR* und *Swift*.

Die Zeitanalyse von *Suzaku* und *NuSTAR* Beobachtungen von KS 1947+300 zeigen eine Entwicklung der Pulsprofile von einem einzigen, breiten Peak zu einem breiten und einem schmalen Peak mit steigender Energie. Dieses Verhalten ist ungewöhnlich für Röntgenpulsare, wurde bei dieser Quelle jedoch schon früher beobachtet.

Das phasengemittelte Spektrum wird gut durch ein absorbiertes Potenzgesetz mit einem exponentiellen cut-off bei hohen Energien und einer zusätzlichen Schwarzkörperkomponente beschrieben. Das Spektrum zeigt Emissionslinien von neutralem, He-artigen und H-artigen Eisen. Eine Zyklotronresonanzlinie konnte aufgrund des lückenhaften Energiebereichs der Detektoren nicht signifikant detektiert werden, aber ihre Berücksichtigung ist im Einklang mit parallelen *NuSTAR* Beobachtungen.

Die pulphasen-aufgelösten Spektren zeigen eine Variation von allen Kontinuumsparametern, insbesondere der Schwarzkörpertemperatur und des N_H über die Pulsphase. Die detektierten Variationen werden von starken, artifiziellen Parameterkorrelationen innerhalb des Modells beeinflusst, die Form des Spektrums ändert sich jedoch deutlich mit der Pulsphase.

Spektroskopie von zwei Beobachtungen von A 0535+26 bei sehr niedrigen Leuchtkräften zeigen, dass sich das Spektrum bei einer Leuchtkraft von ca. 10^{36} erg s⁻¹ dramatisch ändert. Während das empirische Spektralmodell bei der helleren Beobachtung noch mit früheren Beobachtungen verträglich ist, versagt es bei der leuchtschwächeren Beobachtung. Messungen der Zyklotronresonanzenergie bestätigen frühere Berichte, dass sich diese nicht signifikant mit der Leuchtkraft ändert. Die *NuSTAR* Beobachtungen erlauben aber eine deutlich bessere Bestimmung der Zyklotronresonanzenergie bei niedrigen Leuchtkräften als frühere Beobachtungen.

Physikalische Modelle basierend auf der Theorie über die Ausbildung des Spektrums nach [Becker & Wolff \(2007\)](#) werden an den phasengemittelten Spektren getestet und liefern sehr vielversprechende Ergebnisse. Eine quantitative Interpretation der Fitparameter ist noch nicht möglich, da sich diese Modelle teilweise noch in der Entwicklung befinden und noch eine tiefere Untersuchung des jeweiligen Verhaltens und der individuellen Besonderheiten erfordern. Daran wird jedoch zum gegenwärtigen Zeitpunkt intensiv gearbeitet.

Contents

1	Introduction	9
2	Physical background	10
2.1	Formation of neutron stars	10
2.2	Neutron star binaries	10
2.3	Accretion mechanisms	11
3	Spectral formation and modelling	13
3.1	Radiative Processes	13
3.1.1	Black Body radiation	13
3.1.2	Bremsstrahlung	14
3.1.3	Comptonization	15
3.1.4	Fluorescence	15
3.1.5	Cyclotron resonant scattering	15
3.2	The X-ray spectra of accreting pulsars	17
3.3	Empirical and Physical models	19
3.3.1	Empirical models	19
3.3.2	Physical models	21
4	Observational methods	25
4.1	<i>Suzaku</i>	25
4.2	<i>NuSTAR</i>	27
4.3	<i>Swift</i>	27
5	<i>Suzaku</i> observations during the 2013 outburst of KS 1947+300	31
5.1	KS 1947+300 – a brief overview	31
5.2	Data Acquisition and Reduction	32
5.2.1	<i>Suzaku</i>	33
5.2.2	<i>NuSTAR</i>	35
5.3	Timing analysis	35
5.4	Phase averaged spectroscopy	36
5.5	Phase resolved spectroscopy	40
5.6	Discussion	45
6	<i>NuSTAR</i> observations of A 0535+26 at low luminosities	48
6.1	The history of A 0535+26	48
6.2	Data Acquisition and Reduction	49
6.2.1	<i>NuSTAR</i>	49
6.2.2	<i>Swift</i>	49
6.3	Timing Analysis	50
6.4	Spectral Analysis	51
6.4.1	Empirical models	52
6.4.2	The compmag model	55

6.4.3	The BWcbbb model	56
6.5	Discussion	57
7	Conclusions and outlook	59

1 Introduction

From archaeological findings we know that astronomy is certainly among the oldest sciences pursued by mankind. The *Nebra Sky Disk*, which was dated 1600 B.C.¹, gives proof that already prehistoric cultures observed the night sky in Europe and the *MUL.APIN tablets* is an astronomical catalogue developed in Mesopotamia around 690 B.C.².

But in fact, in all early civilizations like e.g. the Maya, Egypt, or Greek, astronomy had a great influence on culture and religion. The thorough study of the night sky becomes even more impressive when keeping in mind, that for thousands of years the sky was only observed by the naked eye and the incredible sensitivity and resolution of the human eye is certainly one of the miracles of evolution. Obviously, the human eye has to bear bright daylight without being damaged but a high sensitivity to low intensity is certainly advantageous but could in principle be superseded by other advanced sensory organs. Therefore, it is truly remarkable, that one can in fact *see* individual stars and one could hardly imagine the development of humanity if the eye were only a tiny bit less sensitive at low intensities. But still, most astronomical objects stay concealed from the naked eye because they are too faint.

Favoured by the development of optical instruments that could collect and focus light from the 17th century onwards, the sensitivity was expanded to lower and lower intensities and even today, astronomers are working on increasing the size of telescopes to study the faintest sources in the universe. With the general goal to maximize the observability of all different kinds of astronomical objects, it is only logical to not only expand the sensitivity to intensity but also to wavelength, although the latter could only be realized quite some time later.

Today, the sky is observed from radio wavelengths up to Gamma rays of several TeV using ground based observatories as well as space satellites. Certain wavelength ranges proved particularly suited for certain classes of sources, although of course multi-wavelength observations provide the most information on a given source.

The class of sources studied in this thesis are accretion powered X-ray pulsars, which consist of a neutron star and a main-sequence companion star. While fast rotating neutron stars are often observed in the radio, in binary systems they tend to be very bright in X-rays. The companion star is mostly observed at optical wavelengths which allow us to classify the star and determine its activity. X-ray observations allow us to study the accretion processes and properties of the neutron star or the whole system.

¹ http://www.lda-lsa.de/en/nebra_sky_disc/

² <http://www.nature.com/news/2007/070528/full/news070528-11.html>

2 Physical background

2.1 Formation of neutron stars

This section gives only a brief summary of stellar evolution that can lead to the formation of neutron stars. More detailed information of stellar structure and evolution can be found in standard astronomy textbooks, e.g., [Kippenhahn & Weigert \(1990\)](#) or [Prialnik \(2009\)](#). A review on the theory of Core-collapse Supernovae is given by [Janka et al. \(2007\)](#).

According to current theory, neutron stars are compact objects which remain from a Supernova explosions of type II. These are the standard scenarios massive stars ($M \gtrsim 8M_{\odot}$) end their life in. Like all main sequence stars, massive stars are powered by nuclear fusion, forming a hydrostatic equilibrium between thermal, radiation and gravitational pressure. At the beginning of its life, hydrogen burning is the only possible fusion process producing helium in the center of the star, where the fusion process is ignited. While the amount of helium increases, the helium core gets hotter and denser until the fusion reaction of helium to carbon and oxygen is possible. Subsequent fusion processes to heavier elements are triggered at sufficient temperatures and densities and towards the end of its life, the star has an onion-like structure where different fusion processes are active at the same time.

The fusion chain usually stops at the production of ^{56}Fe , since no more energy can be produced in standard nuclear fusion reactions¹. The growing iron core is only stabilized by degeneracy pressure of the electrons in the iron plasma which has to stand the gravitational pressure. This is only possible up to masses of the core of the *Chandrasekhar limit* of $\sim 1.4 M_{\odot}$ ([Chandrasekhar 1931](#))². If the mass of the core exceeds this limit, the core collapses and temperature and density increase abruptly. The previously built iron nuclei are fissioned by photo-disintegration and neutrons are formed by electron capture of protons (also called inverse β -decay). The neutrons again form a Fermi gas that is prevented from further compression by degeneracy pressure. This neutron gas is more “robust” with respect to gravitation than the electron gas was and can reach masses of up to the *Oppenheimer-Volkoff limit* of originally $\sim 0.7 M_{\odot}$ ([Oppenheimer & Volkoff 1939](#); [Tolman 1939](#)) while modern calculations rather predict a limit of $\sim 3 M_{\odot}$ ([Bombaci 1996](#)). Depending on whether the critical mass of the neutron gas is reached during the supernova, a neutron star can form or the core collapses again to a black hole. The outer layers of the progenitor star are expelled.

Neutron stars usually have very magnetic fields and rotate extremely fast, because of the conservation of magnetic flux and angular momentum during their birth.

2.2 Neutron star binaries

While isolated neutron stars are often observed as radio pulsars, many neutron stars are gravitationally bound to a main-sequence companion star, forming a so called *binary*. In binaries, mass transfer from one object to the other is possible and the accretion of matter onto a compact object is the most effective energy source in the universe. Accreting neutron stars tend to be very bright in X-rays, because hard

¹ It should be noted that the mean binding energy per nucleon of ^{62}Ni is even higher than that of ^{56}Fe ([Fewell 1995](#)), so in principle energy could be released in further fusion reactions

² In his original work, [Chandrasekhar](#) derived a critical mass of $0.91 M_{\odot}$. The modern value of $1.4 M_{\odot}$ was first calculated by [Gamow \(1939\)](#) and results from a different molecular weight per electron than [Chandrasekhar](#) assumed

X-ray radiation directly originates from the accreted matter during its way to the neutron star's surface, as will be discussed later in more detail.

Depending on the mass of the companion star, X-ray binaries are classified as *Low Mass X-Ray Binaries* (LMXB) or *High Mass X-Ray Binaries* (HMXB). This also applies for black holes.

LMXB can have main sequence stars with masses of around or less the mass of the Sun but also White Dwarfs and Red Giants. Examples of LMXBs with neutron stars as compact objects are Her X-1, SAX J1808.4–3658, and Aql X-1 (Jurua et al. 2011; Patruno et al. 2015; Casella et al. 2008, respectively, and references therein).

The optical companions usually in HMXB are O- or B(e)-stars or blue Supergiants. Examples of HMXBs with neutron stars are Vela X-1, 4U 0115+63, and GX 304-1 (Kreykenbohm et al. 2008; Müller et al. 2013; Klochkov et al. 2012, respectively, and references therein).

A detailed description of binary systems can be found in, e.g., Hilditch (2001).

2.3 Accretion mechanisms

The mass transfer from the companion star to the compact object is a complex process because General Relativity, plasma physics and Magneto-Hydrodynamics have to be considered in the full picture. However, the accretion process can be roughly classified into one of the following types.

Roche lobe overflow: In close binaries, the volume where matter is still gravitationally bound to one of the components is called its *Roche lobe*. It is not infinite because of the two masses in the system and centrifugal forces in the binary. If the the Roche lobe is filled with matter by the companion, matter can pass the potential barrier at the Lagrange point L_1 . The conservation of angular momentum leads to the formation of an accretion disk around the compact object. An example for a neutron star binary, where accretion takes place via Roche lobe overflow is Her X-1 (Jurua et al. 2011).

Wind accretion: Massive stars with very high surface temperatures tend to have strong stellar winds. The compact object can accrete directly from the wind. This mechanism was first proposed by Bondi & Hoyle (1944). A very recent review on wind accretion is given by Shakura et al. (2015). An extensively studied wind accreting neutron star is Vela X-1 (e.g., Kreykenbohm et al. 2008).

Be-Disk accretion: Be stars are B-type stars with additional hydrogen emission lines in their spectra. These lines are not emitted from the star directly but from a circumstellar disk that forms because of the rotation of the star and the conservation of angular momentum (e.g., Reig 2011). If the orbit is eccentric, accretion from the Be disk usually happens at ore close to the periastron of the orbit, although the exact accretion mechanism is still under discussion. These sources are often *Transients*, i.e., they are luminous in X-rays only for a short amount of time but then switch off again. The rise in luminosity connected to periastron passage is called a Type-I outburst, but also irregular, giant Type-II outburst can happen at any orbital phase and are supposed to be caused by a change of the optical companion, although the detailed mechanism is not yet known (Negueruela & Okazaki 2000). An example for a Be disk accreting neutron star which shows very regular outbursts – though not always – is GRO J1008–57 (Kühnel et al. 2013).

The maximum available power provided by the accretion process depends on the gravitational potential that the accreted matter passes and the mass accretion rate \dot{M} , i.e, the amount of accreted matter per time. Assuming matter falling from infinity – although in reality from gravitational potential of the companion – onto the surface of a compact object of radius R , the released gravitational energy

per time is given by

$$L_{\text{acc}} = G \frac{M_{\text{NS}} \dot{M}}{R}, \quad (2.1)$$

where G is the gravitational constant and M_{NS} the neutron star mass.

It is worth noticing that because of the very strong magnetic field of the neutron star, there is a lower limit for the mass accretion rate because of the so-called “propeller effect” (Illarionov & Sunyaev 1975). The co-rotating magnetosphere blocks matter from being accreted onto the neutron star if the ram pressure is too weak. The interaction of the accretion disc and the magnetosphere is rather complicated and scenarios of “trapped” disks, disk instabilities and their connection to variability in X-ray luminosity are discussed by D’Angelo & Spruit (2010, 2011, 2012).

3 Spectral formation and modelling

In accretion powered pulsars, gravitational energy is converted partly to electromagnetic radiation, making them bright X-ray sources. The most important fundamental mechanisms involved in the formation of X-ray spectra of accreting pulsars are atomic processes (e.g., fluorescence or absorption), black body radiation, bremsstrahlung and electron-photon scattering. Although all of these processes are relatively well understood and the governing equations have been solved for simple scenarios, the combination of all of them, together with a huge range of the involved physical properties like density, temperature or magnetic field strength, make the theoretical prediction of exact spectral shape of an accreting pulsar extremely difficult.

In the presence of strong magnetic fields, *cyclotron resonant scattering* occur and provide a way to both absorb and create photons. The photons also may excite not yet fully ionized atoms in the accreted matter which then de-excite again and emit photons of characteristic energies. The most prominent example here is the Fe K α line, which is seen in most X-ray spectra of accreting pulsars.

The following chapter briefly summarizes the individual processes important for the spectral formation and how to calculate the resulting broad band spectrum. The latter is heavily based on [Becker & Wolff \(2007\)](#).

3.1 Radiative Processes

This chapter gives a brief overview over radiative processes important for astrophysics. A comprehensive review is given by [Rybicki & Lightman \(2008\)](#).

3.1.1 Black Body radiation

One of the most important radiation processes in the universe is the radiation of a *black body*. This process forms the spectra of stars or the cosmic microwave background. The name originates from the idea of an object with ideal emissivity 1. At a given temperature T the object will emit electromagnetic radiation with a continuous spectrum. The correct derivation of the spectral intensity distribution was first presented by [Planck \(1901\)](#) by calculating the entropy of a set of resonators in thermodynamic equilibrium for a total energy U . The innovative idea by Planck was that all resonators can only carry an integer multiple of a minimum energy. This is the concept of quantization and avoids the problem of the so-called *UV-catastrophe* of the *Rayleigh-Jeans-Law*, which describes the spectral energy distribution of a black body only for low frequencies but diverges for increasing frequencies.

The spectral energy distribution of a black body is given by *Planck's law*

$$B_\nu(T)dA d\nu = \frac{2h\nu^3}{c^2} \frac{1}{\exp(h\nu/kT) - 1} dA d\nu, \quad (3.1)$$

where $B_\nu(T)dA d\nu$ is the power radiated away from a surface element dA in the frequency range ν to $\nu + d\nu$. An alternative and more elegant method to derive Planck's formula was introduced by [Einstein \(1917\)](#) by proposing a rate equation for transitions in a two-level system where the occupation of states is governed by the Boltzmann distribution. A concise derivation of Planck's formula using Einstein's rate equation can be found in, e.g. [Padmanabhan \(2000\)](#).

Fig. 3.1: Photon density of a black body at different temperatures. All spectra are normalized to the photon flux of a black body of total luminosity of $10^{39} \text{ erg s}^{-1}$ at a distance of 10 kpc by varying the surface area of the emitter.

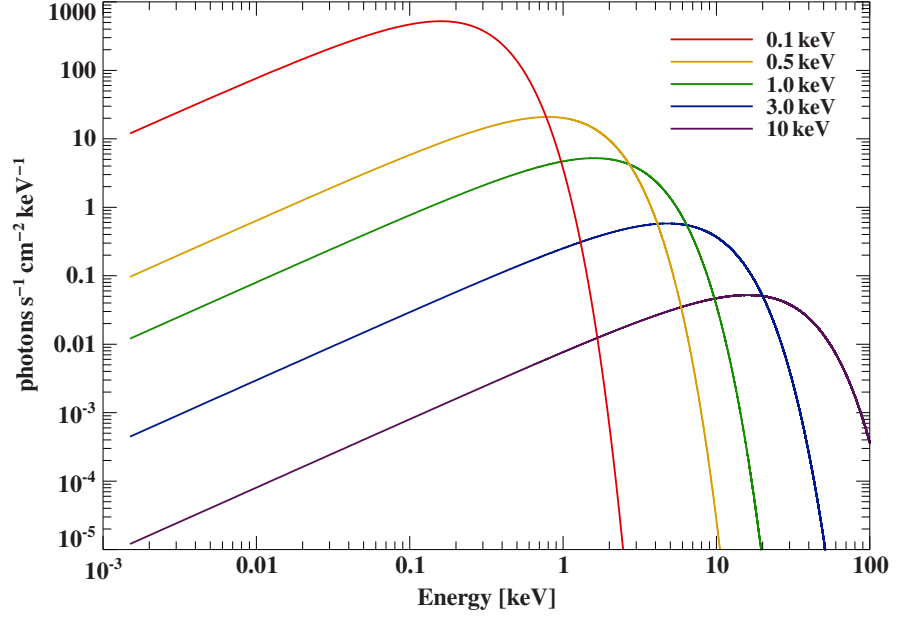


Figure 3.1 shows the photon density distribution for a black body at different temperatures. In high-energy astrophysics, it is convenient to multiply the temperature of the black body by Boltzmann's constant k to give it in units of energy. All spectra in Figure 3.1 are equally normalized, i.e., the integrated flux is the same for all spectra. Note that this is not the case for *one* real black body of surface area A , whose emitted power P_{emit} is related to its temperature by the *Stefan-Boltzmann law* (Stefan 1879; Boltzmann 1884)

$$P_{\text{emit}} = \sigma_{\text{SB}} \cdot A \cdot T^4, \quad (3.2)$$

with the Stefan-Boltzmann constant

$$\sigma_{\text{SB}} = \frac{2\pi^5 k^4}{15c^2 h^3} = 5.67 \cdot 10^{-5} \text{ erg s}^{-1} \text{ cm}^{-2} \text{ K}^{-4}. \quad (3.3)$$

Figure 3.1 also illustrates that even in energy space, the maximum emission of a black body is not at its temperature. This phenomenon is described by *Wien's displacement law* (Wien 1896). Note that there is a difference between the maximum emission of photons and the maximum emission of power. For spectral analyses, the case of photon emission is of higher interest, as it corresponds more directly to the count rate measured by a X-ray detector. In units of energy, for a black body of temperature kT , the photon energy at the maximum photon emission rate is given by

$$E_{\gamma}^{\text{max}} = 1.5936 \text{ keV} \cdot \left(\frac{kT}{1 \text{ keV}} \right), \quad (3.4)$$

so a black body of temperature 1 keV will emit most photons with an energy of $\sim 1.6 \text{ keV}$.

3.1.2 Bremsstrahlung

Bremsstrahlung refers to the radiation emitted by accelerated or decelerated charged particles. In astrophysical processes, the radiation emitted from decelerated electrons is most important. Since one cannot observe individual electrons in an astrophysical source, the velocity distribution and deceleration mechanism of the whole population of electrons contributing to the Bremsstrahlung emission determines the observed spectrum. A very general classification distinguishes between *thermal* (see, e.g., Longair 2011) and *non-thermal* Bremsstrahlung (e.g., Sarazin & Kempner 2000),

the first one being emitted from a plasma of thermal particles, whose velocity distribution is governed by a *Maxwell-Boltzmann* distribution, the second one not. For accreting X-ray pulsars, the second case generally is of more interest, because Bremsstrahlung is emitted from electrons in the accreted plasma which is decelerated from free fall to rest at the neutron star surface by Coulomb or radiation breaking.

Bremsstrahlung is an important source of seed photons for further scattering processes.

3.1.3 Comptonization

In astrophysics the term *Comptonization* refers to the energy gain of photons in gas of high energy electrons via inverse Compton scattering. It is also an effective way to cool down a gas of electrons and then referred to as *Compton cooling*.

This process is of great importance as it can produce hard X-ray radiation from soft seed photons which are upscattered in the corona of galactic black holes or the infalling plasma of accreting neutron stars.

The inverse process is also possible, where photons transfer energy to low-energy electrons. How energy is transferred depends on the initial photon energy and electron temperature. In thermodynamic equilibrium, photons gain energy if the photon energy is lower than $4kT_e$ and lose energy when it is higher (Padmanabhan 2000). The total energy transfer also depends on the number of scattering, i.e., the optical depth of the plasma and is expressed in the so-called y -parameter (Kompaneets 1957).

How Comptonization influences the spectral formation in accreting pulsars is described in more detail in Section 3.2.

3.1.4 Fluorescence

While the previously described processes form the continuum shape of the X-ray pulsar, fluorescence emission and absorption appear as localized spectral features. The origin of fluorescence is a transition of an electron in an atom which is connected to the absorption or emission of a photon. If a photon of sufficient energy is absorbed by an atom, an electron can be excited to a higher energy level or even leave the atom in which case the atom is (higher) ionized. The empty sites are filled up by electrons occupying higher levels and the energy difference released is then emitted as one or more photons. This is an extremely crude description of the atomic processes involved. For example, the de-excitation can happen in different ways and some transitions are more likely than others and depend on the quantum mechanical properties of the electrons. For details see, e.g., Sobelman (1992) or Friedrich (2006).

As challenging the understanding and modelling the atomic processes are, as powerful are they as diagnostic tools. For example, the flux ratios of different transitions in highly ionized atoms can be used to determine the density and temperature of plasmas (see, e.g., Ness et al. 2002). There is software available to calculate emission from photo-ionized plasma, like the XSTAR¹ package distributed with HEASoft. An overview of other atomic codes is given by Hell (2012)

A very characteristic feature observed in many X-ray pulsars is the $K\alpha$ line of neutral iron at an energy of 6.4 keV (see Fig. 3.2). Sometimes, even higher ionization states of iron can be observed, e.g., in Cen X-3 (see Fig. 3.3).

3.1.5 Cyclotron resonant scattering

Electrons moving in a strong magnetic field experience a quantization of their energies in *Landau levels*, analogous to the quantization of the energies of electrons in the Coulomb field of an atomic nucleus.

¹ for details, see <http://heasarc.gsfc.nasa.gov/docs/software/xstar/xstar.html>

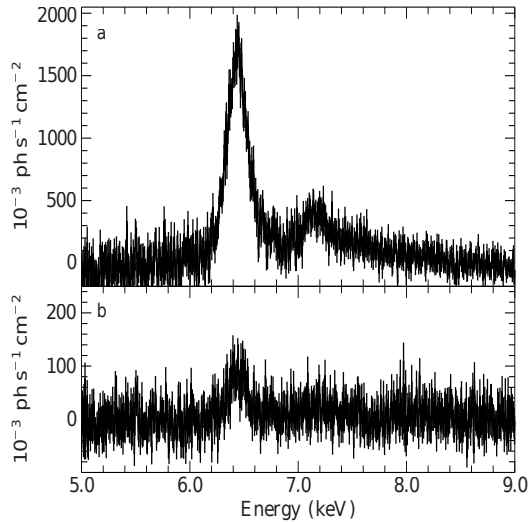


Fig. 3.2: Close-up of the iron line region of 88 *XMM-Newton* spectra of Vela X-1. The neutral iron $K\alpha$ line at 6.4 keV is clearly resolved, as well as the iron $K\beta$ line at ~ 7.1 keV with lower line flux. Figure taken from Kühnel et al. (2015).

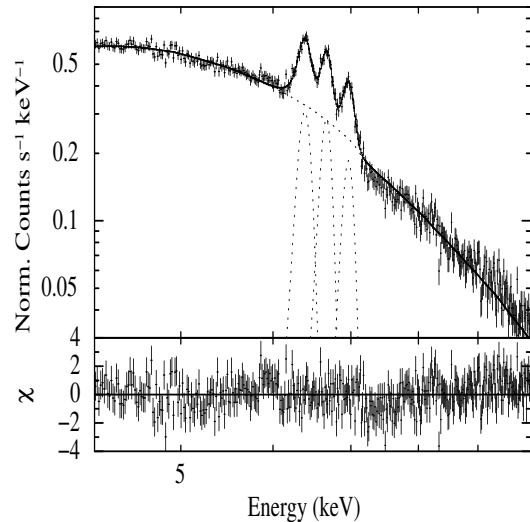


Fig. 3.3: Spectrum of the X-ray pulsar Cen X-3 observed with the *XMM-Newton* observatory. Besides the neutral iron $K\alpha$ line at 6.4 keV, also $K\alpha$ lines of He-like and H-like iron are observed. Figure taken from Naik & Paul (2012).

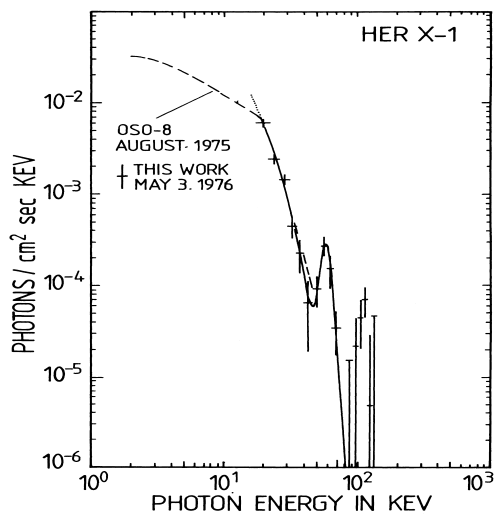


Fig. 3.4: Spectrum of Her X-1 showing the first ever detected cyclotron line at ~ 58 keV. Figure taken from Trümper et al. (1978).

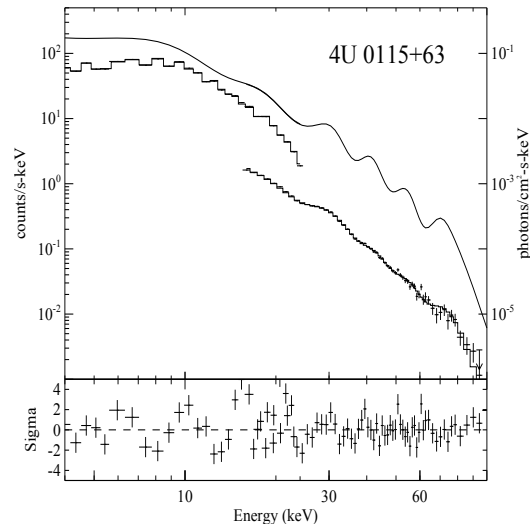


Fig. 3.5: Spectrum of 4U 0115+63 with five cyclotron lines. This is highest number of harmonics ever detected in an X-ray pulsar. Figure taken from Heindl et al. (2000).

The modelling of the cyclotron resonant scattering processes inside the column is generally done in Monte Carlo simulations (e.g., Araya & Harding 1999; Araya-Góchez & Harding 2000; Schönherr et al. 2007; Schwarm 2010).

The effect of cyclotron resonant scattering is observed as absorption features in the spectrum of many X-ray pulsars, which are also referred to as *cyclotron lines*. The first cyclotron line was discovered by Trümper et al. in 1978 in Her X-1 (see Fig. 3.4). Today, more than 20 cyclotron line sources are known, some of them even show harmonic lines (see Caballero & Wilms 2012, for a review). The source showing the highest number of harmonics is 4U 0115+63 where five cyclotron lines have been detected by Heindl et al. (2000, see Fig. 3.5).

The detection of cyclotron lines provides a direct way to measure the magnetic field strength of the neutron star at the line forming region, which is generally associated with a shock front in the accretion stream, via the so-called 12-*B*-12 rule

$$E_{\text{cyc}} = 11.6 \left(\frac{B}{10^{12} \text{ G}} \right) \left(\frac{1}{1+z} \right) \text{ keV}, \quad (3.5)$$

where z is the gravitational redshift (Schönherr et al. 2014).

The magnetic field strength is a fundamental parameter of the system and possible variation of the cyclotron line over time (e.g., Staubert et al. 2014) and especially luminosity (Becker et al. 2012), also allow even further to investigate in more detail the accretion processes and interaction of radiation and matter.

Note, that cyclotron resonant scattering processes also provide a source of seed photons in self-consistent, physical models.

3.2 The X-ray spectra of accreting pulsars

In the accretion powered X-ray pulsar, several of the previously mentioned processes take place at the same time and influence each other.

The basic scenario for the formation of the continuum was proposed by Davidson (1973). Matter is channelled into accretion columns and comes to rest at the bottom of the accretion columns, where it is accumulating and forming a mound which is heated by the steady inflow of more matter. The mound will therefore emit black body radiation and the photons then propagate through the accretion column where some of them undergo Compton scattering gaining energy from the electrons of the infalling plasma.

More precisely, Becker & Wolff (2005a,b) propose an accretion column, formed by the magnetic field of the neutron star, in which matter enters with an estimated velocity of $\sim 0.5 c$ and is decelerated to rest at the neutron star surface, mostly by radiation breaking. At a certain height in the accretion column a shock front forms, compressing the gas strongly and making for bulk Comptonization (also called “dynamical” Comptonization) very effective. This process is treated as a first-order Fermi energization where the photons gain energy from the kinetic energy of the accretion flow. The seed photons involved in this Comptonization process are black body photons emitted from a thermal mound at the bottom of the accretion column, bremsstrahlung and cyclotron emission photons. The whole configuration is illustrated in Fig. 3.6.

The emerging spectrum is calculated by solving the radiative transport equation, which including bulk Comptonization was first derived by Blandford & Payne (1981). In Becker & Wolff (2007) it reads

$$\frac{\partial f}{\partial t} + v \frac{\partial f}{\partial z} = \frac{dv}{dz} \frac{\epsilon}{3} \frac{\partial f}{\partial \epsilon} + \frac{\partial}{\partial z} \left(\frac{c}{3n_e \sigma_{\parallel}} \frac{\partial f}{\partial z} \right) - \frac{f}{t_{\text{esc}}} + \frac{n_e \bar{\sigma} c}{m_e} \frac{1}{\epsilon^2} \frac{\partial}{\partial \epsilon} \left[\epsilon^4 \left(f + kT_e \frac{\partial f}{\partial \epsilon} \right) \right] + \frac{Q(z, \epsilon)}{\pi r_0^2} \quad (3.6)$$

for the photon distribution $f(z, \epsilon)$ at height z and energy ϵ . The physical interpretation of the individual terms is:

- $\frac{\partial f}{\partial t} + v \frac{\partial f}{\partial z}$ is the co-moving derivative of the photon field with respect to time. In a steady state solution, the partial derivative $\partial f / \partial t$ will vanish.
- $\frac{dv}{dz} \frac{\epsilon}{3} \frac{\partial f}{\partial \epsilon}$ is the bulk Comptonization term describing the energy transfer of photons by passing the shock front.

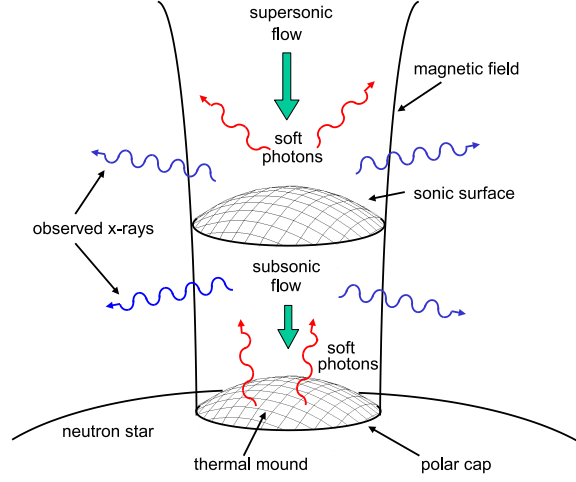


Fig. 3.6: Schematic of plot of an accretion column on a neutron star. At the bottom of the column, the matter settles to rest, building up a thermal mound which emits black body radiation. Some of the photons are (once or multiple times) Compton scattered at the shock front and leave the column. This is the observed X-ray radiation. Figure taken from [Becker & Wolff \(2007\)](#).

- $\frac{\partial}{\partial z} \left(\frac{c}{3n_e \sigma_{\parallel}} \frac{\partial f}{\partial z} \right)$ is a diffusion term along the magnetic field direction. The diffusion coefficient depends on the electron density and the (energy-averaged) scattering cross section σ_{\parallel} for the propagation of photons parallel to the magnetic field, which is lower than the Thomson cross section (see [Canuto, Lodenquai & Ruderman 1971](#), for details).
- $\frac{n_e \bar{\sigma} c}{m_e} \frac{1}{\epsilon^2} \frac{\partial}{\partial \epsilon} \left[\epsilon^4 \left(f + kT_e \frac{\partial f}{\partial \epsilon} \right) \right]$ is the *Kompaneets operator* describing the Comptonization of photons by a non-relativistic, thermal plasma. As the name suggests it was first derived by [Kompaneets \(1957\)](#). A detailed and descriptive derivation of the Kompaneets equation is given by [Katz \(1986\)](#). The original Kompaneets equation contains a term of $\mathcal{O}(f^2)$, that can be neglected if the corresponding occupation number is low, which is typical for astrophysical sources not having reached equilibrium ([Katz 1986](#)).
- $\frac{f}{t_{\text{esc}}}$ describes photon loss through the column walls with the characteristic escape time t_{esc} , which depends on the radius of the accretion column and its optical depth. This term makes the spectrum actually observable.
- $\frac{Q(z, \epsilon)}{\pi r_0^2}$: this is the source term describing the seed photons injected into the column. Assuming photon injection only from black body emission, this term would be a delta function with respect to z and a Planck spectrum with respect to ϵ . In a full solution, also Cyclotron emission, which is assumed to be mono-energetic but distributed along z , and bremsstrahlung which is continuous in both space and energy has to be considered.

The spectrum is obtained by calculating the Green's function for Eq. 3.6 and then integrating the Green's function solution for an assumed seed spectrum like black body, bremsstrahlung, and cyclotron emission and over the full column height. [Becker & Wolff \(2005a,b\)](#) did not take thermal Comptonization into account but [Becker & Wolff \(2007\)](#) found this contribution to be necessary to

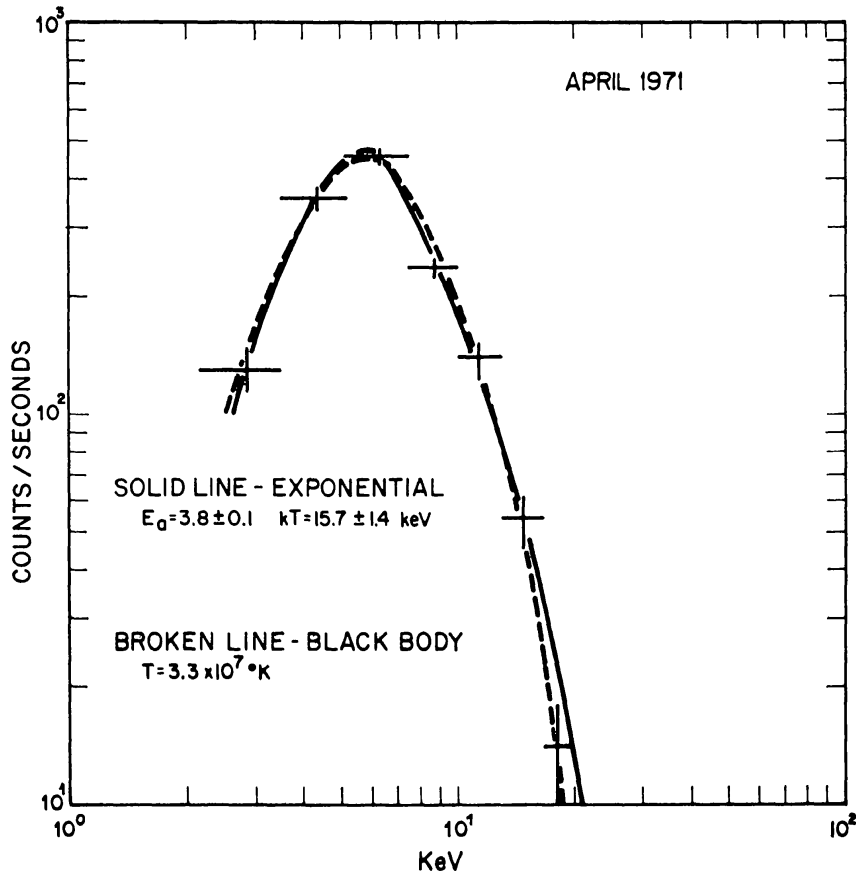


Fig. 3.7: First spectrum of the X-ray pulsar Cen X-3 taken with the *UHURU* satellite. Crosses represent the measured datapoints. The solid line is the best fit of a thermal-bremsstrahlung model with high-energy cutoff and the dashed line shows a black body model. Figure taken from [Giacconi et al. \(1971\)](#).

explain the high-energy cutoff seen in most X-ray pulsars, because it provides also a method to loose energy for photons at highest energies. Absorption at the thermal mound was neglected by [Becker & Wolff \(2007\)](#) because of its very low influence to the spectral shape.

There are some assumptions made for solving Eq. 3.6. The velocity profile of the column is approximated such that the radiative transfer equation becomes separable in energy and space. Perpendicular to the magnetic field axis, constant electron densities and temperatures are assumed.

3.3 Empirical and Physical models

The first detected X-ray pulsar is Cen X-3. It was discovered as an X-ray source by [Chodil et al. \(1967\)](#) with rocket-borne proportional counters and ~ 4.8 s pulsations were found by [Giacconi et al. \(1971\)](#) with *UHURU* satellite. The spectrum was well described by a black body or a thermal bremsstrahlung model with high-energy cutoff.

Since these early experiments, the energy resolution and range as well as the sensitivity has increased incredibly and a great number of transient and persistent neutron star binaries has been discovered. The following section briefly describes empirical models frequently used for spectral fitting of accreting pulsars. A summary of commonly used empirical models is also given by [Müller \(2013\)](#).

3.3.1 Empirical models

Due to the complexity and the computational difficulties of a solution of the radiative transfer equation, X-ray spectra of accretion-powered pulsars traditionally have been modelled with empirical models. The advantage of these models is that they are generally easy to fit in terms of runtime and computa-

tional power, the number of free parameters is often rather low and parameter degeneracies are well known or can be rather easily determined. The inevitable disadvantage is these models provide only little physical insight and that often more than one model describe the data comparably well. The long history of application allows, however, some comparison and classification, which then in turn can be used, at least in principle, to draw conclusions about the physical processes in the sources. For example: The measurement of a cyclotron line energy and its dependence on luminosity can be performed even with simple Gaussian absorption line and an empirical continuum model, although this approach is prone to massive systematic errors².

The broad band spectra of accretion-powered X-ray pulsars often have a powerlaw-like shape and some kind of cut-off at high energies. This shape is very often modelled successfully by a powerlaw with an exponential cut-off where the exact shape of the cut-off term varies between the models:

- **cutoffpl**: The `cutoffpl` model consists of a powerlaw with an overall exponential damping factor

$$\text{cutoffpl}(E) \propto E^{-\Gamma} \exp\left(-\frac{E}{E_{\text{fold}}}\right) \quad (3.7)$$

Despite its simple form, it has proven to be a very successful model in numerous cases and is widely used.

- **powerlaw × highecut**: This model consists of a “pure” powerlaw and a multiplicative factor of the form

$$\text{highecut}(E) = \begin{cases} 1, & E < E_{\text{cut}} \\ \exp\left(-\frac{E-E_{\text{cut}}}{E_{\text{fold}}}\right), & E > E_{\text{cut}} \end{cases} \quad (3.8)$$

The disadvantage of this model is that it is not continuously differentiable at the cutoff energy, which can lead to line like residuals in a spectral fit. This is particularly concerning as the cutoff energy is often in the same range of possible cyclotron lines

- **powerlaw × fdcut** provides a “Fermi-Dirac”-shaped cut-off (Tanaka 1986),

$$\text{fdcut}(E) = \frac{1}{1 + \exp\left(\frac{E-E_{\text{cut}}}{E_{\text{fold}}}\right)} \quad (3.9)$$

In many cases, an excess of photons is observed at low energies (typically below the iron $K\alpha$ energy, which cannot be modelled by the powerlaw component alone. These cases then require an additional model component for which a black body (e.g., Kühnel et al. 2013; Caballero et al. 2013; Fürst et al. 2014) or a very broad Gaussian emission feature centered $\sim 8\text{--}12$ keV, often referred to as “10-keV-feature” (e.g., Coburn et al. 2002; Rivers et al. 2010; Müller et al. 2012, 2013) turned out to be successful.

The soft component can also be accounted for using two powerlaws, one with a negative and one positive photon index, both modified by an exponential folding term. This continuum model is often referred to as “NPEX”,

$$\text{NPEX}(E) = \left(N_1 E^{-\Gamma_1} + N_2 E^{-\Gamma_2}\right) \times \left(-\frac{E}{E_{\text{fold}}}\right) \quad (3.10)$$

with $\Gamma_{1,2} > 0$ and the individual normalizations $N_{1,2}$. In many cases it is necessary to fix the positive photon index to 2.

² One remarkable example of how the choice of an empirical model can affect the obtained results is the claimed (e.g., Nakajima et al. 2006) and disproved (e.g., Müller et al. 2013) energy-luminosity dependence of the fundamental cyclotron line in 4U 0115+63.

The broadband continuum is then often modified by adding Gaussian emission lines (e.g., the iron $K\alpha$ line) and cyclotron lines are mostly modelled with either Gaussian absorption,

$$\text{gabs}(E) = \exp\left(-\frac{d}{\sqrt{2\pi}\sigma} \exp\left(-\frac{(E - E_0)^2}{2\sigma^2}\right)\right), \quad (3.11)$$

with centroid energy E_0 , width σ and line depth d or Pseudo-Lorentzian absorption lines, e.g.,

$$\text{cyclabs}(E) = \exp\left(-D_0 \frac{(W_0 E / E_{\text{cycl}})^2}{(E - E_{\text{cycl}})^2 + W_0^2} - D_1 \frac{(W_1 E / 2E_{\text{cycl}})^2}{(E - 2E_{\text{cycl}})^2 + W_1^2}\right), \quad (3.12)$$

with the optical depths D_0, D_1 and widths W_0, W_1 of the fundamental and first harmonic, respectively (Mihara et al. 1990; Makishima et al. 1990).

3.3.2 Physical models

There are some models available for accreting X-ray pulsars, which actually take the physical processes into account and give a quantitative prediction of the spectrum. The following section gives a brief overview over some commonly used models, but does not claim to be by any means complete.

Absorption

Although this is not limited to accreting X-ray pulsars at all but is indispensable for all spectral modelling is the various foreground and source intrinsic absorption. This clearly belongs to the physical modelling because atomic physics processes have to be considered. The models commonly used for spectral fitting of accreting X-ray pulsars the `tbabs` in `ISIS/XSPEC` (Wilms, Allen & McCray 2000) and the updated version `tbnew`³.

The `compTT` model

The `compTT` model is part of the current distribution of the `HEAsoft` software package and analytically calculates Comptonization of a soft seed spectrum in a thermal plasma, as described in Titarchuk (1994). For simplification, the seed spectrum is a Wien spectrum.

This model is often used for the spectral modelling of black hole binaries, such as Cyg X-1 (e.g., Pottschmidt et al. 2004; Parker et al. 2015), but it has also successfully applied to accreting neutron star binaries, e.g., KS 1947+300 (Naik et al. 2006). As shown by Titarchuk & Lyubarskij (1995), the emerging spectrum of thermal Comptonization has a powerlaw like shape. It is therefore not surprising that often a comparably good fit can be achieved with an empirical powerlaw model with high-energy cutoff can be achieved.

Figure 3.8 shows the spectral shape of the `compTT` model for some model parameters in a range, relevant for application to X-ray pulsars. The exponential high-energy cutoff, that is seen in observational data cannot be reproduced by this model alone.

The `compTB` model

This model takes both thermal and bulk Comptonization into account and was developed for application to low-mass X-ray binaries with rather weakly magnetized neutron stars. It contains an unscattered seed photon component and a bulk and thermal Comptonized component. The seed spectrum is per default a pure black body, but can be altered by the user, and a free-fall velocity profile are assumed. A full description of the model is given by Farinelli et al. (2008), where also a list of successful

³ see <http://pulsar.sternwarte.uni-erlangen.de/wilms/research/tbabs/> for details

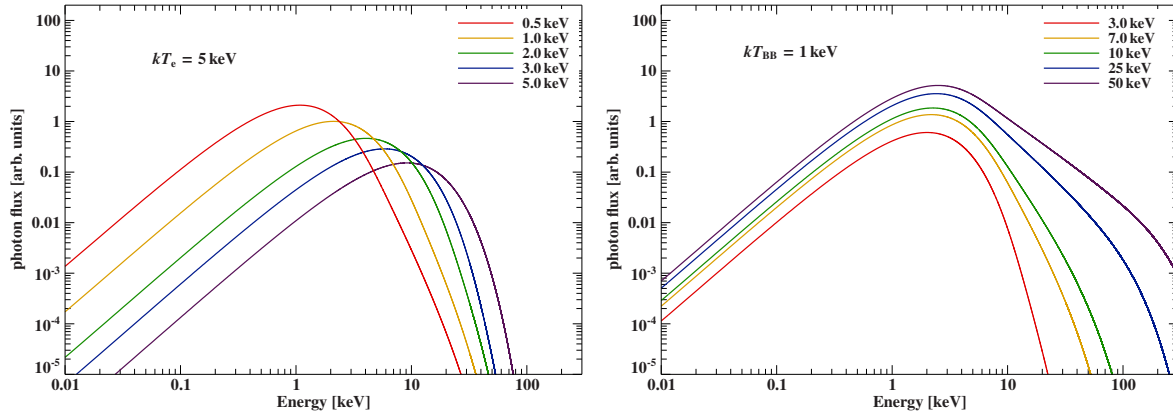


Fig. 3.8: Examples of spectra generated with the `compTT` model for different black body and electron temperatures, for the parameter range that is relevant for accreting X-ray pulsars. A change of the black body temperature shifts the maximum of the Comptonized spectrum, whereas the electron plasma temperature determines the high energy part of the spectrum. *Left:* Variation of the `compTT` model with a change of the black body temperature. The electron temperature is kept constant, as well as the optical depth ($\tau = 3$). *Right:* Variation of the `compTT` model with a change of the electron temperature. The black body temperature is kept constant, as well as the optical depth ($\tau = 3$).

applications are given. It can be regarded as an extension of the BMC model (Titarchuk, Mastichiadis & Kylafis 1997) which provides a set of Green’s functions for spherically symmetric accretion (which is not a realistic scenario in accreting neutron stars) to be convolved with a seed spectrum. The Green’s functions are characterized by a spectral index α which is connected to the electron temperature and the mass accretion rate, but rather parametrizes the efficiency of energy transfer. It is therefore not restricted to a special kind of Comptonization process, i.e., either bulk or thermal Comptonization.

The `compTB` model now includes the δ -parameter to specify the individual contributions of bulk and thermal Comptonization but still contains the spectral index parameter instead of the optical depth. The BMC model failed for most accreting pulsar, because it does not describe the high-energy cut-off properly. The `compTB` model is limited to weakly magnetized neutron stars, because cyclotron emission as a source of seed photons is not taken into account and the influence of the magnetic field to the scattering cross sections is also neglected.

Figure 3.9 shows the dependency of the spectral shape of the `compTB` model on the parameters δ and α . The δ -parameter is the ratio of the energy gain due to bulk vs. thermal Comptonization. For very low values of δ , the emerging spectrum resembles the pure thermal Comptonization spectrum, whereas for higher bulk Comptonization, the hard tail evolves to a powerlaw-like shape.

The α -parameter is related to the electron temperature and the optical depth (see Farinelli et al. 2008, Eq. (10), for $\delta = 0$) and low values of α generally correspond to a high values of $kT_e \times \tau^2$. For a given electron temperature, which is a free parameter in the model, the optical depth can be inferred. Low α -parameters are required to produce the high-energy cutoff.

The `compmag` model

The `compmag` model describes thermal and bulk Comptonization of a black body seed spectrum in the cylindrical accretion flow onto the polar caps of a magnetized neutron star. It provides a numerical solution of Eq. (3.6) and does not require a particular velocity profile of the matter in the accretion column, which is necessary for an analytical solution. A detailed description of the model is given by Farinelli et al. (2012). The model is included in the standard release of XSPEC since version 12.8.0. It includes a second order bulk Comptonization term in the Kompaneets operator (see Psaltis &

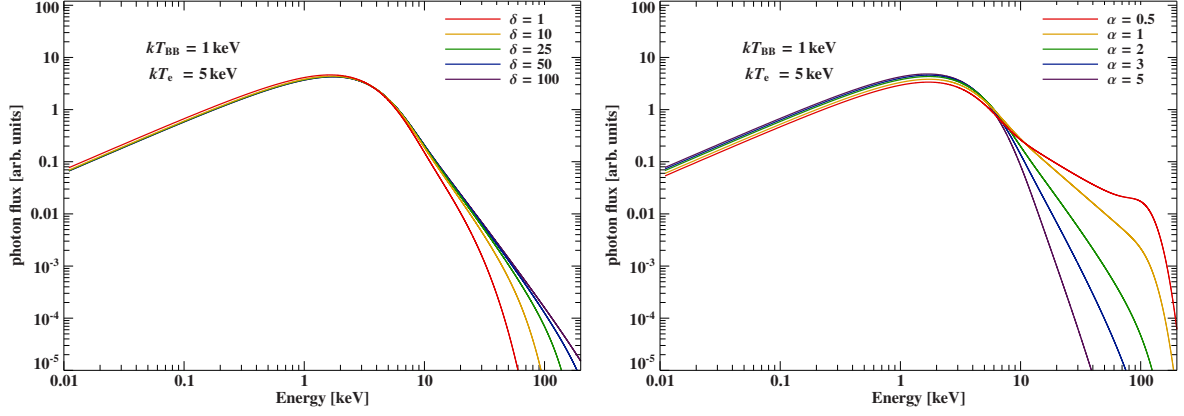


Fig. 3.9: Examples of spectra generated with the `compTB` model for different δ - and α -parameters. *Left:* Variation of the `compTB` model with a change of the δ -parameter, i.e., the bulk over thermal Comptonization ratio for $kT_{\text{BB}} = 1$ keV, $kT_e = 5$ keV, and $\alpha = 2$. *Right:* Variation of the `compTB` model with a change of the α -parameter, i.e., “efficiency” of the Comptonization $kT_{\text{BB}} = 1$ keV, $kT_e = 5$ keV, and $\delta = 20$.

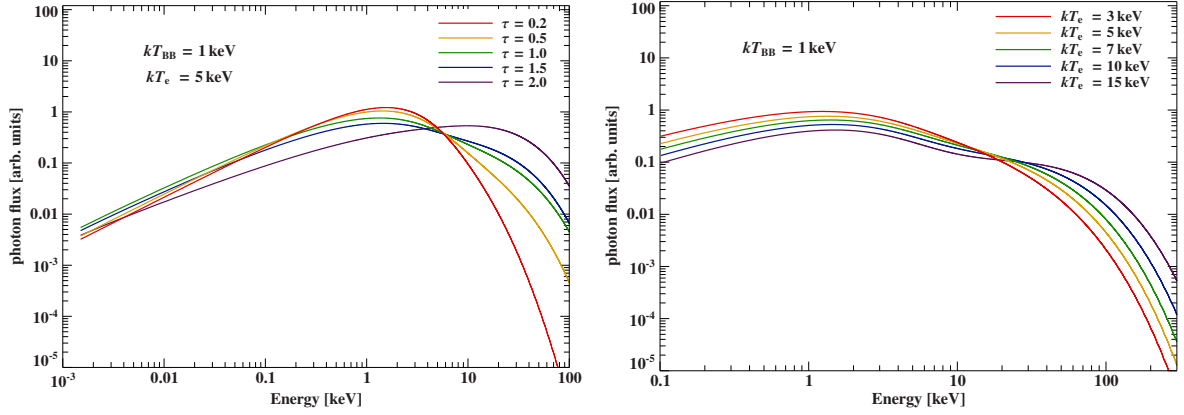


Fig. 3.10: Examples of spectra generated with the `compmag` model for different optical depths and electron temperature. The black body temperature is kept at 1 keV and the column radius of $0.25 R_S$, together with a linear velocity profile are assumed. *Left:* Variation of the `compmag` model with a change of the of the optical depth τ . *Right:* Variation of the `compmag` model with a change of the electron temperature.

Lamb 1997, for details) and allows certain choices of the velocity profile. A successful application of this model to observational data of RX J0440.9+4431, although limited by rather poor statistics, was presented by Ferrigno et al. (2013). The model parameters are the black body and electron temperature, the optical depth and radius of the accretion column, the “index and flag of the velocity profile”, the terminal velocity of the accretion flow at the bottom of the column and the albedo of the neutron star’s surface.

The optical depth determines, as can be seen from Fig. 3.10, the efficiency of the energy transfer from soft photons to hard photons. This is in agreement with the `compTB` model, where this efficiency was expressed in the spectral index α of the Green’s function. This efficiency is also characterized by the electron temperature, which also affects the high-energy cutoff (see Fig. 3.10). The interplay between the model parameters is, however, more complicated than these few examples might suggest. Farinelli et al. (2012) contains more examples of parameter variations and discussion on their effect on the spectral shape.

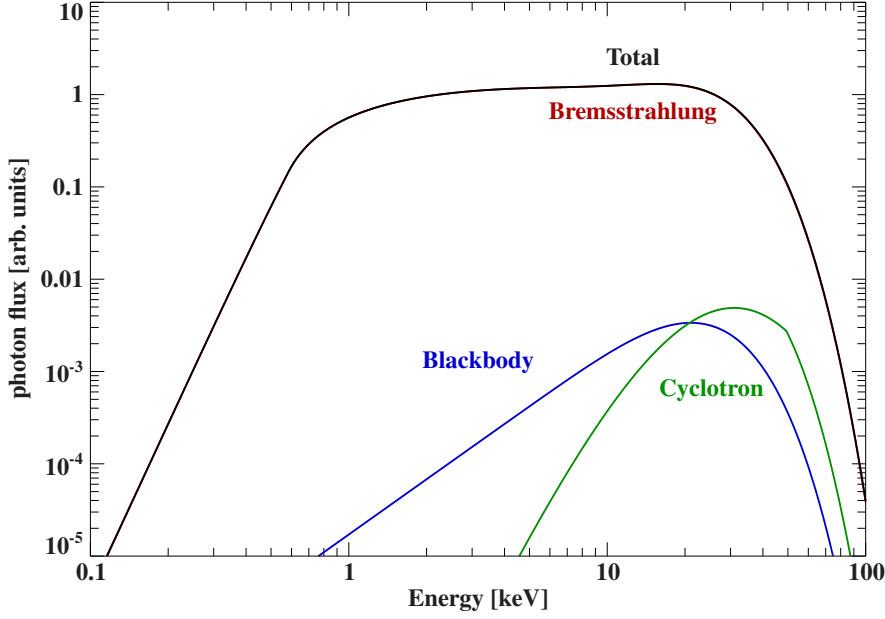


Fig. 3.11: Example spectrum of the BWcbbb model for the parameters: $\dot{M} = 2 \times 10^{17} \text{ g s}^{-1}$, $kT_e = 4.3 \text{ keV}$, $r_{\text{pol}} = 63 \text{ m}$, $B = 4.26 \times 10^{12} \text{ G}$, $\sigma_{\parallel} = 3.84 \times 10^{-5} \sigma_{\text{Thomson}}$ and $\bar{\sigma} = 1.91 \times 10^{-4} \sigma_{\text{Thomson}}$ with the individual Comptonized components of the different seed spectrum contributions of Bremsstrahlung (red), cyclotron emission (green) and black body radiation (blue).

Mike Wolff's BWcbbb model

This model is another implementation of the spectral formation model proposed by Becker & Wolff (2007). Unlike the compmag model, a velocity profile that is linear in the optical depth τ , is assumed here, making the radiative transport equation (Eq. (3.6)) separable in energy and space. Under this assumption the Green's functions can be calculated analytically and are convolved with a seed spectrum consisting of bremsstrahlung, black body and cyclotron emission. The individual seed photon sources can be selected by the user. The model is particularly designed for radiation dominated shocks, where the largest contribution to the observed spectrum originates from Comptonized bremsstrahlung and is therefore supposed to work in the high luminosity regime. It is still under development and not yet publicly available. The free model parameters are the mass accretion rate \dot{M} , the electron temperature kT_e , the radius of the accretion column r_{pol} , the magnetic field strength B , the distance and angle averaged and parallel (to the B-field) scattering cross sections σ_{\parallel} and $\bar{\sigma}$, respectively.

As mentioned before, the BWcbbb model spectrum is a sum of Comptonized black body, cyclotron emission and bremsstrahlung. Figure 3.11 shows the summed spectrum as well as the individual components. For radiation dominated shocks, bremsstrahlung plays the most dominant role as a source of seed photons. The temperature of the black body, which is a fit parameter in most other Comptonization models, is calculated from the mass accretion rate and the polar cap radius, arguing that the kinetic energy of the inflow at the thermal mound surface has to be radiated away and the temperature can be constrained via Stefan-Boltzmann's law. The cyclotron source term is mono-energetic, assuming a constant B-field inside the column but is distributed in space, due to the dependence of the collisional excitation rate on ρ^2 .

4 Observational methods

The following section gives a brief overview over the important characteristics of the X-ray satellites that have been used in this thesis.

4.1 *Suzaku*

Suzaku (also Astro-E2) was launched on 2010 July 10 as the rebuild of the Astro-E mission, which was lost during launch five years earlier. It was a joint mission of the Japan Aerospace Exploration Agency (JAXA) and the National Aeronautics and Space Administration (NASA). Unless otherwise noted, all technical descriptions refer to “The *Suzaku* Technical Description”¹ and the “The *Suzaku* Data Reduction Guide”².

The scientific payload consisted of three detectors: The *X-ray Imaging Spectrometers* (XIS), the *Hard X-ray Detector* (HXD) and the *X-ray Spectrometer* (XRS). The latter was an X-ray calorimeter, that unfortunately became unusable due to loss of the liquid He cryogen two weeks after launch (Kelley et al. 2007). Figure 4.1 shows a schematic of the satellite and the arrangement of the individual instruments.

The XIS consisted of four Wolter-Type I telescopes and CCD detectors (XIS0–3) providing an energy range 0.2–12 keV with an energy resolution of 130 eV at 5.9 keV after launch. The field of view (FoV) is $18' \times 18'$ (Koyama et al. 2007). The time resolution depended on the read-out mode and ranges from 8 s for the full “Window mode” to 1 s for the 1/8 Window mode, where the subsequently smaller areas of the CCD are read out. The “Clocking mode” could be set to Normal or Burst, with the latter one restricting the read-out in time. This also increased the time resolution but reduced the observing efficiency because a fraction of the 8 s frame is discarded. In Timing mode, where pixel data were summed up in y -direction and only read out in x -direction, 7.8 ms time resolution could be achieved. The XIS1 was back-illuminated, whereas all other XIS were front-illuminated. The back-illuminated configuration provided higher sensitivity at lower energy but it decreased more rapidly towards higher energies. The effective areas of all *Suzaku* instruments are shown in Fig. 4.2. In 2006, XIS2 was damaged by a micro-meteorite impact and became unusable³.

The HXD consisted of two detectors: The PIN Silicon diode array (PIN) and the GSO/BGO phoswich counter (GSO). Both detectors were placed together behind a collimator, limiting the FoV to $34' \times 34'$ below 100 keV and shielded by anti-coincidence detectors (Takahashi et al. 2007). The energy range of PIN was ~ 10 keV–70 keV, which was extended up to ~ 600 keV by GSO. The energy resolution of PIN was ~ 3 keV (FWHM) and $7.6/\sqrt{E_{\text{MeV}}}\%$ (FWHM) for GSO. The nominal time resolution of HXD was 61 μs .

Because of the imaging capabilities of XIS, its background could be measured during the observation at an appropriate off-source position of the chip. This was not possible for the HXD. Its background had to be simulated (Kokubun et al. 2007; Fukazawa et al. 2009). An alternative way to estimate the Non X-ray Background (NXB) of HXD is to use data taken during Earth occultation. The Cosmic X-ray background was always simulated according to Boldt (1987).

¹ ftp://legacy.gsfc.nasa.gov/suzaku/nra_info/suzaku_td.pdf

² also known as *Suzaku* ABC Guide, see ftp://legacy.gsfc.nasa.gov/suzaku/doc/general/suzaku_abc_guide.pdf

³ <http://www.astro.isas.jaxa.jp/suzaku/doc/suzakumemo/suzakumemo-2007-08.pdf>

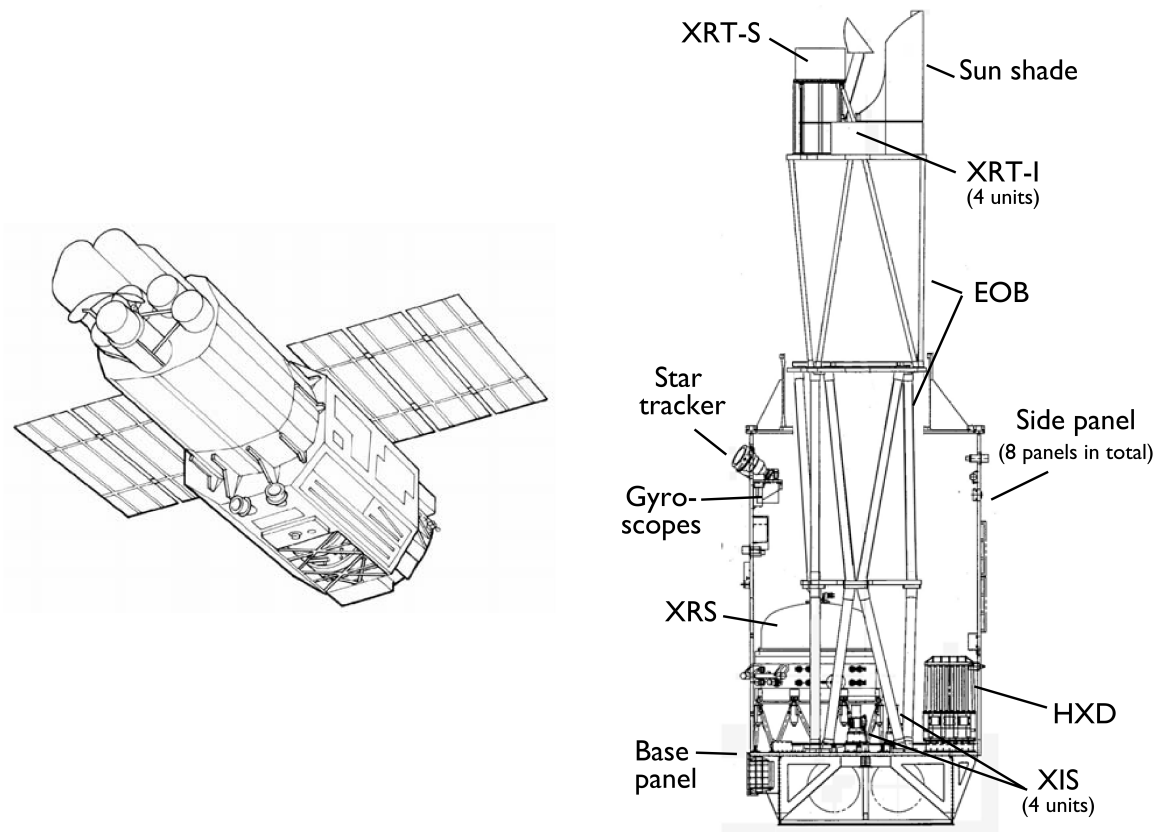


Fig. 4.1: Schematic sketch of the *Suzaku* satellite from the bottom (left) and side view with individual instruments (right). Taken from Mitsuda et al. (2007).

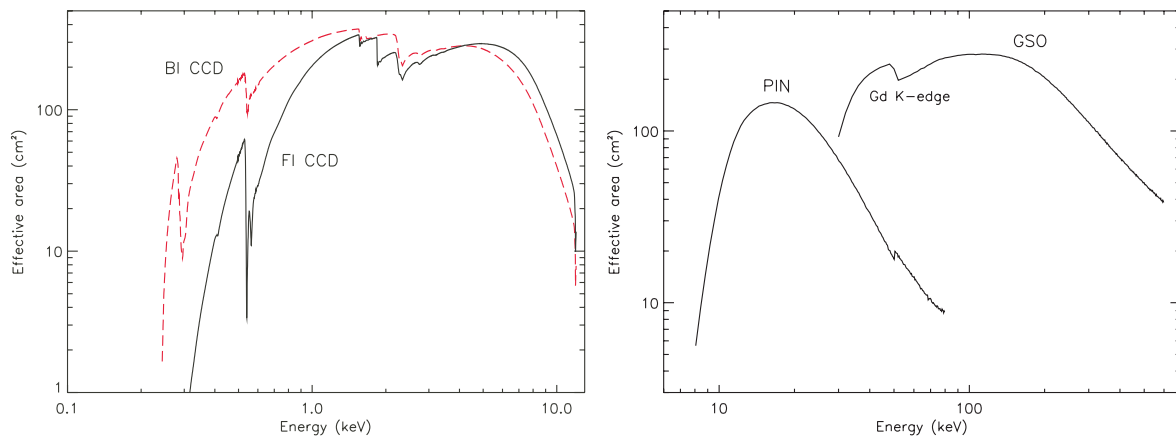


Fig. 4.2: Effective area of the XIS (left) and HXD (right) instruments onboard the *Suzaku* satellite. The XIS had different effective areas for the front- and back-illuminated configurations. The back-illuminated XIS1 has is more sensitive at energies below ~ 4 keV. Taken from Mitsuda et al. (2007).

The exposure times of the HXD have to be corrected for dead time. This is the time after an event occurred until the next event can be detected. This short time after each event, during which the detector is “dead” results overall in a reduction of the effective exposure. The dead time is measured using “pseudo events”. These are events that are artificially created by the analog HXD electronics. The triggered event rate is 4 cts s^{-1} and the pseudo events are flagged. The measured pseudo event count rate is then compared to the triggered count rate and the loss is ascribed to dead time in the

instrument and the exposure keywords are adjusted. To ensure statistical accuracy, the bin-wise dead time correction for lightcurves is only recommended for bin sizes larger than 128 s.

4.2 NuSTAR

The *Nuclear Spectroscopic Telescope Array* (NuSTAR) was launched on 2012 June 13 as a NASA small explorer mission. The primary reference for all technical details is [Harrison et al. \(2013\)](#). It consists of two co-aligned grazing incidence X-ray telescopes and solid-state detector and is sensitive to the energy range of 3–79 keV. The optics are built of 133 nested shells with a FoV of $10' \times 10'$ at 10 keV. The detectors placed in the focal plane of each optical module (called FPM-A and FPM-B) is not a traditional Si-bases CCD but a pixeled CdZnTe detector. It uses a deployable mast to reach the required focal length of more than 10 m. The detectors are actively shielded by CsI detectors. The pixels are read out individually upon triggering. This approach avoids pile-up, which is a severe problem in many other imaging X-ray detectors employing CCDs (e.g., *Suzaku*-XIS), which does not occur up to incident count rates of $\sim 10^5$ cts/s/pixel. However, due to the read-out and processing time of each event, the maximum number of events per module that can be detected is limited to ~ 400 . Because of the accurate determination of the dead time, fluxes can be measured to 1 % up to 10^4 cts/s ([Bachetti et al. 2015](#)). The on board data storage is limited to 2.8 Gbit and ground station contact is provided four times per day in nominal science operations. If the data rate is higher, additional ground station contacts can be scheduled but if the data volume increases unexpectedly, data may be overwritten before download⁴. The time resolution is $2 \mu\text{s}$. The energy resolution of the is roughly by a factor of two worse compared to the CCD energy resolution of e.g. *Suzaku*-XIS with ~ 400 eV at 10 keV. NuSTAR is the first mission providing imaging capabilities of Wolter Type-I optics at energies up to almost 80 keV. The most common method to obtain images in the hard X-ray regime is the coded mask technology which is applicable to even higher energies, though generally at worse resolution (e.g., IBIS onboard *INTEGRAL*, [Ubertini et al. 2003](#)).

4.3 Swift

The *Swift* Gamma Ray Mission, launched on 2004 November 20, is a multi-wavelength observatory, particularly dedicated to detect and follow-up Gamma Ray Bursts (GRBs, [Gehrels et al. 2004, 2005](#)). It carries three detectors for optical/UV and X-ray observations. A schematic picture of the spacecraft and the instruments is shown in Fig. 4.4. A discussion of the detector modes and effects is also given by [Krauß \(2013\)](#).

The *Burst Alert Telescope* (BAT) is a wide FoV coded mask detector, consisting of more than 32 000 CdZnTe detectors and ~ 52 000 mask elements. It covers an energy range of 15–50 keV and 1.4 sr of the sky at a time ([Barthelmy et al. 2005](#)). It was designed to detect and localize GRBs to less than $4'$ precision to trigger immediate slew of the other instruments to the direction of the GRB for follow-up observations. BAT also performs an all-sky survey and monitors transient sources. Orbital and daily lightcurves in the 15–50 keV band are almost in real-time publicly available for currently more than 1000 sources on the *Swift*/BAT Hard X-ray Transient Monitor webpage⁵ ([Krimm et al. 2013](#)).

The *Ultraviolet/Optical Telescope* (UVOT) is a 30 cm Ritchey-Chrétien telescope with a set of 11 filters to cover the wavelength range of 170–600 nm. It is capable of detecting a 24 mag B star in white light in ~ 1000 s and has a FoV of $17' \times 17'$ ([Roming et al. 2005](#)).

The *X-ray Telescope* (XRT) was designed for X-ray follow-up observations of GRBs at higher spectral and spatial resolution than provided by BAT. Similar to *Suzaku*-XIS it uses a grazing incidence

⁴ see the “NuSTAR Observatory Guide” at https://heasarc.gsfc.nasa.gov/docs/nustar/nustar_obsguide.pdf

⁵ <http://swift.gsfc.nasa.gov/results/transients/>

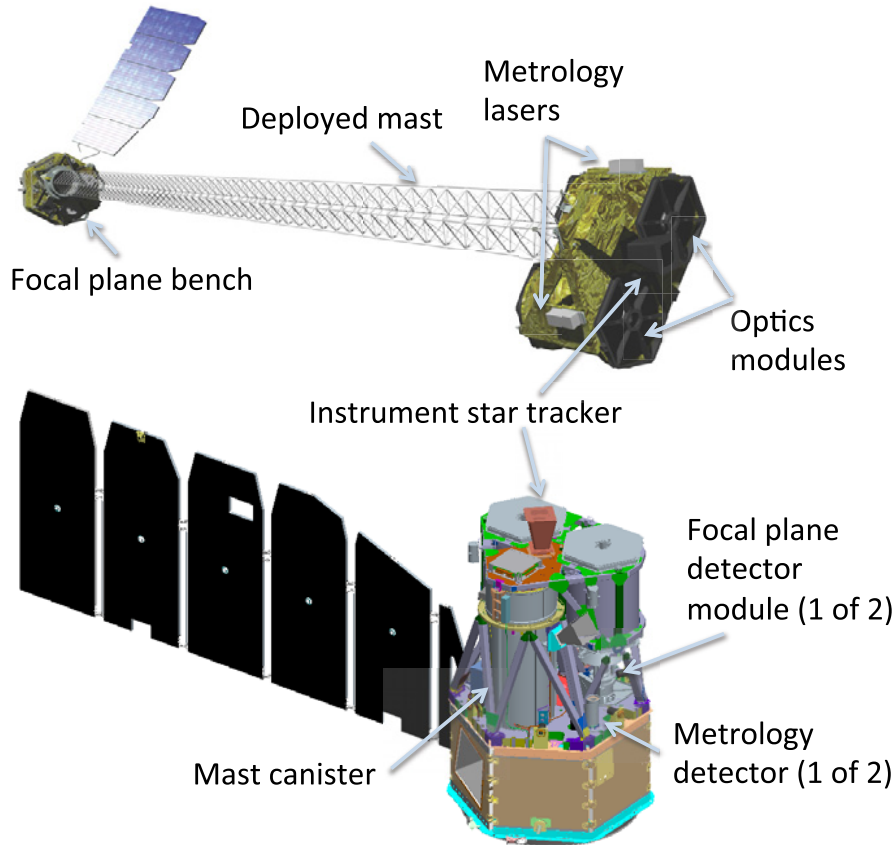


Fig. 4.3: Drawing of the *NuSTAR* satellite in stowed configuration (bottom) and with the mast deployed (top). The deployable mast is necessary to reach the focal length of 10.14 m which would not fit in the launch vehicle. The alignment of the optics and the detector module is measured by the metrology system, which consists of two IR lasers mounted to the optics pointing at a detector mounted to the focal plane module. The laser spot is tracked and the alignment can be recorded. Image taken from [Harrison et al. \(2013\)](#)

Wolter Type-I optics and CCD detectors with a energy range of 0.2–10 keV. The effective area of 125 cm² at 1.5 keV ([Burrows et al. 2005](#)) is considerably smaller than *Suzaku*-XIS. Although its main purpose is to observe GRBs and GRB afterglows, the meantime is available for other observations and *Swift* carries out a large number of Target of Opportunity (ToO) observations and has regular observing campaigns with, e.g., *NuSTAR*.

Again, similar to *Suzaku*-XIS, the XRT has several observing modes, to satisfy a large range of requirements with respect to observable luminosity and time resolution. In the “Photon Counting mode”, the whole CCD is read out every 2.5 s, providing a full 2D image. While this is required for source positioning, observations of bright sources are affected by severe pile-up and the “*Swift* XRT Data Reduction Guide”⁶ recommends to not use this mode for sources brighter than 1 mCrab. In the “Window Timing Mode”, only 200 columns of the central region of the chip are read out and the pixel values are summed up. The time resolution is increased significantly with 1.7 ms but at the prize of the loss of one spatial dimension. This mode is recommended for observations between 1–600 mCrab. Pile-up is becoming an issue for count rates of more than 100 cts s⁻¹ ([Mineo et al. 2006](#)). The big disadvantage of the Window Timing mode is the source position cannot be determined from the image and pointing offsets or attitude instabilities cannot be corrected. This can affect the Response Matrix File (RMF) and because of this problem, several position dependent RMFs are released as part of the

⁶ see http://swift.gsfc.nasa.gov/analysis/xrt_swguide_v1_2.pdf

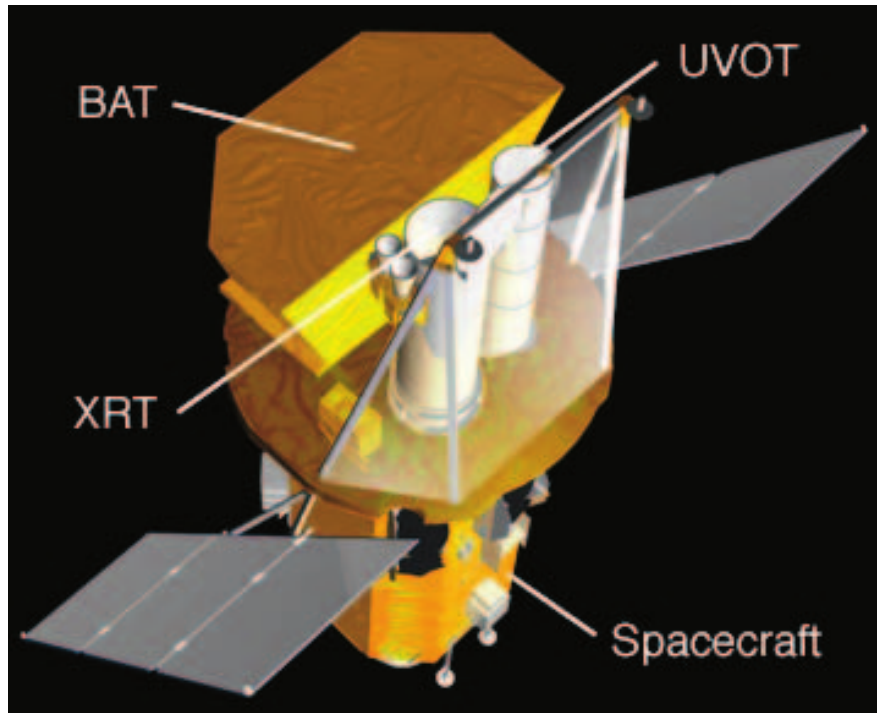


Fig. 4.4: Picture of the *Swift* spacecraft and instruments. Image taken from Gehrels et al. (2004)

Calibration Database (CALDB)⁷. The other available modes are the “Image Mode” and the “Photon Diode Mode”, which are used almost only for GRB observations. During the Image Mode, the entire CCD is read out without any event recognition⁸. The Photon Diode Mode offers the highest time resolution of 0.14 ms but has no imaging capabilities. It is used for very bright sources only (up to 60 Crab).

Figure 4.5 shows a comparison of the effective areas of some of the instruments discussed previously. *Swift*-XRT and *Suzaku*-XIS cover the same energy range but the effective area of the XRT is by a factor of $\sim 2-3$ lower compared to one XIS module. *NuSTAR* exceeds the total effective area of XIS around the iron $K\alpha$ energy and is more sensitive than PIN. Although the effective area of GSO is again larger compared to *NuSTAR* and covers a wider energy range, it should be noted, that the huge advantage of *NuSTAR* is its imaging capabilities, which make the detector background much better manageable and its good energy resolution.

⁷ for more details about the impact of source position uncertainties and the application of position dependent RMFs, see the release note at http://www.swift.ac.uk/analysis/xrt/files/SWIFT-XRT-CALDB-09_v20.pdf

⁸ In the Photon Counting mode, also the whole CCD is read out, but only pixels above a certain threshold are registered as X-ray events and the 3×3 pixel values around this event are sent to telemetry and a grade – depending on the charge distribution in these pixels – is assigned

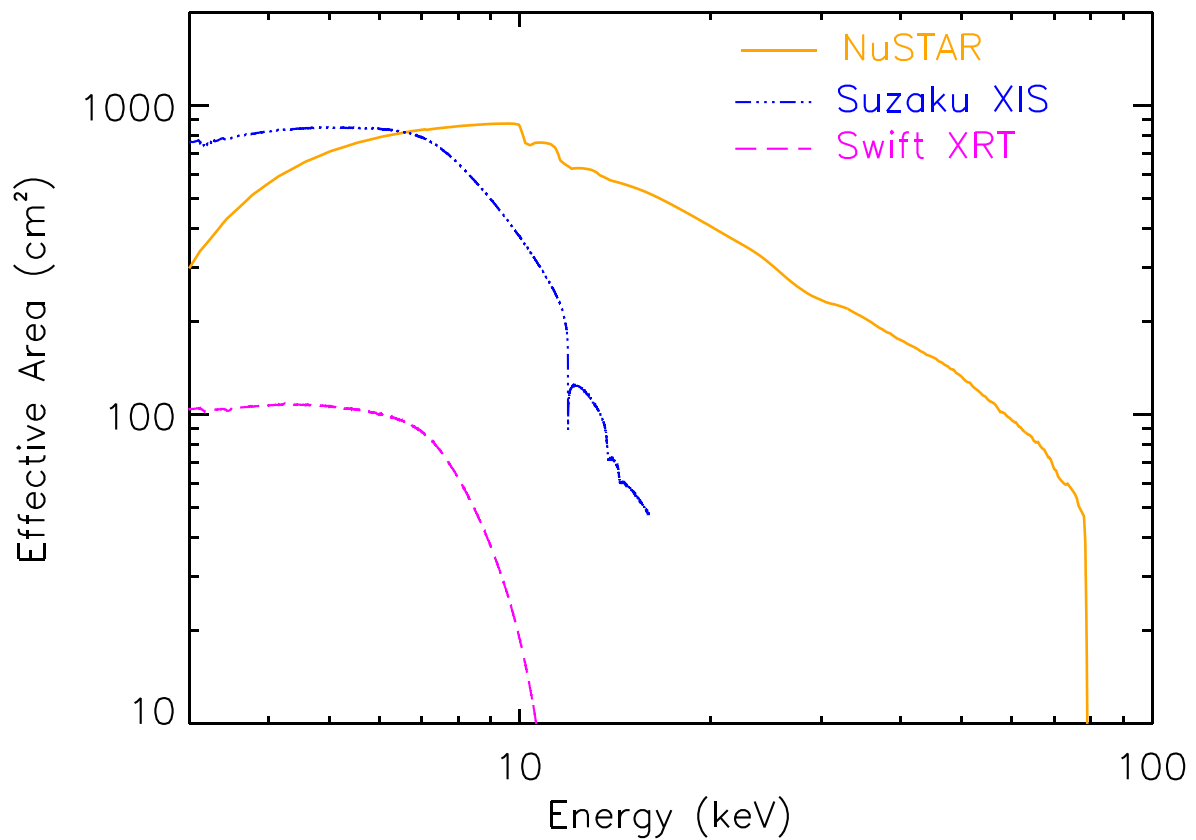


Fig. 4.5: Comparison of the effective areas of the *Suzaku*-XIS, *NuSTAR*-FMPA/B and *Swift*-XRT instruments. Note, that for *Suzaku* the summed effective area of all four XIS modules is shown. Adapted from Harrison et al. (2013).

5 *Suzaku* observations during the 2013 outburst of KS 1947+300

The following chapter presents an analysis of the spectral and timing behavior of KS 1947+300 using data of these *Suzaku* observations and one of the *NuSTAR* observations. The results have been submitted for publication (Ballhausen et al. 2015) and some information is taken in verbatim from there.

5.1 KS 1947+300 – a brief overview

KS 1947+300 is an accreting X-ray pulsar in the vicinity of Cygnus X-1, which was discovered on 1989 June 8 by the TTM coded mask spectrometer onboard the *Kvant* module of the Mir space station during observations of the nearby source GS 2023+338 (Borozdin et al. 1990). The *Kvant*-TTM instrument covered an energy range of 2–30 keV and the spectral model applied to the data was an absorbed powerlaw of photon index 1.72 ± 0.31 and column density $(3.4 \pm 3.0) \times 10^{22} \text{ cm}^{-2}$.

In 1994, the Burst and Transient Spectrometer Experiment (BATSE) all-sky monitor onboard the *Compton Gamma Ray Observatory* (CGRO) discovered a 18.7 s pulsar in the Cygnus region independently, which was catalogued as GRO J1948+32 (Chakrabarty et al. 1995). The identity of KS 1947+300 and GRO J1948+32 was proven by Swank & Morgan (2000) by a comparison of the pulse periods.

In 2000/2001, KS 1947+300 underwent another major outburst, which was densely monitored by the *Rossi X-ray Timing Explorer* (XTE). More than 130 pointed observations were taken from 2000 to 2002. Galloway, Morgan & Levine (2004) presented spectral and timing analyses of these observations and reported orbital parameters. The eccentricity was found to be $e = 0.033 \pm 0.013$, the orbital period $P_{\text{orb}} = 40.415 \pm 0.010 \text{ d}$ and the projected semi-major axis $a \sin i = 137 \pm 3 \text{ lt-s}$. The authors also found a frequency glitch to be occurred during the outburst, which are rarely seen in accretion powered X-ray pulsars. The spectral model that they found to work most successfully was the *compTT* model (see Sect. 3.3.2) together with a soft black body component and a Gaussian iron $K\alpha$ fluorescent line.

The RXTE observations have been analyzed together with a set of *INTEGRAL* observations taken from 2002 to 2004 by Tsygankov & Lutovinov (2005) with particular emphasis on the pulse profile evolution and luminosity dependence. The applied continuum model was a powerlaw modified by a high-energy cutoff (*highcut*), different from what has been reported in Galloway, Morgan & Levine (2004).

Naik et al. (2006) reported on broad-band X-ray spectroscopy of KS 1947+300 using data taken with the *BeppoSAX* satellite during the decline of the 2000/2001 outburst. The applied continuum model was again the absorbed *compTT* model, modified by a black body of $\sim 0.6 \text{ keV}$ temperature and a Gaussian emission component to account for iron $K\alpha$ emission. The iron line energy was $\sim 6.7 \text{ keV}$, higher than what has been observed by RXTE during the same outburst. This may be partly due to the energy calibration uncertainties between the different instruments but also hints at multiple ionization states of iron, even if those could not be resolved with the available energy resolution. Pulse phase resolved spectral analysis was carried out by these authors for the first time for this source. Variation over pulse phase was found – except for the individual normalizations of the model components – the optical depth and, though less constrained, the electron temperature. It should be noted, however, that

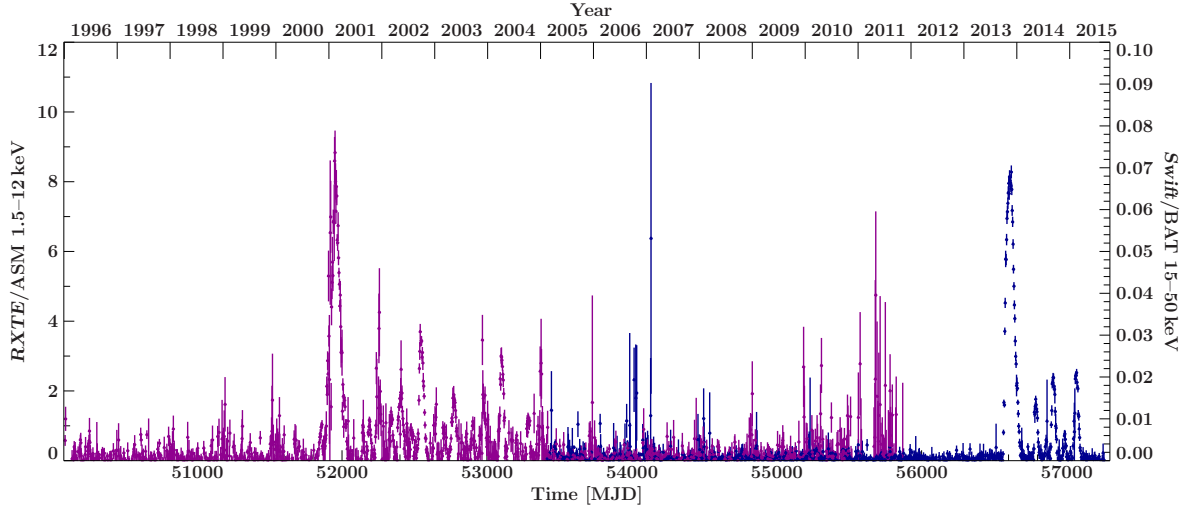


Fig. 5.1: *RXTE*/*ASM* (purple) and *Swift*/*BAT* lightcurve (blue) of KS 1947+300 with a resolution of three days.

several model parameters had to be fixed to the phase averaged values to avoid degeneracies.

Optical spectroscopy and photometry by [Negueruela et al. \(2003\)](#) allowed the classification of the optical companion of KS 1947+300 as a B0Ve star with an approximate distance of 10 ks.

After the 2000/2001 outburst, the source showed minor activity until 2004, still monitored by *INTEGRAL* ([Tsygankov & Lutovinov 2005](#)) and then turned to quiescence for almost ten years. In 2013 October, another outburst occurred which was monitored by *Swift*, *NuSTAR* and *Suzaku*. The *RXTE*/*ASM* and *Swift*/*BAT* lightcurve is shown in Fig. 5.1. The *NuSTAR* observations revealed the presence of a cyclotron line at 12.2 keV ([Fürst et al. 2014](#)). This is remarkable because no other observation of the previous outbursts has detected a cyclotron line, although the *RXTE*-PCA instrument covers the cyclotron line energy and observations were made at very different luminosities. In fact, [Fürst et al. \(2014\)](#) found the cyclotron line to be of different strength in the three *NuSTAR* observations. The best-working continuum model was an absorbed cut-off powerlaw (cutoffpl) with a black body of ~ 0.6 keV temperature.

Since the 2013 outburst, KS 1947+300 showed ongoing activity X-rays in a series of subsequent outbursts until early 2015 ([Finger et al. 2014](#); [Kühnel et al. 2014](#); [Finger, Jenke & Wilson-Hodge 2015](#)). Optical observations revealed an increase in the $H\alpha$ equivalent widths right before and during X-ray activity ([Ozbey-Arabaci et al. 2014](#); [Camero-Arranz, Ozbey-Arabaci & Caballero-Garcia 2014](#)).

As mentioned above, KS 1947+300 underwent an outburst again in 2013 after almost ten years of quiescence, that was also monitored by *Suzaku*, *NuSTAR* and *Swift*.

5.2 Data Aquisition and Reduction

Suzaku observed KS 1947+300 on 2013 October 22 during rise and on 2013 November 22 at the peak of the outburst for 29.0 ks and 7.6 ks, respectively. *NuSTAR* observed the source three times but only the second observation (ObsID 80002012004) with 18.8 ks exposure is used in this work. An analysis of all three *NuSTAR* observations and several *Swift* pointed observations is reported by [Fürst et al. \(2014\)](#). Figure 5.2 shows a close-up of the *Swift*/*BAT* lightcurve with the times of the *Suzaku* and *NuSTAR* observations marked. The second *NuSTAR* observation overlaps with the second *Suzaku* observation.

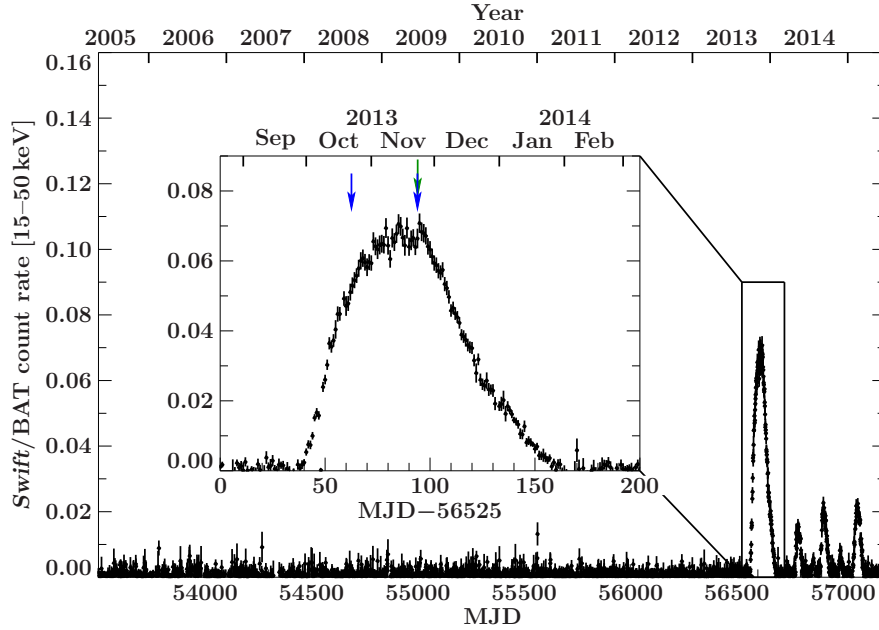


Fig. 5.2: Close-up of the *Swift*/BAT lightcurve of KS 1947+300 with the times of the two *Suzaku* observations (blue) and the one *NuSTAR* observation (green) used in this work marked. Adapted from Ballhausen et al. (2015)

5.2.1 *Suzaku*

XIS was operated in 1/4 Window mode during both observations and in Normal Clocking Mode during the first (Obs. I) and Burst Mode during the second observation (Obs. II), increasing the available time resolution from 8 s to 2 s.

The HEASoft software package (v. 6.15.1) was used for data reprocessing. The FTOOL *aepipeline* was run on both datasets to apply the latest calibration to the raw data and screen the event files to produce so-called “cleaned event files”. In the calibration step, Good Time Interval (GTI) files are generated for both XIS and HXD where telemetry did not suffer from saturation. This happens when the telemetry quota, that depends on the current data rate (it is different, e.g., on weekends and weekdays), is exceeded and is a problem especially when observing bright sources. Event times and, for XIS, sky coordinates are assigned using time calibration and attitude files. Finally the event energies are calculated (in terms of PI values) using the latest gain calibration and event grades are assigned, depending on the charge distribution. In the screening stage, events are removed that occurred, during or close SAA passages, during slews or low elevation angles or at low telemetry rates. Additionally, a grade selection is applied and columns of bad Charge Transfer Efficiency (CTE) in XIS and low voltage events in HXD are removed.

All event times were transferred to the Solar barycenter using the *Suzaku*-specific FTOOL *aebarycen*. This is necessary because all event times are recorded in the satellite’s inertial frame, and are Doppler-shifted due to the satellite’s orbital motion around the Earth and the Earth orbiting around the Sun plus relativistic effects due to the gravitational potential in the solar system.

The CALDB versions used for data reprocessing and calibration are v20110630 for XRT, v20110913 for HXD, and v20130916 and v20131231 for the first and second XIS data set.

The sky image of the first observation showed two sources that are not displayed in the detector image (see Fig. 5.3). The transformation from detector to sky coordinates is not working correctly. In principle it is not a problem to perform all data extraction in the detector coordinate system but the disadvantage of this approach is that no additional attitude correction can be performed, which is recommended by default. Attitude correction refers to the correct the attitude file for “thermal

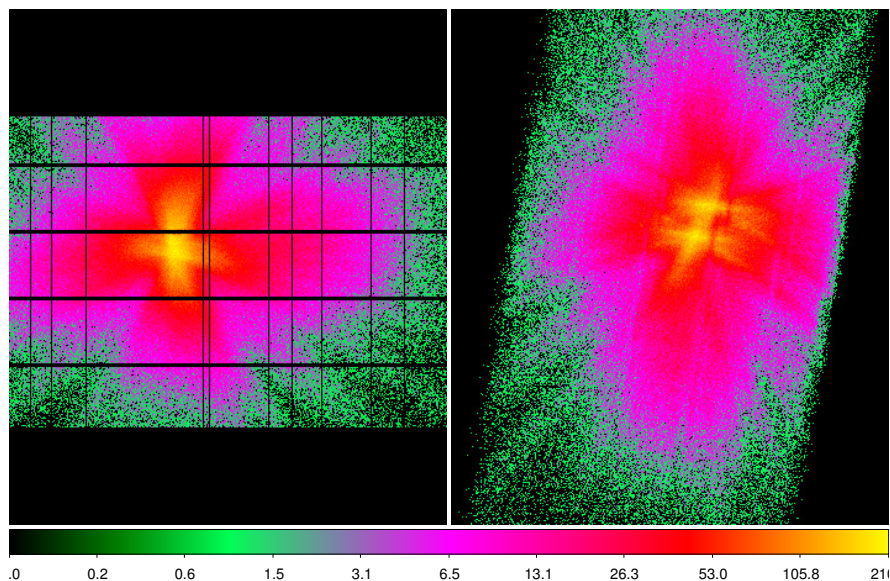


Fig. 5.3: DS9 image of the XIS3 3×3 mode of Obs. I in detector (left) and sky coordinates (right). The black stripes in the detector image are charge injection columns. The sky image clearly shows two sources. The source in the detector image looks slightly blurred. The colorbar shows the total counts per pixel.

Table 5.1: Log of the *Suzaku* observations.

Obs. No.	ObsID	mid-time [MJD]	XIS exposure [ks]	HXD exposure [ks]
Obs. I	908001010	56587.58	29.0	27.5
Obs. II	908001020	56619.02	7.6	29.7

wobbling”, i.e., an apparent change of the source position due to distortions of the optical system caused by temperature gradients. In many cases, the attitude can be improved with the FTOOL `aeattcor2`, which is based on an ISIS routine by Mike Nowak¹ and which splits the observation in shorter snapshots (typically of 128 s) and determines the source position and tracks it during the observations. The deviations of the nominal source position are then used to generate an updated attitude file (see Uchiyama et al. 2008, for details). The result is a more sharply defined source image. For Obs. II, no problems occurred during the event coordinates transformation and `aeattcor2` was applied to the event files.

The source regions are annuli with outer radii of 125 pixels for Obs. I and $90''$ for Obs. II. Both observations were checked for pile-up using the FTOOL `pileest`, that calculates the probability for two or more events to happen during one read-out cycle using Poisson statistics from the expected count rate in the absence of pile-up. The pile-up probabilities are then mapped and areas of estimated pile-up fraction of more than 4% were excluded from the source regions. Circular background regions of the same size as the outer radius were chosen at the outer region of the CCD chip.

As HXD has no imaging capabilities the events are directly binned into spectra and lightcurves. The applied PIN response is of epoch 11 for the XIS nominal pointing position and the “tuned” background version 2.2 is used as Non X-ray background (Fukazawa et al. 2009). The GSO “correction ARF” was applied to both observations as recommended by the *Suzaku* Data Analysis Guide (see also Yamada et al. 2011).

The observation log is given in Table 5.1.

¹ <http://space.mit.edu/cxc/software/suzaku/aeatt.html>

5.2.2 NuSTAR

The *NuSTAR* observation that had the most overlap with the *Suzaku* observation was also included in the analysis. The raw data was reprocessed using `nupipeline` v. 1.4.1 which is part of `HEASoft` v. 6.16. The CALDB version at the time of data extraction was 20150316. The `FTOOL` `nupipeline` performs similar tasks as `aepipeline`, though obviously with different screening criterias. The event processing time for each event is 2.5 ms, so dead time becomes significant for count rates of more than 50 cts s⁻¹ per module².

The source and background regions are circles with 130'' and 105'' radii, respectively. Again, all event times were transferred to the solar barycenter.

5.3 Timing analysis

XIS and PIN lightcurves with 128 s time resolution were extracted for both observations. While the count rates during Obs. II are higher, they do not show a significant variation or flaring during the individual observations. The hardness ratio was determined by taking the ratio of the background-subtracted count rates in the 7–10 keV and 1–4 keV bands. The XIS3 and PIN lightcurves, as well as the hardness ratio is shown in Fig. 5.4. The hardness ratio does not change significantly between the two observations.

The pulse periods were determined with the epoch folding technique as described by Leahy et al. (1983). This method has the advantage – compared to standard periodicity searches via Fourier transform – that it works also for unevenly spaced lightcurves with gaps. The lightcurve is folded on a set of test periods and the pulse profiles are then compared to a flat distribution, i.e., a constant. If the correct pulse period is matched, the pulse profile is expected to have the most distinct shape, whereas for any other period the pulse profile will be evened out if a high number of pulses is averaged. The deviation from the flat distribution is then expressed as a χ^2 value and the pulse period is found by taking the test period where the χ^2 distribution has its maximum.

As the time resolution of PIN is much higher than that of XIS and the PIN has longer exposure in total (and therefore covers more pulses), the PIN data will give the most accurate pulse period. The determined pulse periods are 18.80876(7) for Obs. I and 18.78896(7) for Obs. II. The uncertainties are determined in a Monte Carlo approach: for the found pulse period and pulse profile lightcurves are simulated with additional Poisson noise. The epoch folding is then repeated for these simulated lightcurves and the standard deviation of the distribution of the obtained pulse periods is then the assumed uncertainty on the pulse period.

Pulse profiles of different energy bands for both observations are shown in Fig. 5.5. In the XIS energy range, the pulse profiles look rather sinusoidal, although the exact shape is difficult to determine because of the limited time resolution of XIS of 2 s. Since the pulse period is ~ 18.8 s this allows only for 9 independent phase bins. The high time resolution of PIN allows to resolve the pulse profiles in much more detail above 12 keV. The harder pulse profiles show a second, narrow minimum and peak right after the main minimum. This feature gets more distinct as energy increases. The morphology and evolution is rather unusual for accreting X-ray pulsars, but has been observed in this source in previous outbursts (see, e.g., Tsygankov & Lutovinov 2005; Naik et al. 2006).

The pulse profile evolution below 12 keV can be studied in much more detail using *NuSTAR*. Figure 5.6 shows the count rate distribution of the *NuSTAR* observation as a function of pulse phase and energy. It consists of 40 energy resolved lightcurves, folded to 60 bins pulse profiles. To account for the powerlaw-like decrease of count rate with energy, all pulse profiles are normalized to their mean count rate and given in units of their standard deviation. In this way, each row of the map represents an

² http://www.nustar.caltech.edu/uploads/files/CIT_Memo_FPE_livetime.pdf

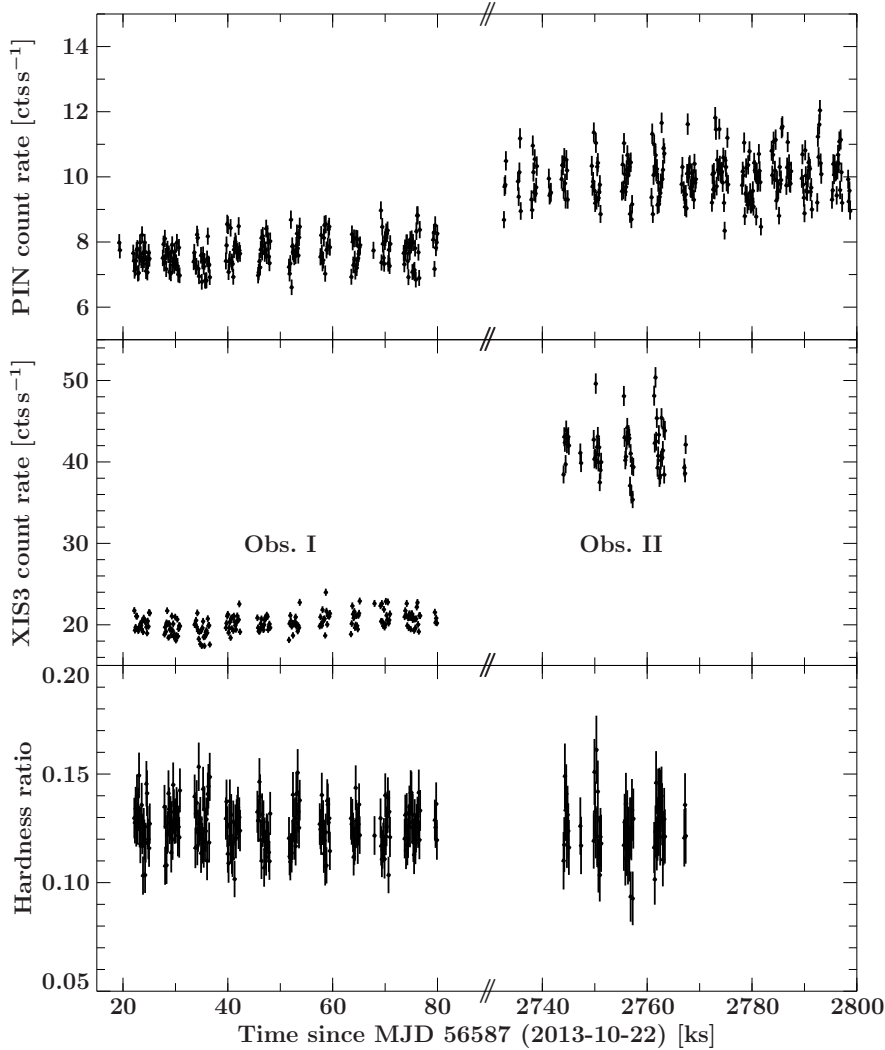


Fig. 5.4: Background-subtracted lightcurve and hardness ratio of the two *Suzaku* observations with 128 s bin size. The upper and middle panel shows the PIN lightcurve in the 15–70 keV band and XIS3 lightcurve in the 1–10 keV band, respectively. The lower panel shows the hardness ratio measured with XIS3 and defined as the count rate ratio of the 7–10 keV to the 1–4 keV band. Adapted from [Ballhausen et al. \(2015\)](#).

energy resolved pulse profile and each column would represent a phase resolved spectrum, if the pulse profiles had not been normalized which destroys the spectral information.

However, comparing Figs. 5.5 and 5.6 shows that the formation of the second, narrow peak already starts around 6 keV, which could not be resolved with *Suzaku* alone. It is of comparable strength as the main peak from ~ 15 keV onwards and even exceeds the main peak above ~ 30 keV. This is in excellent agreement with the PIN profiles of Obs. I. There are no phase shifts detected in the pulse profile evolution. The pulse profiles of Obs. I and Obs. II are very similar in shape, although the emerging second peak is slightly weaker in Obs. II.

5.4 Phase averaged spectroscopy

For spectral analysis, the energy range of XIS was restricted to 1–10 keV for XIS0 and 3, and 1–8 keV for XIS1 to reduce calibration uncertainties of the response. Additionally, the energy ranges 1.72–1.88 keV and 2.19–2.37 keV were excluded for all XIS because of known detector features of Au and

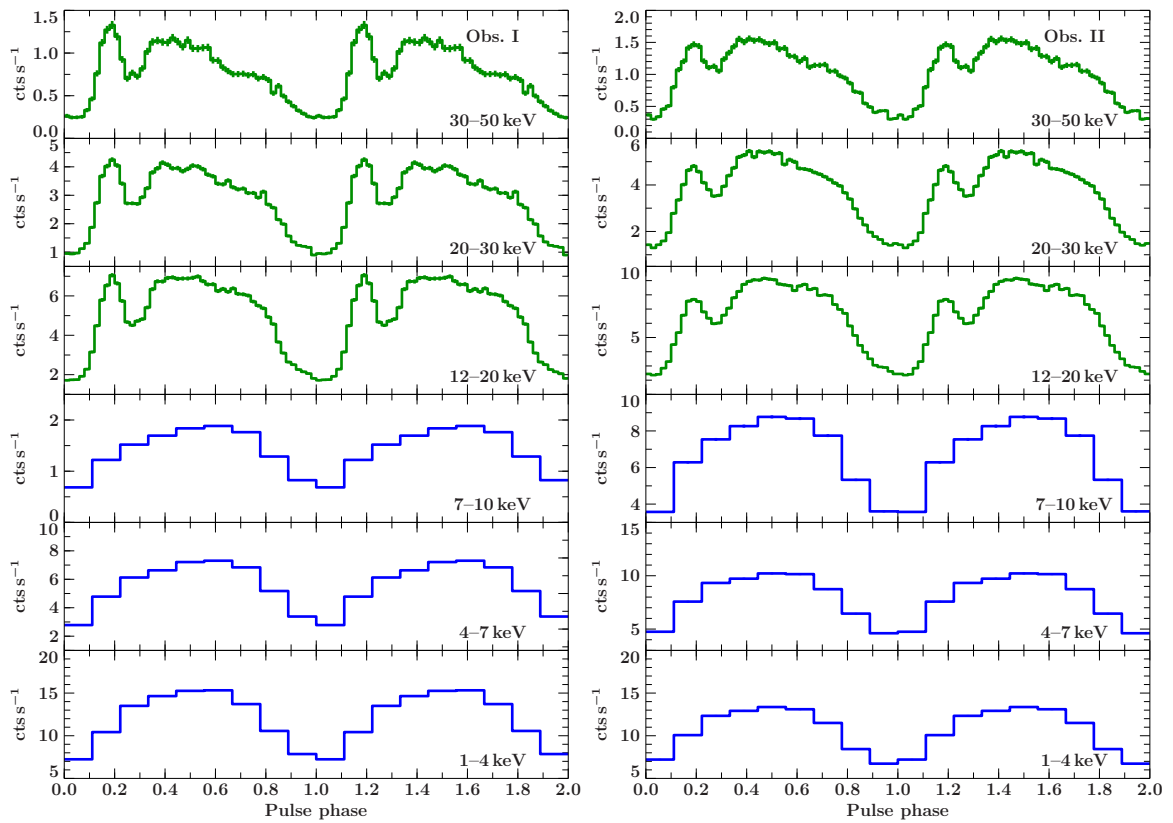


Fig. 5.5: Background subtracted pulse profiles of both *Suzaku* observations for different energy bands of PIN (green) and XIS0 (blue). All profiles are shown twice for clarity.

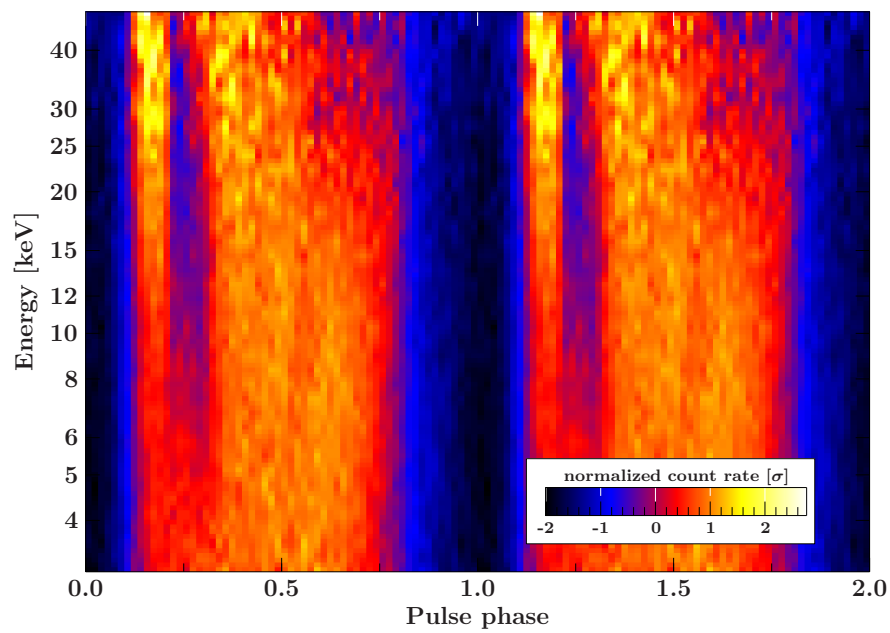


Fig. 5.6: Map of the count rate distribution of the *NuSTAR* observation as a function of energy and pulse phase. Taken from Ballhausen et al. (2015).

Si (Nowak et al. 2011). The HXD energy range used is 15–70 keV for PIN and 70–90 keV for GSO. The XIS spectra were jointly rebinned to a minimum signal-to-noise ratio (SNR) of 80 for Obs. I and 70 for Obs. II. For the energy range 6–7 keV, the required SNR was reduced to 65 for Obs. I and 50 for Obs. II to ensure a finer energy resolution in the iron line region. The PIN spectra of both observations were rebinned to a minimum SNR of 25 and for GSO channels were rebinned by a factor of 4. The *Interactive Spectral Interpretation System* (ISIS v1.6.2, Houck & Denicola 2000) was used for all spectral fitting.

The applied continuum to the phase averaged spectrum of KS 1947+300 is an absorbed powerlaw with high-energy cutoff (cutoffpl) with an additional black body of ~ 0.6 keV temperature with abundances and absorption cross sections set to the values of Wilms, Allen & McCray (2000) and Verner et al. (1996), respectively.

To model the $K\alpha$ emission of neutral iron at 6.4 keV, a narrow Gaussian emission line was added to the model for both observations. The line width was fixed to 10^{-6} keV which is reasonable if the intrinsic line width is much smaller than the detector energy resolution of ~ 190 eV in 2009 (Ozawa et al. 2009) and might be already lower because of a decrease of the CTE due to radiation damage in orbit. If $K\alpha$ emission is detected, from our understanding of atomic physics there must also be $K\beta$ emission and the energy difference and the respective transition probabilities, i.e., the ratio of the line fluxes are known. Therefore, adding another Gaussian emission line to account for $K\beta$ emission, with fixed line width and energy and flux tied to the values of the $K\alpha$ does not introduce further fit parameters and such a line with 13% flux of the $K\alpha$ at 0.65 keV higher energy was added to the model (Palmeri et al. 2003).

Adding the neutral $K\alpha$ line improved the fit significantly but still left over line-like residuals in the iron band. Adding second narrow Gaussian emission line at ~ 6.7 keV and – only for Obs. I – a third one at ~ 6.9 keV eventually resulted in an acceptable fit.

Figure 5.7 shows the iron line region of Obs. I. with different model components included. For clarity, all XIS are combined for plotting but fitted individually. The different emission features are interpreted as $K\alpha$ lines from neutral, He-like and H-like iron. For Obs. II, a H-like iron $K\alpha$ line could not be detected significantly, probably because of the worse SNR due to the shorter exposure and is therefore not included in the model.

KS 1947+300 is a newly established cyclotron line source with a line energy of 12.2 keV (Fürst et al. 2014). The cyclotron line was discovered in *NuSTAR* observations partly simultaneous with the *Suzaku* observation. Unfortunately, the line centroid energy is exactly in the gap between XIS and PIN, so it cannot be detected with *Suzaku*. However, the cyclotron line has a width of a few keV and thus its wings can reach into the energy range covered by the *Suzaku* instruments. The cyclotron line was therefore added to the model although the line energy and width had to be fixed to the values from Fürst et al. (2014) because they cannot be constrained with the available data. The inclusion of the cyclotron line indeed improved the fit quality and is therefore in agreement with Fürst et al. (2014). It should be noted, however, that the detector responses, especially PIN, are not very good calibrated at the lower energy limit, so a detection of the cyclotron line cannot be concluded.

The spectrum and best fit model of Obs. I is shown in Fig. 5.8, which also illustrates the impact of the cyclotron line and iron line component. The photon index of XIS1 was fitted independently of the photon indices of all other detectors, to check whether the calibration difference of the XIS observed by Tsujimoto et al. (2011) also affects this analysis. The photon indices of XIS1 and the other detectors are found to agree within confidence levels and the deviation is therefore not considered for further analysis. The parameter values of the best fit are given in Table 5.2.

The detector cross-normalization constants are very different in the two observations. This is most likely a result of the different extraction methods, i.e., the different coordinate systems and the missing attitude correction for Obs. I. During the extraction the ARF is calculated by the FTOOL `xissimarfgn` via ray-tracing simulations for the particular source position and extraction region

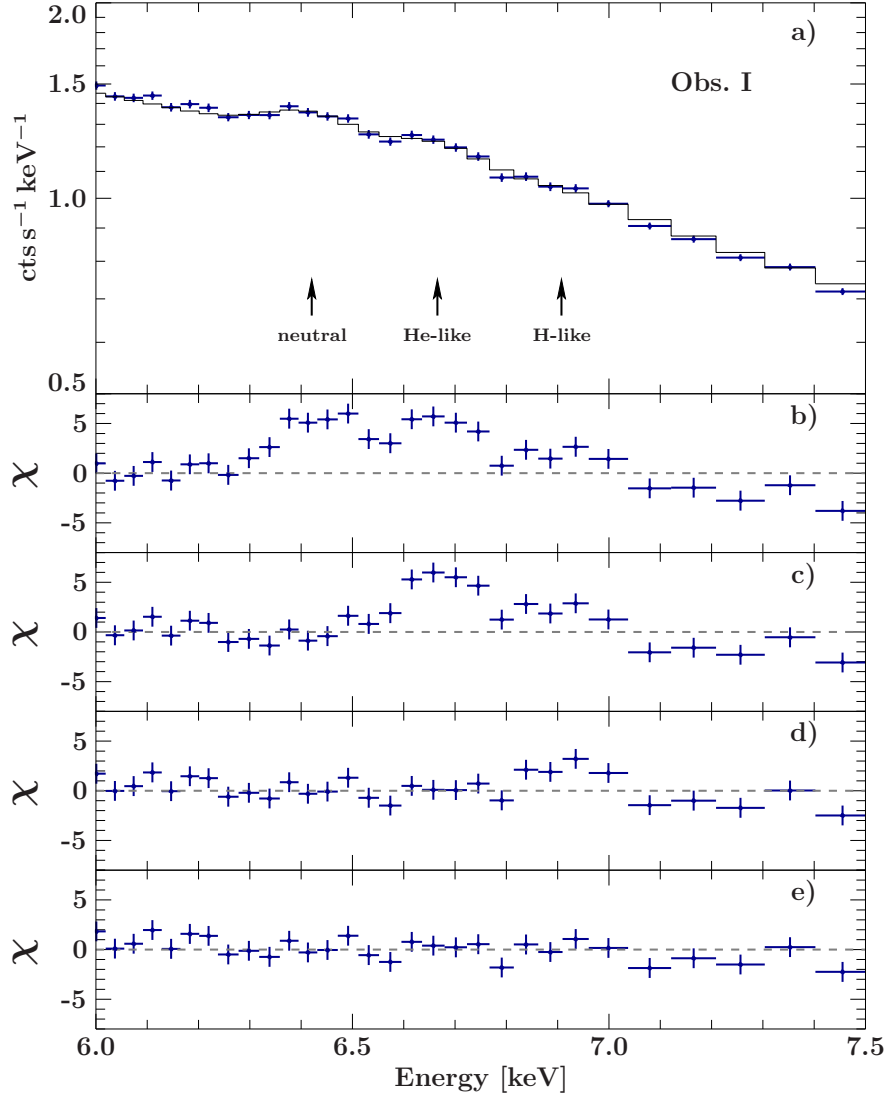


Fig. 5.7: Close-up of the iron line region for Obs. I for all XIS combined. Panel **a)** shows the spectrum and best fitting model including neutral, He-like, and H-like iron lines (black). Panel **b)** shows the residuals for the continuum model without any emission lines. Panel **c)** shows the residuals for the continuum model with only the neutral $K\alpha$ line and panel **d)** shows the residuals for the continuum model with both, neutral and He-like $K\alpha$ lines. Panel **e)** shows the residuals for the continuum model with emission lines from neutral, He-like, and H-like iron. All panels show the respective best fit.

size/shape (see [Ishisaki et al. 2007](#), for details). The ARF generation is very sensitive to the source position and extent, so a systematic uncertainty is introduced to the flux measurement when the position “wiggles” during the observation or gets shifted. The reason why PIN is chosen as the reference detector is because as a collimated instrument, small source position uncertainties have less impact on the measured flux.

Comparing Obs. I and II, the photon index decreases with flux, whereas the folding energies agree within confidence levels. The temperature of the black body increases about 0.1 keV from Obs. I to Obs. II.

The difference of the spectral shape of Obs. I and II is illustrated in [Fig. 5.9](#). It shows the unfolded spectra and the ratio of those, when rebinning them to the same energy grid. The two observations differ most in the XIS energy range, so below the cyclotron line. Below ~ 2.5 keV, there is an excess

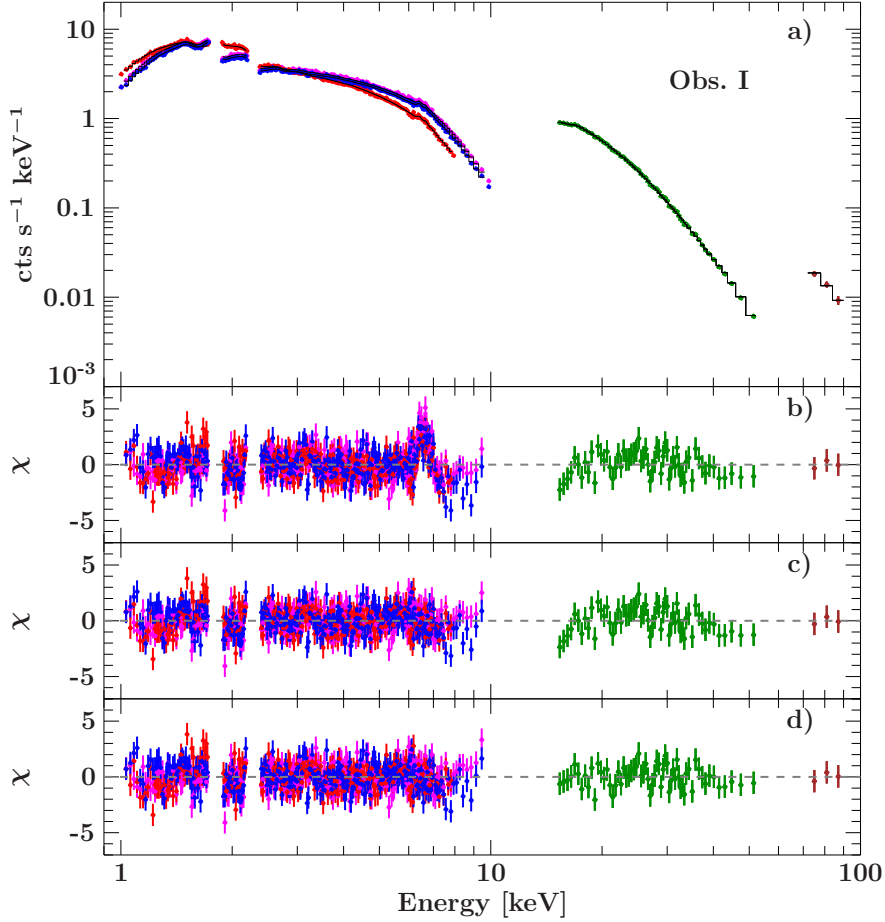


Fig. 5.8: Phase averaged spectrum of Obs. I with different model components included. Panel **a)** shows the spectrum XIS0 (blue), XIS1 (red), XIS3 (magenta), PIN (green) and GSO (brown) in count space with the best fit model (black). The corresponding residuals are shown in panel **d)**. Panel **b)** shows the residuals of the continuum model without any iron emission lines and without the cyclotron line. Panel **c)** shows the residuals of the continuum model with all three iron lines included, but without the cyclotron line. All panels show the respective best fit for each model. Adapted from [Ballhausen et al. \(2015\)](#).

of photons in Obs. I. Around the iron line, there is again some deviation, which is not surprising considering that different ionization states are detected in the two observations. At higher energies, the ratio stays rather constant with energy, which is represented by the similar photon indices and folding energies in both observations. At soft energies, the spectral shape is additionally determined by the black body component, which varies between the observations.

5.5 Phase resolved spectroscopy

Figure 5.6 does not only show that the pulse profiles change with energy but also that the spectra change with pulse phase, although the spectral information is lost in this kind of representation. This variation originates from the different viewing angles onto the neutron star and the accretion column. The variation of the spectral shape with pulse phase was studied in more detail by extracting spectra for five phase intervals (Pb 1–5). The number of phase intervals is again limited by the time resolution of XIS and also certain SNR has to be ensured, especially during the pulse profile minimum (see upper panels of Figs. 5.11 and 5.12 for the definition of the phase intervals). GSO was not used for phase resolved analysis because of its poor statistics.

Table 5.2: Best fit parameters and statistics for the phase-averaged spectra. The “dagged” values are taken from Fürst et al. (2014).

Parameter	Obs. I	Obs. II
N_{H} [10^{22} cm $^{-2}$]	0.796 ± 0.021	0.784 ± 0.027
$\mathcal{F}_{15-50\text{keV}}$ [10^{-9} erg s $^{-1}$ cm $^{-2}$]	3.70 ± 0.02	4.88 ± 0.3
$\Gamma_{\text{XIS0,3}}$	0.97 ± 0.04	0.89 ± 0.04
Γ_{XIS1}	1.00 ± 0.04	0.95 ± 0.04
\mathcal{F}_{BB} [10^{-9} erg s $^{-1}$ cm $^{-2}$]	0.306 ± 0.018	$0.479^{+0.029}_{-0.031}$
kT_{BB} [keV]	0.581 ± 0.010	0.673 ± 0.012
E_{fold} [keV]	23.3 ± 0.9	22.8 ± 0.9
$E_{\text{FeIK}\alpha}$ [keV]	$6.420^{+0.020}_{-0.017}$	$6.440^{+0.023}_{-0.017}$
$A_{\text{FeIK}\alpha}$ [10^{-4} phs s $^{-1}$ cm $^{-2}$]	6.3 ± 1.0	8.4 ± 1.5
$E_{\text{FeXXV K}\alpha}$ [keV]	6.666 ± 0.021	$6.729^{+0.029}_{-0.027}$
$A_{\text{FeXXV K}\alpha}$ [10^{-4} phs s $^{-1}$ cm $^{-2}$]	5.9 ± 1.0	$6.5^{+1.6}_{-1.5}$
$E_{\text{FeXXVI K}\alpha}$ [keV]	6.91 ± 0.05	–
$A_{\text{FeXXVI K}\alpha}$ [10^{-4} phs s $^{-1}$ cm $^{-2}$]	2.1 ± 1.0	–
E_{CRSF} [keV]	12.2^{\dagger}	12.2^{\dagger}
d_{CRSF}	$0.36^{+0.15}_{-0.14}$	0.48 ± 0.14
σ_{CRSF} [keV]	2.5^{\dagger}	2.5^{\dagger}
C_{XIS0}	$0.764^{+0.014}_{-0.013}$	$0.952^{+0.021}_{-0.020}$
C_{XIS1}	$0.738^{+0.019}_{-0.018}$	$0.893^{+0.027}_{-0.026}$
C_{XIS3}	0.743 ± 0.013	0.967 ± 0.021
C_{PIN}	1	1
C_{GSO}	0.80 ± 0.08	0.79 ± 0.06
χ_{red}^2 (d.o.f)	1.25 (712)	1.32 (561)

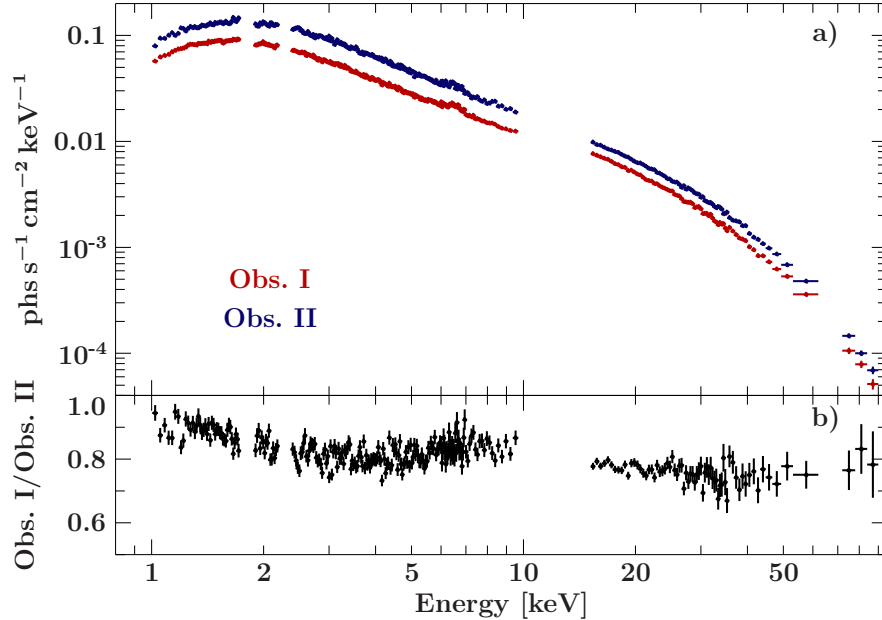


Fig. 5.9: Panel **a)** shows the unfolded spectra of Obs. I and Obs. II in comparison. For clarity, only XIS3, PIN and GSO is shown. Panel **b)** shows the ratio of the two spectra. The spectra of the individual instruments have been corrected for the cross-normalization constants obtained from spectral fitting. Taken from Ballhausen et al. (2015).

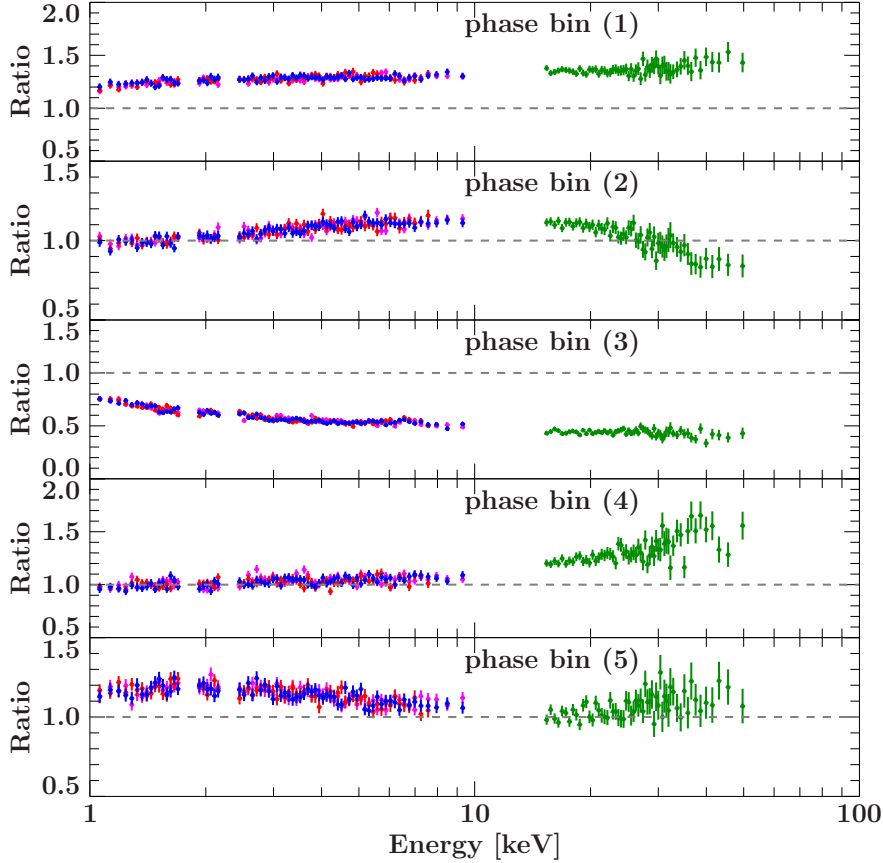


Fig. 5.10: Count rate ratios of the all phase resolved spectra with respect to the phase averaged spectrum of Obs. I.

The minimum SNR requirement for rebinning was reduced for the phase resolved spectra to account for shorter effective exposure due to the splitting of the observations. The SNR requirements for both observations are 50 for XIS (45 for the 6–7 keV iron band) for all phase intervals except for one covering the main minimum of the pulse profile, where the required minimum SNR is 40 (35 for 6–7 keV) and 15 for PIN.

Figure 5.10 shows the count rate ratios of all phase resolved spectra with respect to the phase averaged spectra. This allows to estimate how the spectra change in terms of hardness or localized features, without having to care about parameter correlations or characteristics of the applied model. The spectrum of Pb. 1 is very similar in shape to the phase averaged spectrum. As the phase averaged spectrum is the weighted mean of the phase resolved spectra, it is expected to resemble the spectrum of the main pulse. The spectrum of Pb. 2 is slightly harder than the phase averaged spectrum in the XIS energy range but the cutoff sets in at lower energies and the ratio drops around 20 keV. The spectrum that covers the pulse profile minimum (Pb. 3) is softer than the phase averaged spectrum with most of the soft excess below 2.5 keV. The spectrum of Pb. 4 is similar in shape to the phase averaged spectrum in the XIS range but gets harder in the PIN energy range. Phase bin 5 has again a soft excess around 3 keV, but tends to get harder again above ~ 25 keV, though at low statistics.

The applied model was the same as for the phase averaged spectrum, but without the H-like iron $K\alpha$ line, which cannot be constrained in phase averaged spectra. Figures 5.11 and 5.12 show the evolution of some parameters over pulse phase. The detector cross-normalization constants and the iron line energies were not allowed to vary over pulse phase.

As expected, the fluxes follow the pulse profiles. The black body temperature is rather similar in

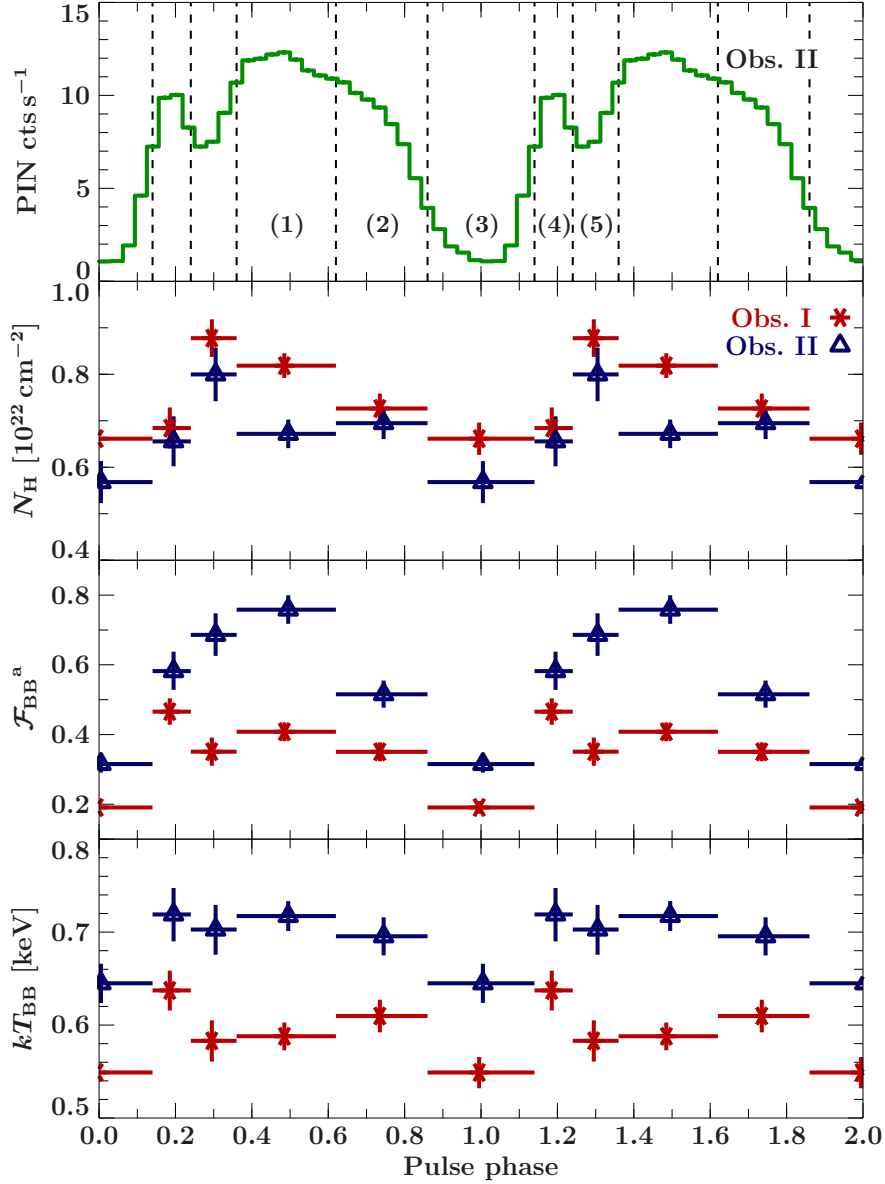


Fig. 5.11: Evolution of the column density, black body flux and temperature over pulse phase for Obs. I (red) and Obs. II (blue). The upper panel shows the PIN pulse profile of Obs. II. All fluxes are given in units of 10^{-9} erg s^{-1} cm^{-2} . Profiles and parameter evolution are shown twice for clarity. Adapted from Ballhausen et al. (2015).

most phase bins but has a lower value during the pulse profile minimum. The photon index and folding energy change significantly from phase to phase, reflecting the complex change of the spectral shape already observed in Fig. 5.10. The cyclotron line strength is highest during the pulse profile minimum and the secondary peak (Pbs. 3 and 4). The parameter evolution is similar in both observations.

The observed parameter variations might at least partly be caused by model-intrinsic artificial parameter correlations. To test their impact on this analysis, confidence contours were calculated for several pairs of fit parameters. These are shown in Figs. 5.13 and 5.14. They demonstrate that the observed variation of N_H is indeed significant although this parameter correlates with the black body temperature and Γ . Interestingly higher N_H values generally correspond to lower black body temperatures and fluxes, although, one would think that an increase of black body flux should be compensated for by higher absorption. However, the contour plots show that the powerlaw reacts more

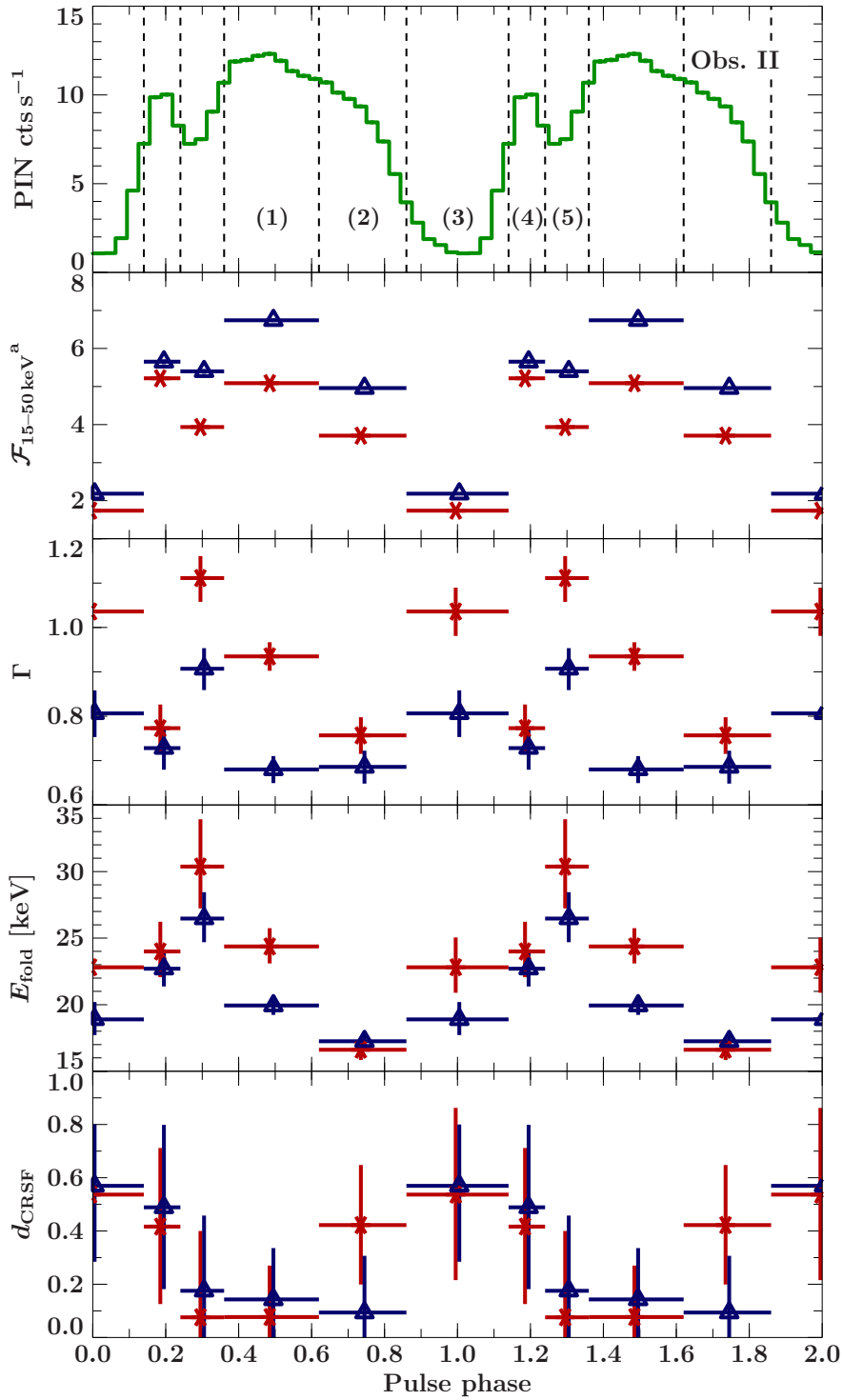


Fig. 5.12: Evolution of the powerlaw flux, photon index, folding energy and optical depth of the cyclotron line over pulse phase for Obs. I (red) and Obs. II (blue). The upper panel shows the PIN pulse profile of Obs. II. All fluxes are given in units of $10^{-9} \text{ erg s}^{-1} \text{ cm}^{-2}$. Profiles and parameter evolution are shown twice for clarity. Adapted from [Ballhausen et al. \(2015\)](#).

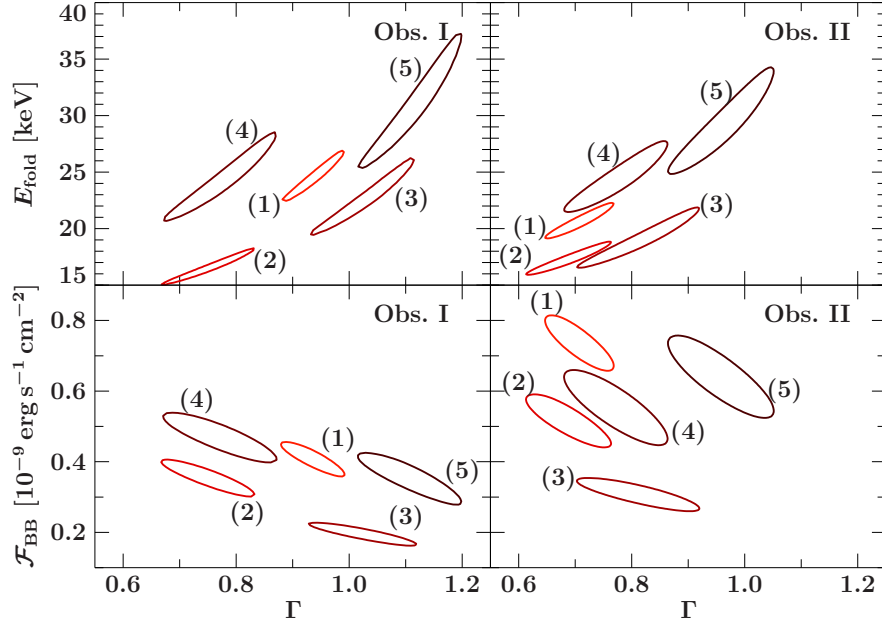


Fig. 5.13: 3σ contours of all phase resolved spectra for both observations of Γ vs black body flux and folding energy. Adapted from Ballhausen et al. (2015).

sensitively to a change of N_{H} . The folding energy and Γ both peak during the secondary peak and have their lowest value during the decline of the main peak. These parameters are intrinsically correlated, but the contour plots show that the change is still significant.

5.6 Discussion

The *Suzaku* observations of KS 1947+300 confirm the peculiar morphology and energy dependence of the pulse profiles seen in previous outbursts. At low energies, the pulse profile consists of one broad peak. Around 6 keV a second, narrow peak starts to form right after the main minimum and grows towards higher energies. However, this behavior is rarely seen in X-ray pulsars. Most cases show complex profiles at low energies that evolve to rather smooth and sinusoidal profiles at higher energies, e.g., in Vela X-1 (Kreykenbohm et al. 2002), 4U 1909+07 (Fürst et al. 2011) and EXO 2030+375 (Naik et al. 2013). However, IGR J16393–4643 shows pulse profiles similar to KS 1947+300 (Islam et al. 2015). The exact shape of pulse profiles is generally very difficult to interpret, because the geometry of the system, relativistic light bending effects, the radiation pattern of the column, absorption and scattering all contribute to the formation of the pulse profiles. One possible explanation for the secondary narrow peak is that for very similar inclinations of magnetic field and observer, during a small phase interval, the opposite column is light-bent towards the observer. For a certain energy-dependent radiation pattern, the peak can appear at higher energies only (Falkner, priv. comm.).

The phase averaged spectra show the presence of different ionization states of iron, which is the first time that also He-like and H-like iron is detected in this source. Other observations have found iron emission lines also at higher energies (e.g., Fürst et al. 2014, at ~ 6.5 keV), which already indicates ionization of iron, but these could not be resolved with *RXTE* or even *NuSTAR*. Emission lines from neutral, He-like and H-like iron have been observed in other sources before, e.g., Cen X-3 (Naik, Paul & Ali 2011).

The cyclotron line discovered by Fürst et al. (2014) was included in the model although the centroid energy is in the gap between XIS and PIN. The inclusion indeed improves the fit quality but it should

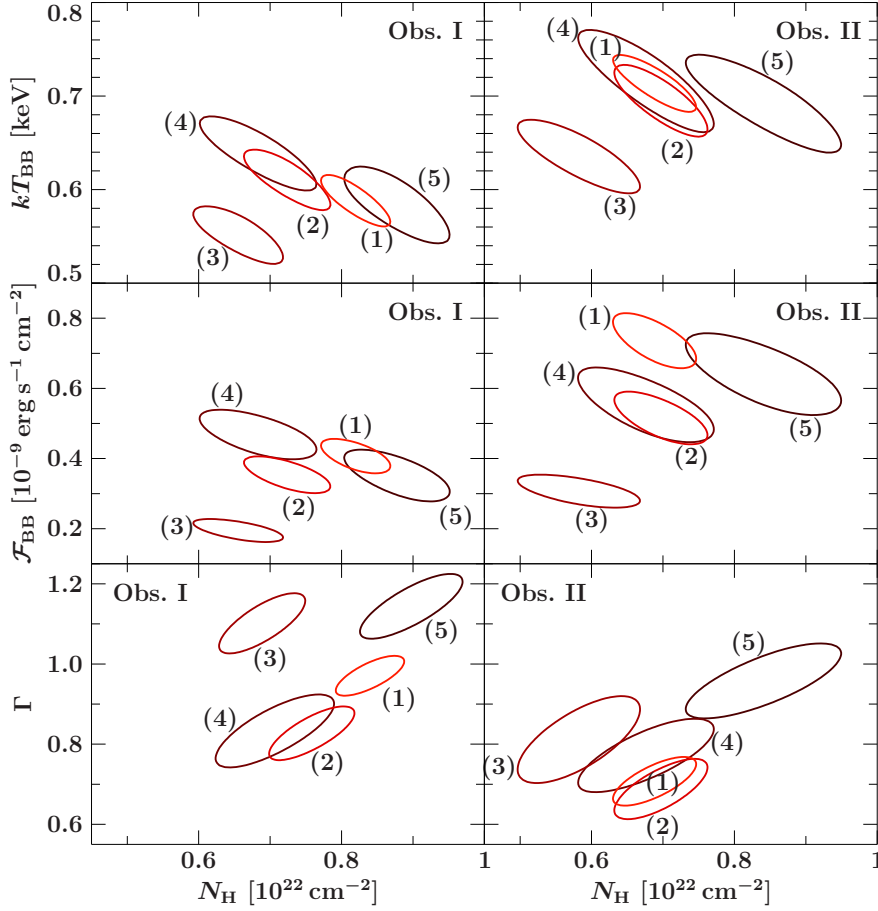


Fig. 5.14: 3σ contours of all phase resolved spectra for both observations of N_{H} vs black body temperature, balckbody flux and Γ . Adapted from [Ballhausen et al. \(2015\)](#).

be noted that a reliable detection of the line wings is made impossible by calibration uncertainties of the detector responses very close to their energy edge.

The pulse resolved spectra show a strong variations of the spectral shape over pulse phase, although these are affected by model-intrinsic parameter correlations. Contour calculations confirmed, however, a change of N_{H} over pulse phase although in combination with changes of the continuum. The change of N_{H} is very interesting because a neutral absorber should not couple to the magnetic field of the pulsar and therefore no dependence of the absorption column density on the pulse phase should be observed. If the medium is strongly ionized, it is more easily trapped by the magnetic field, but should be quite transparent for incident X-rays. The conclusion has to be that moderately ionized matter, that still contributes to the absorption mostly via K-shell absorption exists close enough to the neutron star to couple to its magnetic field.

Previous observations by *BeppoSAX* have found no variability of N_{H} over pulse phase although the instruments covered an energy range down to 0.1 keV. [Naik et al. \(2006\)](#) found the `compTT` model to describe the *BeppoSAX*. The `compTT` model generally produced worse fits of the *Suzaku* data. Contour plots of N_{H} using the `compTT` model still showed a variation of N_{H} with the minimum appearing during Pb. 3, although individual values are moderately different. There is no doubt that the underlying continuum model has an impact on the observed N_{H} . This was also reported by [Hemphill et al. \(2014\)](#), who observed model-dependent N_{H} variability in 4U 1538–522.

Therefore, the next step has to be to replace the empirical continuum models by physically motivated, self-consistent models such as Becker&Wolff model to unambiguously connect model parameters with

source properties and to disentangle artificial parameter correlations. First attempts to fit the spectra of KS 1947+300 with the `compmag` model have not been successful, probably because cyclotron emission and bremsstrahlung in the seed photon term cannot be neglected (see Sec. 3.3.2).

Finally, because of the characteristic shape and energy dependence of the pulse profiles, which hint at a certain geometry regarding magnetic field and observer, KS 1947+300 might be a suitable candidate to try to also model the pulse profiles. The reason why KS 1947+300 is a very promising candidate for this kind of study is because the inclination parameters are generally very difficult to determine from fitting the pulse profiles, so additional constraints on these two parameters will reduce runtime significantly and avoid at least some of the parameter degeneracies.

6 *NuSTAR* observations of A 0535+26 at low luminosities

6.1 The history of A 0535+26

A 0535+26 was discovered in 1975 by the Rotation Modulation Collimator on *Ariel V* during routine observations of the Crab as a transient X-ray source exhibiting 104 s pulsations (Rosenberg et al. 1975). The optical counterpart was identified to be HDE 245770 (Li et al. 1979), a B0IIIe star¹ with an estimated distance of ~ 2 kpc (Steele et al. 1998).

The orbital parameters are reported to be $e = 0.42 \pm 0.02$ and $P_{\text{orb}} = 110.3 \pm 0.3$ d (Finger, Wilson & Harmon 1996). A 0535+26 shows irregular outburst activity with normal Type I outbursts corresponding to periastron passage and giant Type II outbursts, interrupted by periods of quiescence (see, e.g., Rothschild et al. 2013). Figure 6.1 shows the daily *Swift*/BAT lightcurve of A 0535+26. The different luminosity states and the periods of quiescence are clearly visible.

A 0535+26 is a known cyclotron line source with a fundamental line at ~ 50 keV and a second harmonic at ~ 100 keV (Kendziorra et al. 1994; Kretschmar 1991; Kretschmar et al. 1996). The fundamental line energy shows no significant variation over two orders of magnitude in luminosity (Caballero et al. 2007, 2013). Because of its relatively small distance, A 0535+26 is a suitable candidate for observations at very low luminosities and the cyclotron line measurement at lowest observed luminosity of $\sim 3.7 \times 10^{34}$ erg s⁻¹ was still in agreement with a constant cyclotron line energy (Terada et al. 2006).

The X-ray continuum of A 0535+26 is often empirically modelled by a cut-off powerlaw with an additional black body of 1–2 keV temperature but the spectral shape varies with luminosity. Postnov et al.

¹ HDE 245770 was first classified as a O9.7IIIe star by Giangrande et al. (1980). Steele et al. (1998) later used high-quality CCD spectra and argued that a classification as B0IIIe is the most appropriate classification, although the previously accepted O9.7IIIe cannot be discarded.

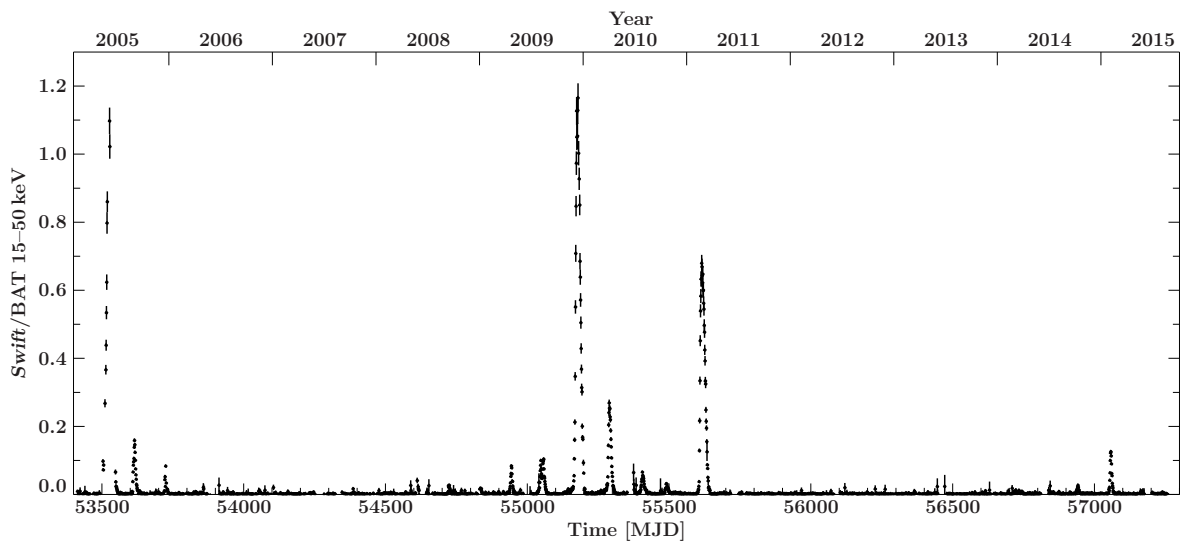


Fig. 6.1: *Swift*/BAT daily lightcurve of A 0535+26

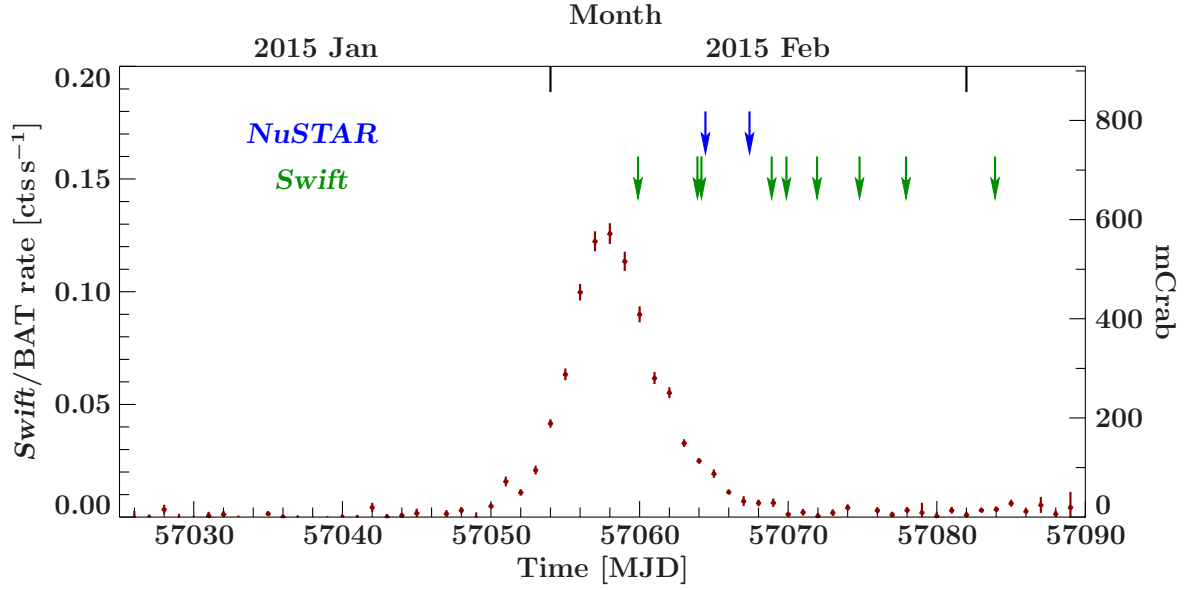


Fig. 6.2: *Swift*/BAT daily lightcurve of A 0535+26 of the 2015 January/February outburst. The arrows mark the *NuSTAR* observations (blue) and *Swift*/XRT pointed observations (green).

(2015) studied the dependence of the spectral hardness on luminosity of (among others) A 0535+26 and found the spectral hardness to be rather constant above 10^{37} erg s $^{-1}$ but decreasing towards lower luminosities. This is interpreted as the formation of the accretion column around the luminosity where the hardness ratio saturates.

Not only the X-ray pulsar but also the optical companion of the A 0535+26/HDE 245770 system was and is subject of intensive monitoring and the correlation of X-ray activity and H α emission of the Be disk is analyzed by, e.g., [Camero-Arranz et al. \(2012\)](#).

6.2 Data Acquisition and Reduction

NuSTAR first observed A 0535+26 twice in 2015 February near the end of its 2015 January/February outburst. Nine pointed *Swift*/XRT observations of ~ 1 – 2 ks exposure were taken to follow the decline phase of this outburst. A close-up of the *Swift*/BAT lightcurve with the times of *NuSTAR* and *Swift*/XRT observations marked is shown in Fig. 6.2.

6.2.1 *NuSTAR*

The data were reprocessed using *nupipeline* as part of the *NUSTARDAS* v. 1.5.1 and *CALDB* v. 20150316. The source region is a circle of $90''$ radius and the background region consists of 3 circles of $120''$ radius from the remaining corners of the chip to ensure sufficient SNR of the background, especially around the cyclotron line energy. All time information were transferred to the solar barycenter and corrected for binary motion using the ephemeris from [Finger, Wilson & Harmon \(1996\)](#). The observation log is summarized in Table 6.1.

6.2.2 *Swift*

All *Swift* observations were taken in Window Timing Mode and reprocessed with the *FTOOL* *xrtpipeline* distributed with *HEASoft* v. 6.16 to apply standard calibration and screening. The extraction regions are boxes of 40 pixels length. None of them is affected by considerable pile-up.

Table 6.1: Observation log for the two *Suzaku* and the *NuSTAR* observation.

ObsID	mid-time [MJD]	exposure [ks]
<i>NuSTAR</i>		
80001016002	57064.43	21.4
80001016004	57067.40	29.7
<i>Swift</i>		
00035066050	57059.91	1.09
00035066051	57063.90	0.95
00081432001	57064.21	1.94
00035066052	57068.90	1.08
00035066053	57069.89	1.06
00035066054	57071.95	1.07
00035066055	57074.88	0.33
00035066056	57077.94	0.96
00035066057	57083.96	1.55

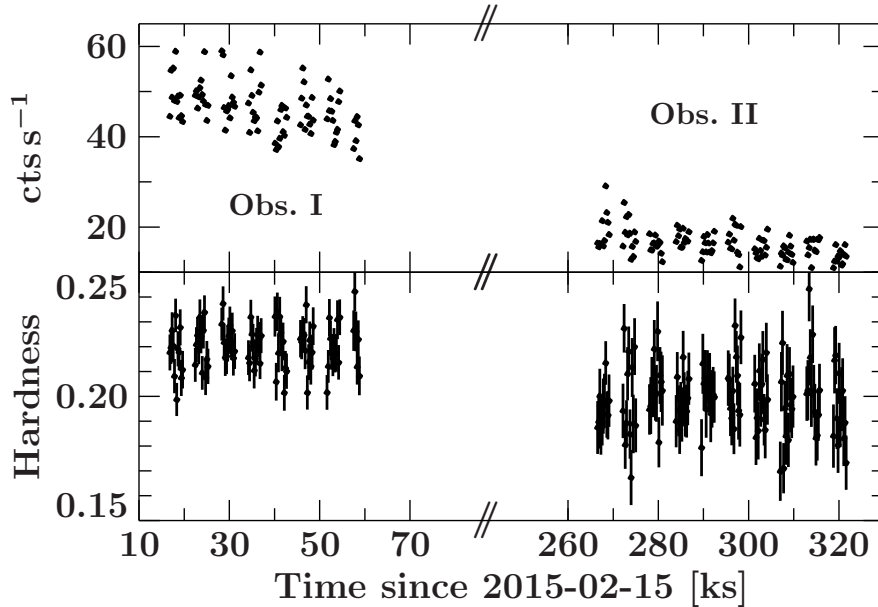


Fig. 6.3: Background-subtracted lightcurve and hardness ratio with 256 s time bins of both *NuSTAR* observations of A 0535+26. The hardness ratio is defined as the count rate ratio of the 3–10 keV band to 15–50 keV band.

6.3 Timing Analysis

Lightcurves with 256 s time resolution were extracted for the full 3–78 keV range and are shown, together with the hardness ratio, which is defined as the count rate ratio the sub-bands 3–10 keV and 15–50 keV, in Fig. 6.3.

The count rate decreases between the observations, as expected for the decline phase of the outbursts, although the count rates are not corrected for variations of the effective area, which can result, e.g., from different source positions on the chip. The decline trend can even be observed during the individual observations.

The hardness ratios are different in the two observations but stay rather constant during the observation. Unlike in the *Suzaku* observations of KS 1947+300, there seems to be a fundamental change in spectral shape above 3 keV between the observations. This is investigated in more detail in Sec. 6.4.

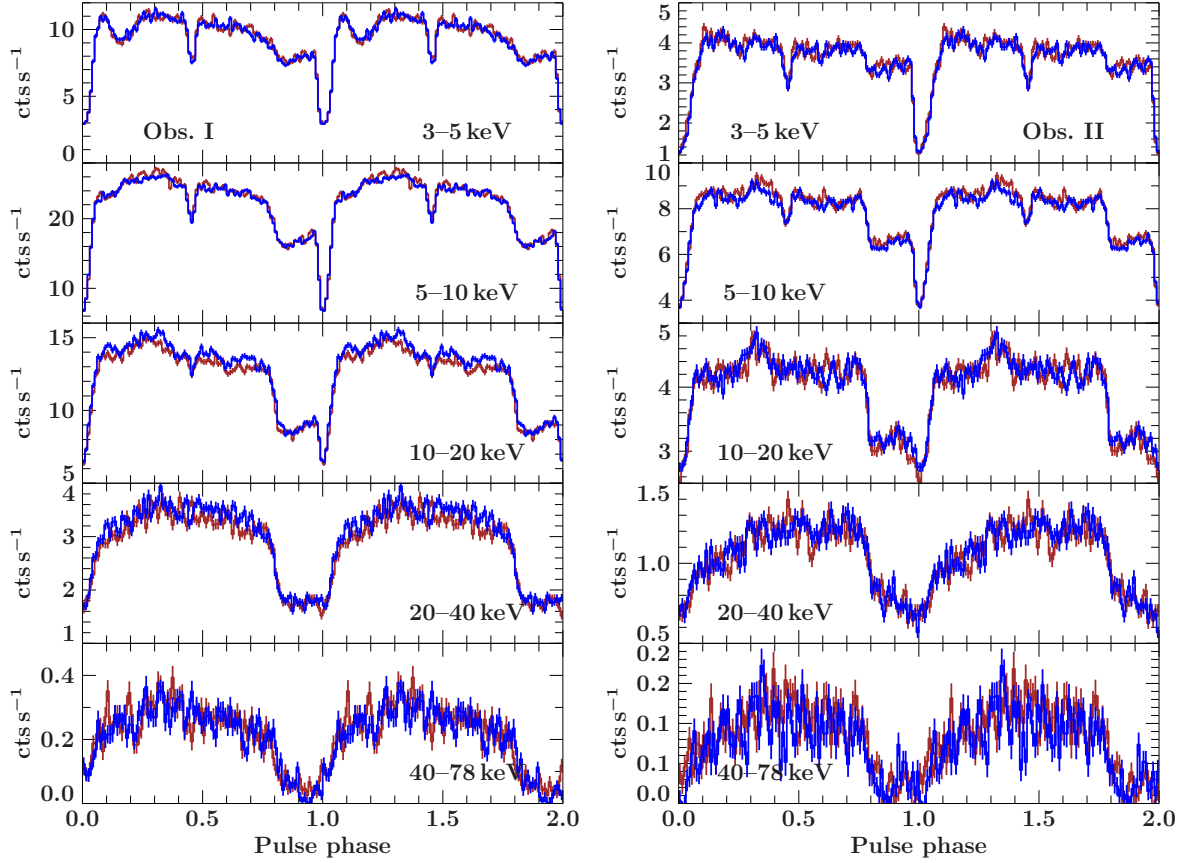


Fig. 6.4: Energy resolved pulse profiles of FMPA (blue) and FPMB (red) of both *NuSTAR* observations. All profiles are background-subtracted and shown twice for clarity.

Pulse periods were again determined using the epoch folding method (see Sect. 5.3 for details). The binary corrected pulse periods are 103.3913(8) s in Obs. I and 103.3890(9) s in Obs. II.

Pulse profiles for different energy bands are shown in Fig. 6.4. Below ~ 20 keV, the pulse profile has a rather plateau-like shape, modified by a complex sub-structure with two narrow minima of different depth. At higher energies, the pulse profile becomes more and more sinusoidal in shape. The smaller minimum vanishes and the main minimum gets more pronounced, rather by a drop of the maximum than the minimum is actually widened.

The energy resolved pulse profiles of the two observations are quite similar, but the softest profile of Obs. I shows a small dip around phase 0.2 (as defined in Fig. 6.4) that is not observed in the lower luminosity observation. A very similar energy dependence and evolution with luminosity was observed by Caballero et al. (2013).

6.4 Spectral Analysis

For spectral analysis, the energy range of 5–79 keV for *NuSTAR* and 1–10 keV for *Swift* was considered. The *NuSTAR* data in the 3–5 keV range had to be excluded due to a mismatch between *Swift* and *NuSTAR* (see Fig. 6.5). This mismatch is a known issue and will probably be resolved in a calibration update in the near future.

The *NuSTAR* spectra were rebinned to a minimum SNR of 25, 35, 25, 15, 10, 5 for the 5–10 keV, 10–20 keV, 20–30 keV, 30–50 keV, 50–70 keV and 70–80 keV, respectively. The *Swift* observations that were fitted simultaneously to the *NuSTAR* observations are ObsID 00081432001 for Obs. I and

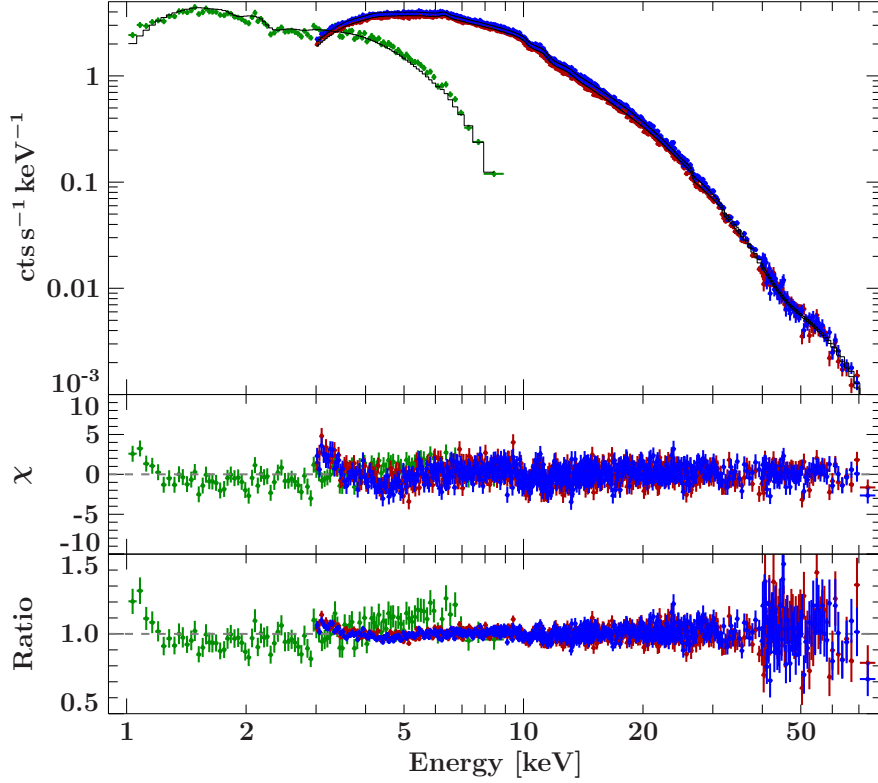


Fig. 6.5: Joint fit of Obs. I of *NuSTAR* and *Swift* with a *NuSTAR* noticed energy range of 3–79 keV with a simple absorbed powerlaw model to illustrate the calibration mismatch between 3–5 keV. The upper panel shows count spectra of *Swift* (green) and *NuSTAR*/FPMA (blue) and FPMB (red). The middle and lower panels show the residuals and the data/model ratio, respectively. Strange residuals in *NuSTAR* are clearly visible below 5 keV. The ratio panel shows that the *Swift* spectrum is not described properly by the model, because the fit is dominated by *NuSTAR* because of its much better SNR.

00035066052 for Obs. II. The two *Swift* spectra corresponding to the *NuSTAR* observations were rebinned to a minimum SNR of 15 and 5, respectively.

6.4.1 Empirical models

The empirical models applied to the data are an absorbed cutoff powerlaw (`cutoffpl`) and a powerlaw with a high-energy cutoff factor (`powerlaw × highecut`), both with a black body of ~ 1.4 keV temperature, modified by a Gaussian emission line to model the iron $K\alpha$ line and a Gaussian absorption line to model the cyclotron line. The width of the iron line component was fixed to 10^{-6} keV, assuming that line broadening is only due to the detector response.

It turned out that Obs. I is well described by the `cutoffpl`-model, which fails, however, for Obs. II. Figure 6.6 shows the unfolded spectra and residuals for both models and both observations. The `powerlaw × highecut` model is also able to describe the spectra of Obs. I well, because the cutoff energy can be set to a very low value and the model effectively becomes a `cutoffpl`.

The two observations are clearly different around ~ 30 keV, in particular, the spectrum of Obs. II shows a “kink” around this energy which cannot be modelled by the `cutoffpl` model alone, because despite exponential damping, the turn-over is too smooth. What is a well known problem of the `powerlaw × highecut` model, namely the sudden onset of the exponential folding at the cutoff energy is exactly what is required to model the kink.

The best fit parameter for these two models are given in Tables 6.2 and 6.3. The luminosities,

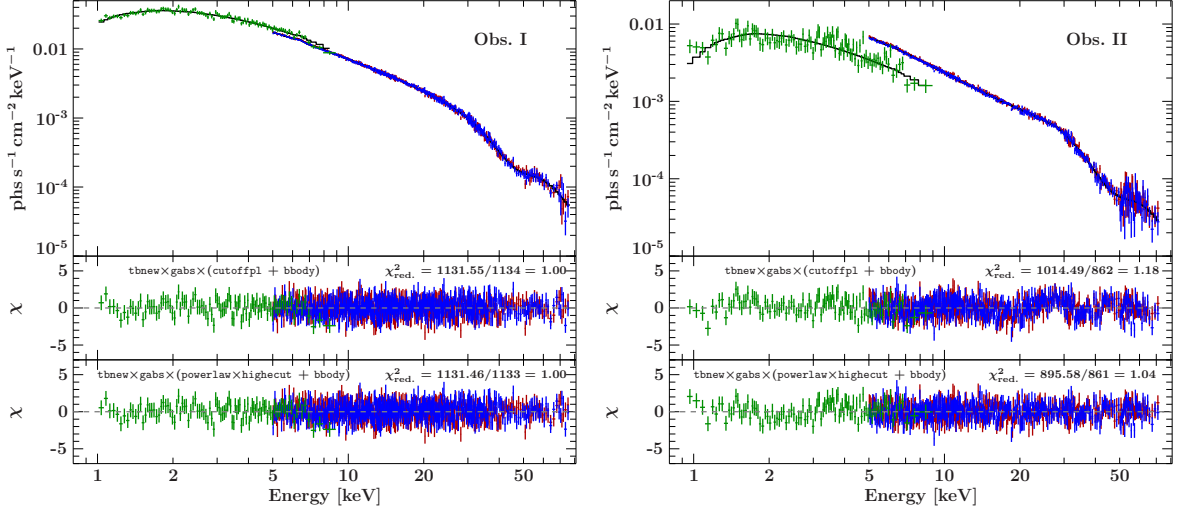


Fig. 6.6: Phase averaged spectra of obs. I (left) and Obs. II (right) with different continuum models. The upper panels show the unfolded spectra of *Swift* (green) and *NuSTAR*/FPMA (blue) and FPMB (red). The middle and lower panels show the residuals for the `cutoffpl` and `powerlaw x highcut` model, respectively.

Table 6.2: Best fit parameters for the `cutoffpl` model for both observations.

Parameter	Obs. I	Obs. II
N_{H} [10^{22} cm $^{-2}$]	0.79 ± 0.0	$0.39^{+0.15}_{-0.14}$
Γ	$0.72^{+0.04}_{-0.05}$	0.58 ± 0.10
E_{fold} [keV]	19.4 ± 0.9	$21.4^{+2.3}_{-1.9}$
$\mathcal{F}^{3-50 \text{ keV}}$ [10^{-9} erg/s/cm 2]	2.974 ± 0.030	1.027 ± 0.020
kT [keV]	1.41 ± 0.05	$1.526^{+0.026}_{-0.027}$
E_{cycl} [keV]	$45.6^{+0.7}_{-0.6}$	$47.1^{+0.9}_{-0.8}$
d_{cycl}	$12.7^{+1.7}_{-1.4}$	$15.0^{+2.4}_{-2.0}$
σ_{cycl} [keV]	8.1 ± 0.6	$7.5^{+0.7}_{-0.6}$
E_{Fe} [keV]	$6.424^{+0.018}_{-0.064}$	$6.28^{+0.28}_{-0.13}$
EW_{Fe} [eV]	21 ± 5	8 ± 6
C_{FPMA}	1*	1*
C_{FPMB}	1.009 ± 0.004	1.023 ± 0.005
C_{XRT}	1.154 ± 0.019	0.590 ± 0.025

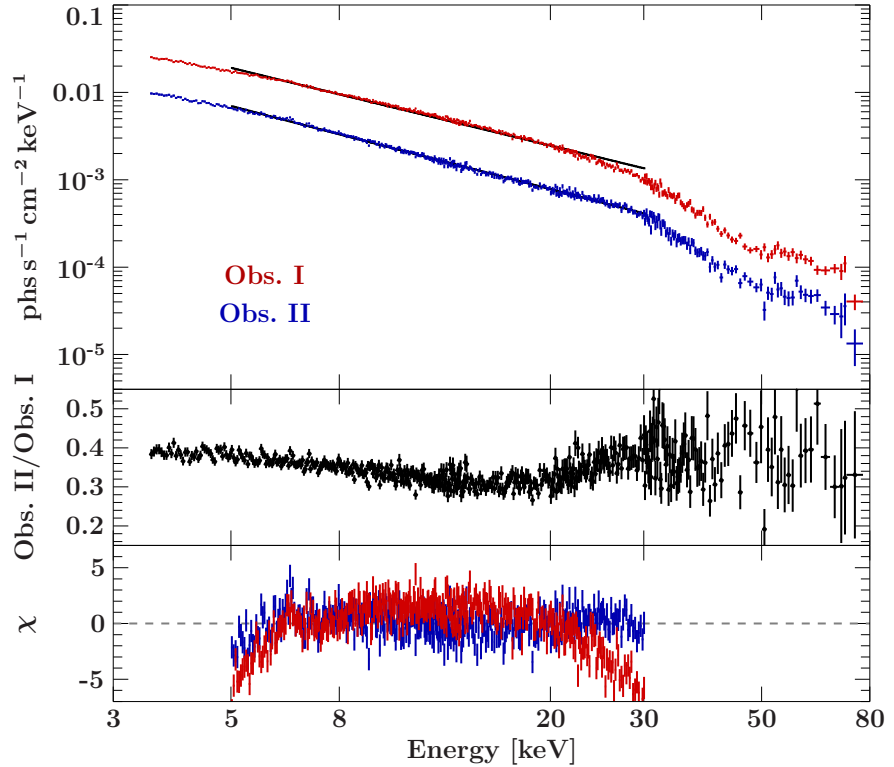
calculated from the 3–50 keV flux and assuming a distance of 2 kpc are $(1.42 \pm 0.02) \times 10^{36}$ erg s $^{-1}$ and $(5.02 \pm 0.09) \times 10^{35}$ erg s $^{-1}$ for Obs. I and II, respectively. The extremely low value of the cutoff energy of the `highcut` model in Obs. I shows that this model is effectively also a `cutoffpl`.

Figure 6.7 shows the unfolded *NuSTAR* spectra of Obs. I and II, as well as the count rate ratio of the two spectra. Below ~ 20 keV, Obs. II is slightly softer than Obs. I, but then gets harder again at higher energies up to ~ 40 keV. At even higher energies, the ratio is hard to track because of the rather low statistics, especially of Obs. II. The spectral difference of the two observations corresponds to the fact, that the spectrum of Obs. I is already modified considerably by the exponential folding (the folding energy is ~ 20 keV in the `cutoffpl` model), whereas the cutoff energy in the `highcut` model is at ~ 30 keV and the spectrum of Obs. II is very well described by a simple powerlaw (except for the very soft part where the black body and absorption play a significant role). This is illustrated in the lower panel of Fig. 6.7, which shows the residuals for a fit of a pure powerlaw to the 5–20 keV range of the spectra. Apart from line like residuals in the iron line regions, Obs. II is well fitted by the powerlaw in the chosen energy range. The residuals of Obs. II are strongly “bent”, showing that the

Table 6.3: Best fit parameters for the powerlaw \times highecut model for both observations.

Parameter	Obs. I	Obs. II
N_{H} [10^{22} cm $^{-2}$]	$0.75^{+0.10}_{-0.08}$	$1.40^{+0.16}_{-0.15}$
Γ	$0.72^{+0.04}_{-0.05}$	1.38 ± 0.04
E_{cut} [keV]	$2.1^{+0.6}_{-2.2}$	$28.1^{+1.3}_{-0.8}$
E_{fold} [keV]	19.4 ± 0.9	$27.7^{+2.5}_{-2.3}$
$\mathcal{F}^{3-50\text{keV}}$ [10^{-9} erg/s/cm 2]	$2.970^{+0.030}_{-0.031}$	1.049 ± 0.019
kT [keV]	1.42 ± 0.05	$1.526^{+0.026}_{-0.027}$
E_{cycl} [keV]	$45.6^{+0.7}_{-0.6}$	46.0 ± 1.0
d_{cycl}	$12.7^{+1.7}_{-1.3}$	$12.5^{+2.9}_{-2.3}$
σ_{cycl} [keV]	8.1 ± 0.6	$8.0^{+1.0}_{-0.9}$
E_{Fe} [keV]	$6.39^{+0.09}_{-0.04}$	$6.37^{+0.16}_{-0.09}$
EW_{Fe} [eV]	21 ± 5	13 ± 6
c_{FPMA}	1^*	1^*
c_{FPMB}	1.009 ± 0.004	1.023 ± 0.005
c_{XRT}	$1.153^{+0.015}_{-0.004}$	0.523 ± 0.024

Fig. 6.7: The top panel shows the unfolded spectrum of Obs. I (red) and Obs. II (blue). The middle panel shows the count rate ratio of the two observations and the lower panel shows the residuals for the 5–30 keV spectra when fitted with a simple powerlaw. For clarity, only FPMA is shown.



spectral shape is clearly different in the two observations.

The cyclotron line parameters are similar in both observations. A 0535+26 is one of the sources where no correlation of the cyclotron line energy with luminosity is observed (Caballero et al. 2013). To compare the very low luminosity observations of A 0535+26 with *NuSTAR* to previous observations, the cyclotron line energies observed with *NuSTAR*, together with those measured by Caballero et al. (2007) and Terada et al. (2006) are shown in Fig. 6.8.

The *NuSTAR* measurements are in very good agreement with a constant cyclotron line energy over luminosity at the lower luminosity end of feasible measurements. The only measurement of the cyclotron line at an even lower luminosity was performed by *Suzaku* and the cyclotron line is not as

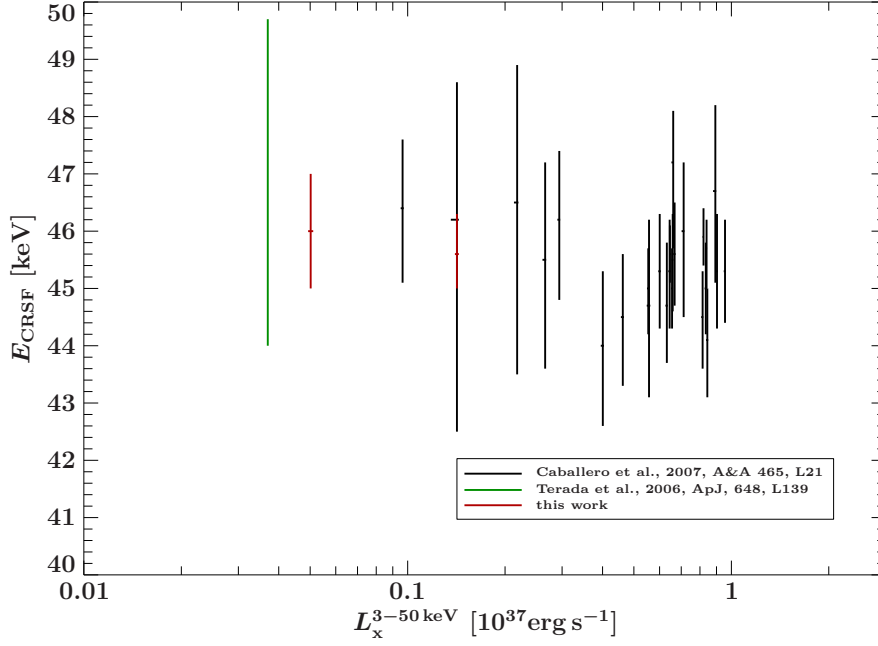


Fig. 6.8: E_{cycl} vs $\mathcal{F}^{3-50\text{keV}}$ as measured with *NuSTAR* and in comparison with values of previous observations. The *NuSTAR* results are in agreement with a constant E_{cycl} .

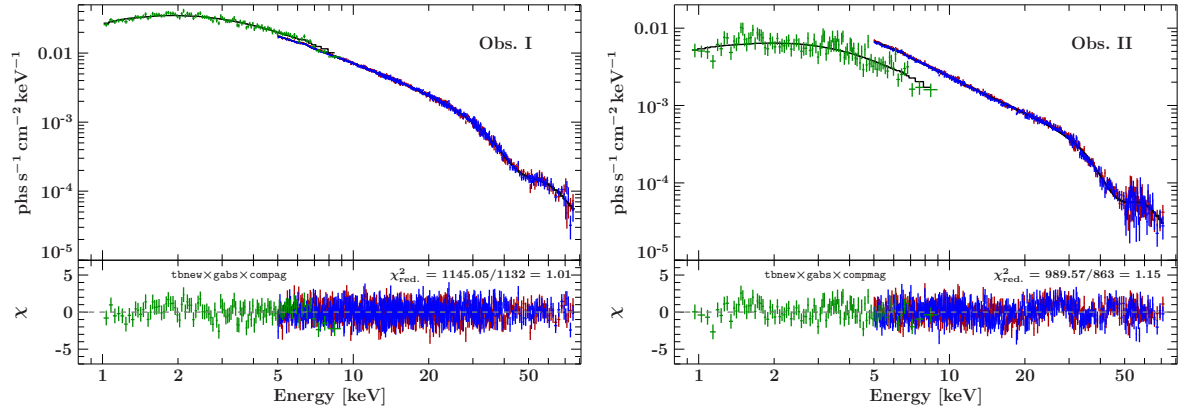


Fig. 6.9: Phase averaged spectra of obs. I (left) and Obs. II (right) fitted with the *compmag* model. The upper panels show the unfolded spectra of *Swift* (green), *NuSTAR*/FPMA (blue) and FPMB (red) and the model (black). The lower panels show the residuals. The model clearly fails for the fainter observation.

well constrained.

6.4.2 The *compmag* model

The physical models tested on the data are the *compmag* model and Mike Wolff’s implementation of the *Becker & Wolff (2007)* model. Hereafter, the applied models are also just referred to as “*compmag*” model or “*Bwcbcb*” but the full fit model is the absorbed continuum model, modified by a narrow, Gaussian iron emission line and a Gaussian cyclotron line component. Detector cross-normalization constants are introduced with respect to FPMA. The *compmag* model has some runtime problems, in particular, the model evaluation sometimes terminates unexpectedly with a memory allocation error. This makes fitting the model and especially the uncertainty determination very difficult.

The *compmag* model describes the phase-averaged spectrum of the first but not the second observation well (see Fig. 6.9) if the beta flag parameter is set to 2, i.e. for a velocity profile that is linear in τ . There are strong residuals at the “kink” energy. The best fit parameters are given in Table 6.4.

As the *compmag* model alone cannot provide a satisfactory description of the second observation, its

Table 6.4: Best fit parameters for the compmag model for both observations.

Parameter	Obs. I	Obs. II
N_{H} [10^{22} cm $^{-2}$]	$0.29^{+0.11}_{-0.06}$	$0.116^{+0.105}_{-0.006}$
$kT_{\text{BB}}^{\text{seed}}$ [keV]	$1.031^{+0.030}_{-0.043}$	1.107 ± 0.024
kT_{e} [keV]	$4.78^{+0.17}_{-0.53}$	> 9.90
τ	$0.728^{+0.036}_{-0.008}$	0.509 ± 0.004
r_0 [r_{S}]	$0.45^{+0.04}_{-0.07}$	> 9.9999999979
$\mathcal{F}^{3-50\text{keV}}$ [10^{-9} erg/s/cm 2]	$2.964^{+0.012}_{-0.009}$	$1.030^{+0.005}_{-0.004}$
E_{cycl} [keV]	$45.5^{+0.7}_{-0.6}$	$46.4^{+0.7}_{-0.4}$
d_{cycl}	$12.4^{+1.6}_{-1.0}$	$14.0^{+0.4}_{-0.5}$
σ_{cycl} [keV]	$8.05^{+0.43}_{-0.23}$	$7.1^{+0.5}_{-0.4}$
E_{Fe} [keV]	6.4^*	6.4^*
EW_{Fe} [eV]	23^{+5}_{-4}	15 ± 6
c_{FPMA}	1^*	1^*
c_{FPMB}	1.009 ± 0.004	$1.023^{+0.005}_{-0.004}$
c_{XRT}	$1.148^{+0.016}_{-0.020}$	0.564 ± 0.023
χ_{red}^2 (d.o.f)	$1.01(1135)$	$1.15(863)$

interpretability and comparability to the first observation is somewhat questionable. The polar cap radius and the electron temperature cannot be well constrained for the second observation and hit the upper limits of parameter range. Because of the difficulties in applying the model, however, it should be cautioned that this fit might not be a unique solution or another comparably well fit could be found in a parameter range where the model is not running stable enough.

6.4.3 The BWcbb model

The BWcbb model has the problem of a self-consistent flux normalization. The norm parameter is required for implementations in standard fitting packages like ISIS and XSPEC but the output flux is also determined by the mass accretion rate parameter \dot{M} . The norm parameter should therefore always be fixed to 1. The mass accretion rate could in principle be fitted, just like the norm of any other model, however, there are artificial parameter correlations and the model does not necessarily conserve energy. Fits with initial parameters including a free mass accretion rate can result in unphysical results. If the distance to the system is known, the mass accretion rate can at least roughly be estimated from the observed flux using Eq. 2.1. The practicable application has, however, a subtle caveat. Standard convolution models like `enflux` in ISIS or `cflux` in XSPEC can determine the flux correctly which could in principle be fed back into the mass accretion rate but the other parameters can also affect the output flux. As energy is not conserved in the model and the flux determination internally rescales the model, these parameters can not be constrained independently. A work-around for this problem is to determine the broad-band flux *externally*, e.g., by fitting *any model* that describes the data well and where all normalizations can be fixed, independent of the actual interpretation of the model and calculate the expected mass accretion rate for the BWcbb model.

When fitting the BWcbb model, the norm parameter should be fixed to 1 and the mass accretion rate to the previously determined value. If an acceptable fit is found, the mass accretion rate can be thawed again for a fine adjustment of all parameters.

Figure 6.10 shows the best fit of the BWcbb model Obs. I of A 0535+26. There is an excess of soft photons below ~ 1.3 keV, but the hard tail of the spectrum is well described. The magnetic field was tied to the cyclotron line energy, corrected for a gravitational redshift of $z = 0.3$ during the fit.

The best fit parameters are given in Table 6.5. Uncertainties could not yet be determined because

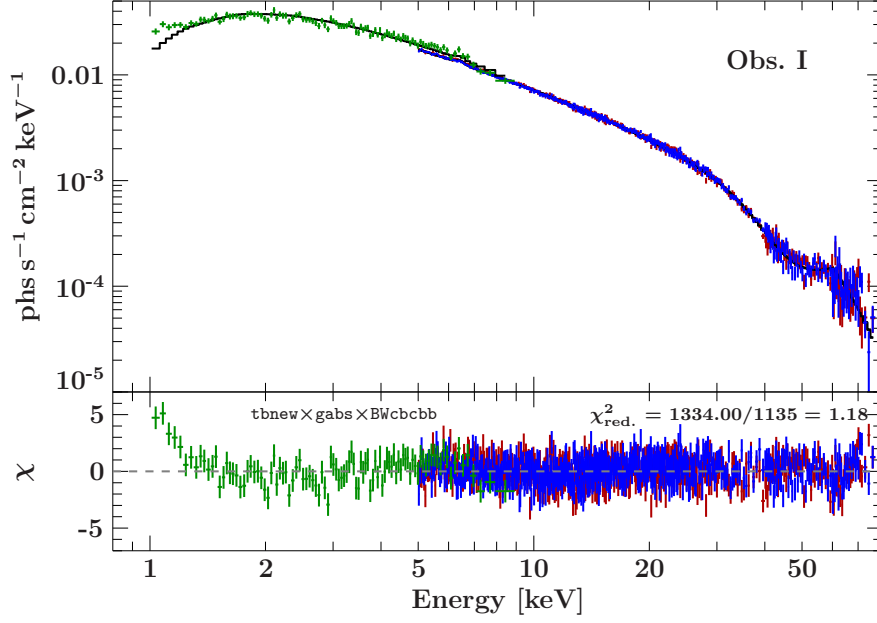


Fig. 6.10: Obs. I of A 0535+26 fitted with the BWcbb. The upper panels show the unfolded spectra of *Swift* (green) and *NuSTAR/FPMA* (blue) and *FPMB* (red). The lower panel shows the residuals.

Table 6.5: Best fit parameters for the BWcbb model for the first observation.

Parameter	Value
N_{H} [10^{22} cm $^{-2}$]	1.36
\dot{M} [10^{17} g s $^{-1}$]	0.091
kT_{e} [keV]	8.1
r_0 [m]	69
B [10^{12} G]	5.2
σ_{\parallel} [σ_{T}]	1.36×10^{-7}
$\bar{\sigma}$ [σ_{T}]	0.083
E_{cycl} [keV]	46.4
d_{cycl}	15.4
σ_{cycl} [keV]	8.6
E_{Fe} [keV]	6.4
EW_{Fe} [eV]	26
c_{FPMA}	1*
c_{FPMB}	1.009 ± 0.004
c_{XRT}	1.11

of the computational time that the model evaluation requires. A quantitative interpretation of the parameters is therefore not possible at this point. The fit shows, however, that the underlying theory of spectral pulsar formation, including the assumptions made can describe the observed spectral shapes on a wide energy range.

6.5 Discussion

The energy and flux dependence of the pulse profiles is in agreement with previous observation. An analysis of the pulse profiles using Fourier decomposition technique was presented by Caballero et al. (2011). The authors propose a hollow column and thermal halo around the column close to the neutron star surface to explain the observed pulse profile morphology and energy dependence. The findings by Caballero et al. (2011) could be taken as a starting point for self-consistently fitting the pulse profiles

with light bending models. Similar to KS 1947+300, any additional constraints on the geometry that allow to reduce the number of free parameters will be very helpful to speed up the calculations and avoid parameter degeneracies.

The spectral analysis shows that the two observations are clearly different from each other. None of the applied models could provide a satisfactory description of both observations. The parameters of the `cutoffpl` model of the brighter observation are similar to those found by Caballero et al. (2013) during the 2009 outburst. While the parameters stay relatively constant at higher luminosities, a change at very low luminosity was seen before but could be resolved in more detail with *NuSTAR*. A physical explanation for this behavior is still to be found.

The `compmag` model was applied to both observations and found to describe only the first observation well. The `flag` parameter was set assuming a velocity profile linear in τ which is also an assumption made by Becker & Wolff (2007) to solve the radiative transport equation analytically. The model failed, however, for the second observation, mainly because the rather abrupt steepening of the spectrum around 30 keV could not be modelled properly. It should be noted that some parameters hit the limits of their respective range, indicating that the fit has not converged to a minimum yet. The model has some runtime instabilities and a search of the full parameter space will have to be done once the problems of the implementation are fixed.

The `BWcbb` model was fitted to the first observation and the mass accretion rate was derived from the measured 0.1–100 keV flux of the best fitting empirical model. The magnetic field strength was tied to the centroid energy of a Gaussian absorption feature that models the cyclotron line. Except for the very low energy range, the model is able to describe the data well. The model is still under development and a quantitative interpretation of the results is not yet possible at this point because uncertainties could not be calculated for all parameters due to time constraints. The model assumes a radiation dominated shock and is therefore expected to work spectra of accreting X-ray pulsars at high luminosities. The fact that a good description of a spectrum at very low luminosities can be achieved raises the question whether all parameters found are reasonable in the sense that they are likely to represent the conditions at the emission region of the accretion column and if the fit is affected by model-intrinsic parameter correlations. This has to be investigated in much more detail in future work.

7 Conclusions and outlook

This thesis presents spectral and timing analyses of the two HMXB KS 1947+300 and A 0535+26. The spectral analysis of two *Suzaku* observations KS 1947+300 uses empirical continuum models and localized spectral features like iron emission lines and the evolution of model parameters over pulse phase are studied in detail. The phase averaged spectra of both observations show emission lines from neutral and He-like iron. The spectrum of the first observation even shows an emission line at the energy of H-like iron. Artificial parameter correlations are found to affect this evolution but a significant change of the spectral shape over pulse phase is observed.

The next step will be to model the spectrum with a self-consistent physical model like the BWcbcb model. This will allow to disentangle artificial parameter correlations and show how physical properties of the system really change with pulse phase.

The pulse profiles show a very characteristic dependence on energy. In particular, the pulse profile evolves from one broad peak at low energies to a broad, asymmetric peak and a secondary narrow peak. This behavior is rarely seen in accretion powered X-ray pulsars.

Again, the long term goal has to be to model the pulse profiles in a way that allows to infer the geometry of the system. Current light bending models are computationally very expensive but the special energy-dependence and morphology of these profiles might allow us to restrict parameter ranges before actually fitting the models. This makes KS 1947+300 a very promising example for dedicated pulse profile modelling studies.

For A 0535+26, empirical and physical models were applied. The spectra of the two observations are fundamentally different from each other. None of the tested model was able to provide a satisfactory description of both spectra. There have been hints in previous observations that the spectral shapes changes dramatically around a luminosity of 10^{36} erg s⁻¹.

The applied physical *compmag* and BWcbcb models, however, require a lot more detailed investigation. For example, both models have to be checked carefully for model-intrinsic parameter correlations. Generally, the physical models have a higher number of free parameters than the empirical ones and not all of them can be constrained from observational data. It will have to be discussed if parameters can be fixed and what “reasonable” values and ranges for the individual parameters are. Finally, the physical models will have to be tested also on the phase resolved spectra.

X-ray spectroscopy of accretion powered X-ray pulsars is very exciting these days, because of the huge progress of physical continuum models that was made in recent time. The development of these models is going on for many years now and we are now at a point where these models can for the first time be tested systematically on larger datasets owing to the constant increase of computational power. Some of these models are still in a testing phase and there might be still room for improvement. Finally, not only the continuum models will be superseded by self-consistent physical models but also the cyclotron lines can be modelled in a self consistent way. Theory predicts the line profile to deviate from a simple Gaussian or Lorentzian shape and high-resolution spectroscopy will hopefully allow us to resolve the actual shape of the lines and the predicted wings, which will improve our understanding of the physical conditions at the line-forming region. Again, this will require also the continuum to be modelled self-consistently to avoid the interplay of continuum and line models that caused so much lot of trouble so far.

Bibliography

- Araya, R.A., Harding, A.K., 1999, *ApJ*, 517, 334
- Araya-Góchez, R.A., Harding, A.K., 2000, *ApJ*, 544, 1067
- Bachetti, M., Harrison, F.A., Cook, R., et al., 2015, *ApJ*, 800, 109
- Ballhausen, R., Kühnel, M., Pottschmidt, K., et al., 2015, *A&A*, submitted
- Barthelmy, S.D., Barbier, L.M., Cummings, J.R., et al., 2005, *Space Sci. Rev.*, 120, 143
- Becker, P.A., Klochkov, D., Schönherr, G., et al., 2012, *A&A*, 544, A123
- Becker, P.A., Wolff, M.T., 2005a, *ApJ*, 621, L45
- Becker, P.A., Wolff, M.T., 2005b, *ApJ*, 630, 465
- Becker, P.A., Wolff, M.T., 2007, *ApJ*, 654, 435
- Blandford, R.D., Payne, D.G., 1981, *MNRAS*, 194, 1033
- Boldt, E., 1987, in *Observational Cosmology*, IAU Symposium 124, 611
- Boltzmann, L., 1884, *Annalen der Physik*, 258, 291
- Bombaci, I., 1996, *A&A*, 305, 871
- Bondi, H., Hoyle, F., 1944, *MNRAS*, 104, 273
- Borozdin, K., Gilfanov, M., Sunyaev, R., et al., 1990, *Sov. Astron. Lett.*, 16, 345
- Burrows, D.N., Hill, J.E., Nousek, J.A., et al., 2005, *Space Sci. Rev.*, 120, 165
- Caballero, I., Kraus, U., Santangelo, A., et al., 2011, *A&A*, 526, A131
- Caballero, I., Kretschmar, P., Santangelo, A., et al., 2007, *A&A*, 465, L21
- Caballero, I., Pottschmidt, K., Marcu, D.M., et al., 2013, *ApJ*, 764, L23
- Caballero, I., Wilms, J., 2012, *Memorie della Societa Astronomica Italiana*, 83, 230
- Camero-Arranz, A., Finger, M.H., Wilson-Hodge, C.A., et al., 2012, *ApJ*, 754, 20
- Camero-Arranz, A., Ozbey-Arabaci, M., Caballero-Garcia, M., 2014, *ATel* 6439
- Canuto, V., Lodenquai, J., Ruderman, M., 1971, *Phys. Rev. D*, 3, 2303
- Casella, P., Altamirano, D., Patruno, A., et al., 2008, *ApJ*, 674, L41
- Chakrabarty, D., Koh, T., Bildsten, L., et al., 1995, *ApJ*, 446, 826
- Chandrasekhar, S., 1931, *ApJ*, 74, 81
- Chodil, G., Mark, H., Rodrigues, R., et al., 1967, *Phys. Rev. Lett.*, 19, 681
- Coburn, W., Heindl, W.A., Rothschild, R.E., et al., 2002, *ApJ*, 580, 394
- D'Angelo, C., Spruit, H.C., 2011, in *Fast X-ray Timing and Spectroscopy at Extreme Count Rates (HTRS 2011)*, 39
- D'Angelo, C.R., Spruit, H.C., 2010, *MNRAS*, 406, 1208
- D'Angelo, C.R., Spruit, H.C., 2012, *MNRAS*, 420, 416
- Davidson, K., 1973, *Nature Physical Science*, 246, 1
- Einstein, A., 1917, *Physikalische Zeitschrift*, 18, 121
- Farinelli, R., Ceccobello, C., Romano, P., Titarchuk, L., 2012, *A&A*, 538, A67
- Farinelli, R., Titarchuk, L., Paizis, A., Frontera, F., 2008, *ApJ*, 680, 602
- Ferrigno, C., Farinelli, R., Bozzo, E., et al., 2013, *A&A*, 553, A103
- Fewell, M.P., 1995, *American Journal of Physics*, 63, 653
- Finger, M.H., Jenke, P.A., Wilson-Hodge, C.A., 2015, *ATel* 7017
- Finger, M.H., Wilson, R.B., Harmon, B.A., 1996, *ApJ*, 459, 288
- Finger, M.H., Wilson-Hodge, C.A., Jenke, P.A., GBM Pulsar Team 2014, *ATel* 6123
- Friedrich, H.S., 2006, *Theoretical Atomic Physics*, Springer-Verlag Berlin Heidelberg, 3rd edition
- Fukazawa, Y., Mizuno, T., Watanabe, S., et al., 2009, *PASJ*, 61, 17
- Fürst, F., Kreykenbohm, I., Suchy, S., et al., 2011, *A&A*, 525, A73
- Fürst, F., Pottschmidt, K., Wilms, J., et al., 2014, *ApJ*, 784, L40
- Galloway, D.K., Morgan, E.H., Levine, A.M., 2004, *ApJ*, 613, 1164
- Gamow, G., 1939, *Physical Review*, 55, 718
- Gehrels, N., Chincarini, G., Giommi, P., et al., 2005, *ApJ*, 621, 558
- Gehrels, N., Chincarini, G., Giommi, P., et al., 2004, *ApJ*, 611, 1005
- Giacconi, R., Gursky, H., Kellogg, E., et al., 1971, *ApJ*, 167, L67
- Giangrande, A., Giovannelli, F., Bartolini, C., et al., 1980, 40, 289
- Harrison, F.A., Craig, W.W., Christensen, F.E., et al., 2013, *ApJ*, 770, 103
- Heindl, W.A., Coburn, W., Gruber, D.E., et al., 2000, in *American Institute of Physics Conference Series*, Vol. 510, 173

- Hell, N., 2012, Laboratory Astrophysics: Investigating the mystery of low charge states of Si and S in the HMXB Cyg X-1, Master's thesis, Universität Erlangen-Nürnberg
- Hemphill, P.B., Rothschild, R.E., Markowitz, A., et al., 2014, *ApJ*, 792, 14
- Hilditch, R., 2001, An Introduction to Close Binary Stars, Cambridge astrophysics series, Cambridge University Press
- Houck, J.C., Denicola, L.A., 2000, in *Astronomical Data Analysis Software and Systems IX*, Vol. 216, Astronomical Society of the Pacific Conference Series, 591
- Illarionov, A.F., Sunyaev, R.A., 1975, *A&A*, 39, 185
- Ishisaki, Y., Maeda, Y., Fujimoto, R., et al., 2007, *PASJ*, 59, 113
- Islam, N., Maitra, C., Pradhan, P., Paul, B., 2015, *MNRAS*, 446, 4148
- Janka, H.T., Langanke, K., Marek, A., et al., 2007, 442, 38
- Jurua, E., Charles, P.A., Still, M., Meintjes, P.J., 2011, *MNRAS*, 418, 437
- Katz, J.I., 1986, High energy astrophysics, *Fontiers in Physics* 63, The Benjamin/Cummings Pub. Co. Inc., Menlo Park
- Kelley, R.L., Mitsuda, K., Allen, C.A., et al., 2007, *PASJ*, 59, 77
- Kendziorra, E., Kretschmar, P., Pan, H.C., et al., 1994, *A&A*, 291, L31
- Kippenhahn, R., Weigert, A., 1990, *Stellar Structure and Evolution*, Springer-Verlag Berlin Heidelberg, 1 edition
- Klochkov, D., Doroshenko, V., Santangelo, A., et al., 2012, *A&A*, 542, L28
- Kokubun, M., Makishima, K., Takahashi, T., et al., 2007, *PASJ*, 59, 53
- Kompaneets, A.S., 1957, *Sov. Phys., JETP*, 4, 730
- Koyama, K., Tsunemi, H., Dotani, T., et al., 2007, *PASJ*, 59, 23
- Krauß, F., 2013, Multiwavelength Observations of TANAMI Sources, Master's thesis, Universität Erlangen-Nürnberg
- Kretschmar, P., 1991, Calibration of high energy X ray detectors at the spectrum of the Crab nebula, and X ray pulsar A0535+26 examinations, Ph.D. thesis, Universität Tübingen
- Kretschmar, P., Pan, H.C., Kendziorra, E., et al., 1996, 120, C175
- Kreykenbohm, I., Coburn, W., Wilms, J., et al., 2002, *A&A*, 395, 129
- Kreykenbohm, I., Wilms, J., Kretschmar, P., et al., 2008, *A&A*, 492, 511
- Krimm, H.A., Holland, S.T., Corbet, R.H.D., et al., 2013, *ApJS*, 209, 14
- Kühnel, M., Falkner, S., Grossberger, C., et al., 2015, *Acta Polytechnica*, submitted
- Kühnel, M., Ferrigno, C., Esposito, V., et al., 2014, *ATel* 6129
- Kühnel, M., Müller, S., Kreykenbohm, I., et al., 2013, *A&A*, 555, A95
- Leahy, D.A., Darbro, W., Elsner, R.F., et al., 1983, *ApJ*, 266, 160
- Li, F., Clark, G.W., Jernigan, J.G., Rappaport, S., 1979, *ApJ*, 228, 893
- Longair, M.S., 2011, *High Energy Astrophysics*, Cambridge University Press, Cambridge, 3rd edition
- Makishima, K., Ohashi, T., Kawai, N., et al., 1990, *PASJ*, 42, 295
- Mihara, T., Makishima, K., Ohashi, T., et al., 1990, *Nat*, 346, 250
- Mineo, T., Romano, P., Mangano, V., et al., 2006, *Nuovo Cimento B Serie*, 121, 1521
- Mitsuda, K., Bautz, M., Inoue, H., et al., 2007, *PASJ*, 59, 1
- Müller, S., 2013, Observations of the X-ray Pulsars XTE J1946+274, 4U 0115+634, and GX 304, Ph.D. thesis, Universität Erlangen-Nürnberg
- Müller, S., Ferrigno, C., Kühnel, M., et al., 2013, *A&A*, 551, A6
- Müller, S., Kühnel, M., Caballero, I., et al., 2012, *A&A*, 546, A125
- Naik, S., Callanan, P.J., Paul, B., Dotani, T., 2006, *ApJ*, 647, 1293
- Naik, S., Maitra, C., Jaisawal, G.K., Paul, B., 2013, *ApJ*, 764, 158
- Naik, S., Paul, B., 2012, *Bull. Astron. Soc. India*, 40, 503
- Naik, S., Paul, B., Ali, Z., 2011, *ApJ*, 737, 79
- Nakajima, M., Mihara, T., Makishima, K., Niko, H., 2006, *Adv. Space Res.*, 38, 2756
- Negueruela, I., Israel, G.L., Marco, A., et al., 2003, *A&A*, 397, 739
- Negueruela, I., Okazaki, A.T., 2000, in *The Be Phenomenon in Early-Type Stars*, IAU Colloq. 175, Vol. 214, ASP Conference Proceedings, 713
- Ness, J.U., Schmitt, J.H.M.M., Burwitz, V., et al., 2002, *A&A*, 394, 911
- Nowak, M.A., Hanke, M., Trowbridge, S.N., et al., 2011, *ApJ*, 728, 13
- Oppenheimer, J.R., Volkoff, G.M., 1939, *Physical Review*, 55, 374
- Ozawa, M., Uchiyama, H., Matsumoto, H., et al., 2009, *PASJ*, 61, 1
- Ozbey-Arabaci, M., Camero-Arranz, A., Fabregat, J., et al., 2014, *ATel* 6265
- Padmanabhan, T., 2000, *Theoretical Astrophysics: Volume 1, Astrophysical Processes*, Theoretical Astrophysics, Cambridge University Press, Cambridge
- Palmeri, P., Mendoza, C., Kallman, T.R., et al., 2003, *A&A*, 410, 359
- Parker, M.L., Tomsick, J.A., Miller, J.M., et al., 2015, *ApJ*, 808, 9

- Patruno, A., Maitra, D., Curran, P.A., et al., 2015, *ApJ*, submitted
- Planck, M., 1901, *Annalen der Physik*, 309, 553
- Postnov, K.A., Gornostaev, M.I., Klochkov, D., et al., 2015, *MNRAS*, 452, 1601
- Pottschmidt, K., Wilms, J., Nowak, M.A., et al., 2004, in *Proceedings of the 5th INTEGRAL Workshop on the INTEGRAL Universe*, Vol. 552, ESA Special Publications, 345
- Prialnik, D., 2009, *An Introduction to the Theory of Stellar Structure and Evolution*, Cambridge University Press
- Psaltis, D., Lamb, F.K., 1997, *ApJ*, 488, 881
- Reig, P., 2011, *Ap&SS*, 332, 1
- Rivers, E., Markowitz, A., Pottschmidt, K., et al., 2010, *ApJ*, 709, 179
- Roming, P.W.A., Kennedy, T.E., Mason, K.O., et al., 2005, *Space Sci. Rev.*, 120, 95
- Rosenberg, F.D., Eyles, C.J., Skinner, G.K., Willmore, A.P., 1975, *Nat*, 256, 628
- Rothschild, R., Markowitz, A., Hemphill, P., et al., 2013, *ApJ*, 770, 19
- Rybicki, G.B., Lightman, A.P., 2008, *Radiative Processes in Astrophysics*, Physics textbook, WILEY-VCH, Weinheim
- Sarazin, C.L., Kempner, J.C., 2000, *ApJ*, 533, 73
- Schönherr, G., Schwarm, F.W., Falkner, S., et al., 2014, *A&A*, 564, L8
- Schönherr, G., Wilms, J., Kretschmar, P., et al., 2007, *A&A*, 472, 353
- Schwarm, F.W., 2010, *Cyclotron resonant scattering features in the line forming region of highly magnetized neutron stars*, Diploma thesis, Universität Erlangen-Nürnberg
- Shakura, N.I., Postnov, K.A., Kochetkova, A.Y., et al., 2015, *Astronomy Reports*, 59, 645
- Sobelman, I.I., 1992, *Atomic Spectra and Radiative Transitions*, Springer Berlin Heidelberg
- Staubert, R., Klochkov, D., Wilms, J., et al., 2014, *A&A*, 572, A119
- Steele, I.A., Negueruela, I., Coe, M.J., Roche, P., 1998, *MNRAS*, 297, L5
- Stefan, J., 1879, *Sitzungsberichte der mathematisch-naturwissenschaftlichen Classe der kaiserlichen Akademie der Wissenschaften*, 79, 391
- Swank, J., Morgan, E., 2000, 7531, 4
- Takahashi, T., Abe, K., Endo, M., et al., 2007, *PASJ*, 59, 35
- Tanaka, Y., 1986, in D. Mihalas, K.H.A. Winkler (eds.), *IAU Colloq. 89: Radiation Hydrodynamics in Stars and Compact Objects*, Vol. 255, Lecture Notes in Physics, Berlin Springer Verlag, 198
- Terada, Y., Mihara, T., Nakajima, M., et al., 2006, *ApJ*, 648, L139
- Titarchuk, L., 1994, *ApJ*, 434, 570
- Titarchuk, L., Lyubarskij, Y., 1995, *ApJ*, 450, 876
- Titarchuk, L., Mastichiadis, A., Kylafis, N.D., 1997, *ApJ*, 487, 834
- Tolman, R.C., 1939, *Physical Review*, 55, 364
- Trümper, J., Pietsch, W., Reppin, C., et al., 1978, *ApJ*, 219, L105
- Tsujimoto, M., Guainazzi, M., Plucinsky, P.P., et al., 2011, *A&A*, 525, A25
- Tsygankov, S.S., Lutovinov, A.A., 2005, *Astronomy Letters*, 31, 88
- Ubertini, P., Lebrun, F., Di Cocco, G., et al., 2003, *A&A*, 411, L131
- Uchiyama, Y., Maeda, Y., Ebara, M., et al., 2008, *PASJ*, 60, 35
- Verner, D.A., Ferland, G.J., Korista, K.T., Yakovlev, D.G., 1996, *ApJ*, 465, 487
- Wien, W., 1896, *Annalen der Physik*, 294, 662
- Wilms, J., Allen, A., McCray, R., 2000, *ApJ*, 542, 914
- Yamada, S., Makishima, K., Nakazawa, K., et al., 2011, *PASJ*, 63, 645

Acknowledgements

This work would not have been possible without the help and support of numerous people whom I want to express my gratitude.

First of all, I want to thank my advisor Jörn Wilms for giving me the opportunity to work on a project particularly matching my personal interests and I greatly appreciate the freedom and independence I experienced during the last year.

Special thanks go to Katja Pottschmidt for her advice and very instructive comments throughout this whole project and her help with writing the paper. I also want to thank her for getting me into contact with the NuSTAR Galactic Binaries Working Group.

Felix Fürst also contributed heavily to this work with his great experience in NuSTAR data analysis and the source KS 1947+300. His comments on the paper manuscript have always been constructive and helpful.

I want to thank Mike Wolff for letting me play around with his implementation of the BW model and his help with the actual application of the model.

The Neutron star gang at Remeis has always been supportive and I want to thank Matthias Kühnel, Sebastian Falkner, Dominik Hertel, Ingo Kreykenbohm, Fritz Schwarm, and Jakob Stierhof for the many valuable discussions, the great teamwork and the constant sharing of experience.

I have spent a huge part of the last year on preparing the manuscript of the paper summarizing the work on KS 1947+300. I want to thank all co-authors who helped with the data analysis, interpretation of the results and finally edited the manuscript. Apart from those already mentioned, these are Peter Kretschmar, Paul Hemphill, Amy Gottlieb, Rick Rothschild and Victoria Grinberg.

The Remeis observatory is a wonderful place to work because of all the lovely people there and my gratitude for the friendly atmosphere and the many recreational moments, like BBQ, swimming pool or cake (to mention only a few), belongs to every single one of them.

Last but not least, I want to thank my family and friends for their support.

Erklärung

Hiermit erkläre ich, die vorliegende Arbeit selbstständig verfasst und keine anderen als die angegebenen Hilfsmittel verwendet zu haben.

Bamberg, den 16. November 2015
